National Library
of Canada

Acquisitions and
Bibliographic Services Branch

395 Wellington Street
Ottawa, Ontario
K1A 0N4

Bibliothèque nationale
du Canada

Direction des acquisitions et
des services bibliographiques

395, rue Wellington
Ottawa (Ontario)
K1A 0N4

Your file Votre référence

Our file Notre référence

NOTICE

The quality of this microform is heavily dependent upon the quality of the original thesis submitted for microfilming. Every effort has been made to ensure the highest quality of reproduction possible.

If pages are missing, contact the university which granted the degree.

Some pages may have indistinct print especially if the original pages were typed with a poor typewriter ribbon or if the university sent us an inferior photocopy.

Reproduction in full or in part of this microform is governed by the Canadian Copyright Act, R.S.C. 1970, c. C-30, and subsequent amendments.

AVIS

La qualité de cette microforme dépend grandement de la qualité de la thèse soumise au microfilmage. Nous avons tout fait pour assurer une qualité supérieure de reproduction.

S'il manque des pages, veuillez communiquer avec l'université qui a conféré le grade.

La qualité d'impression de certaines pages peut laisser à désirer, surtout si les pages originales ont été dactylographiées à l'aide d'un ruban usé ou si l'université nous a fait parvenir une photocopie de qualité inférieure.

La reproduction, même partielle, de cette microforme est soumise à la Loi canadienne sur le droit d'auteur, SRC 1970, c. C-30, et ses amendements subséquents.

Canada

# Numerical Studies of Phase Behavior in Thermotropic and Lyotropic Liquid Crystals

by

Zhengping Zhang
Department of Physics, McGill University
Montréal, Québec
Canada

January, 1993

A Thesis submitted to the
Faculty of Graduate Studies and Research
in partial fulfillment of the requirements for the degree of
Doctor of Philosophy

© Zhengping Zhang, 1993

National Library
of Canada

Acquisitions and
Bibliographic Services Branch

395 Wellington Street
Ottawa, Ontario
K1A 0N4

Bibliothèque nationale
du Canada

Direction des acquisitions et
des services bibliographiques

395, rue Wellington
Ottawa (Ontario)
K1A 0N4

Your file Votre référence

Our file Notre référence

The author has granted an irrevocable non-exclusive licence allowing the National Library of Canada to reproduce, loan, distribute or sell copies of his/her thesis by any means and in any form or format, making this thesis available to interested persons.

L'auteur a accordé une licence irrévocable et non exclusive permettant à la Bibliothèque nationale du Canada de reproduire, prêter, distribuer ou vendre des copies de sa thèse de quelque manière et sous quelque forme que ce soit pour mettre des exemplaires de cette thèse à la disposition des personnes intéressées.

The author retains ownership of the copyright in his/her thesis. Neither the thesis nor substantial extracts from it may be printed or otherwise reproduced without his/her permission.

L'auteur conserve la propriété du droit d'auteur qui protège sa thèse. Ni la thèse ni des extraits substantiels de celle-ci ne doivent être imprimés ou autrement reproduits sans son autorisation.

ISBN 0-315-87889-4

Canada

# Phase Behavior of Thermotropic and Lyotropic Liquid Crystals

by

Zhengping Zhang

Department of Physics, McGill University

Montréal, Québec

Canada

January, 1993

© Zhengping Zhang, 1993

## Abstract

This thesis presents numerical studies of phase behavior for both thermotropic and lyotropic liquid crystals. The nature of the orientational transition in the Lebwohl–Lasher model for the nematic–isotropic phase transition is found to be weak first-order with the stability limits of the nematic and isotropic phases being extremely close to the equilibrium transition temperature. It is also found that the director fluctuations in the nematic phase correspond to fractional Brownian motion whereas the fluctuations in the isotropic phase follow ordinary Brownian motion. The Pink model is extended to give an accurate description of the main phase transition in lipid bilayers by introducing hydrophobic mismatch interactions between acyl chains and also direct inter-monolayer attractive interactions. The lateral density fluctuations and the resulting dynamic bilayer heterogeneity are studied. Lipid–protein interactions are further included to describe the phase separation of lipid–protein mixtures, gramicidin channel formation and the effects of protein on the lipid bilayers. A model is also proposed for phase transitions involving hydrogen bonding between the polar heads in lipid bilayers.

# Résumé

Cette thèse porte sur des études numériques du comportement des phases pour des cristaux liquides lyotropiques et thermotropiques. La nature de la transition d'orientation ayant lieu dans le modèle Lebwohl–Lasher, lequel est sensé représenter une transition de phase nématique–isotropique, s'est révélée du premier ordre. De plus, les limites de stabilité des phases nématiques et isotropiques sont très près de la température de transition à l'équilibre. Il y est également trouvé que les fluctuations directrices dans la phase nématique correspondent à des mouvements Browniens fractionnels alors que les fluctuations dans la phase isotropique ont lieu selon un mouvement Brownien ordinaire.

En outre, le modèle de Pink y est étendu afin de donner une description plus précise des transitions de phases principales dans les doubles couches lipidiques. Ceci est effectué en introduisant des intéractions hydrophobiques impaires entre les chaînes acyliques et des intéractions attractives directes entre les monocouches. La densité des fluctuations latérales et l'hétérogénéité dynamique résultante entre les couches ont été étudiées. Les intéractions lipides–protéines ont été incluses pour d'ecrire la séparation de phases des mélanges lipides–protéines, la formation des canaux de gramicidine, et enfin l'effet des protéines sur les doubles couches lipidiques.

Finalement, un modèle incluant des ponts hydrogène entre les têtes polaires dans les doubles couches lipidiques est proposé.

The author claims the originality of the ideas and results presented in this thesis. The following contributions are of particular interest:

- The Lee–Kosterlitz method was first used to study the $3d$ Lebwohl–Lasher model, the canonical model of a system which displays an orientational phase transition. The first unambiguous evidence for a very weak first-order transition in this model was found.
- The spinodal points for this model were first located here by studying the variation of the free energy which was obtained from the simulations of order-parameter distributions around the equilibrium transition temperature.
- The director fluctuations in liquid crystals were first investigated by Monte Carlo simulations described in this thesis. It was confirmed later by the neutron-scattering experiment that the Hurst exponent, $H \simeq 1$, in the nematic phase and the crossover between fractional and normal Brownian motion can be induced by an external field.
- The study of director fluctuations led to the finding of a new universal class of models with a continuous order-parameter degeneracy.
- The mismatch interactions between the lipid acyl-chain conformation states were first introduced in this thesis to describe the main phase transition via an extended Pink model.
- It was first suggested here that the finite-size effects should be considered in the interpretation of experimental observations for small biological systems.

- The relation between the specific heat obtained from finite-size simulations and the latent heat at first-order transitions was first clarified in this thesis.
- The kinetics of ionic conduction equilibria for the ion channel of gramicidin in term of monomer–dimer formation of gramicidin molecules was first simulated here in a novel bilayer model composed of two monolayers.
- A new correlation function was first introduced here to the study in the effects of proteins on lipids. The suppression of the correlations in the presence of proteins is consistent with the recent $^2H - NMR$ observations.
- The Lee–Kosterlitz method was first used here to determine the phase boundaries of binary mixtures in terms of temperature and composition.
- The first microscopic model was established in this thesis to predict a critical mixing point in a binary peptide–lipid mixture. The study led to the first understanding of the lower critical mixing point found in experiments at the level of a microscopic model.
- The method of Ferrenberg and Swendsen was first used in this thesis to calculate the properties related to cluster distributions and the exponents at percolation transitions.
- A new model for $2d$ hydrogen bonding networks in lipid bilayers was proposed in this thesis.

I am indebted to Professor Martin J. Zuckermann, my research supervisor, who introduced me to the field of lyotropic liquid crystals and to various numerical simulation methods. He has provided me with both stimulating suggestions and freedom for my research. I also wish to thank him for his help in the preparation of this thesis.

I am very grateful to Professor Ole G. Mouritsen, The Technical University of Denmark, who introduced me to the field of thermotropic liquid crystals. His ideas and suggestions led to the work presented in Chapter 3 in this thesis. I would also like to thank him for inviting me to visit Denmark twice and providing me with further supervision and excellent facilities for research.

I am indebted to Professor Jan Tobochnick, Kalamazoo College, Kalamazoo. Without his help, I would not have understood the percolation aspect of the work reported in Chapter 6. Hence the work would probably never have been completed.

I would like to give special thanks to Professor Hong Guo and my colleague, Mohamed Laradji, from whom I learned the new Monte-Carlo simulation methods which have been widely used in this thesis.

I wish to thank Dr. John H. Ipsen and Dr. Maria M. Sperotto, The Technical University of Denmark, for many helpful discussions for the results reported in Chapter 4 and 5 of this thesis.

I wish to thank three experimentalists for their collaborations: Professor John Silvius (Department of Biochemistry, McGill University), Professors K. Otnes and T. Riste (Institutt for Energiteknikk, Norway).

I would like to thank my colleagues, Loki Jörgenson and Martin D. Lacasse, for their help on computer facilities. I also thank Martin D. Lacasse for translating the abstract of this thesis from English into French for me.

Finally I wish to thank University of Science and Technology of China in Anhui for keeping my position open for the past four years.

**to my wife and son**

# Contents

# List of Figures

# Chapter 1

# General Introduction

Liquid crystal phases are distinct states of matter that have structural order intermediate between that of conventional liquids and solids (de Gennes, 1974). For example, many organic crystals melt by passing through intermediate fluid phases that are optically anisotropic. Although liquid crystals were identified for at least 100 years, they have attracted major attention from physicists only in the last twenty-five years (Litster and Birgeneau, 1982). The dramatic rise in scientific interest in liquid crystals has occurred for several reasons. First, liquid crystals precipitated a revolution in the display industry and this in turn excited the interest of basic scientists. Second, the liquid-crystalline state is ubiquitous in biological systems and this has led to a major effort in biological research. Third, the physical behavior of liquid crystals raises some fundamental problems in statistical physics.

From the way that the liquid crystals change phases, they can be classified into *thermotropic* and *lyotropic* liquid crystals (Litster and Birgeneau, 1982; Pershan, 1982). For thermotropic materials, as the name implies, temperature determines the phase. However, for lyotropic substances, concentration is the main physical variable.

*Thermotropic* liquid-crystal phases are those observed in pure compounds or homogeneous mixtures as the temperature is changed. They are conventionally classified into nematic, cholesteric, and smectic phases (see Fig. 1.1). The nematic phase is the least complex liquid-crystal phase, whose long range order is based on molec-

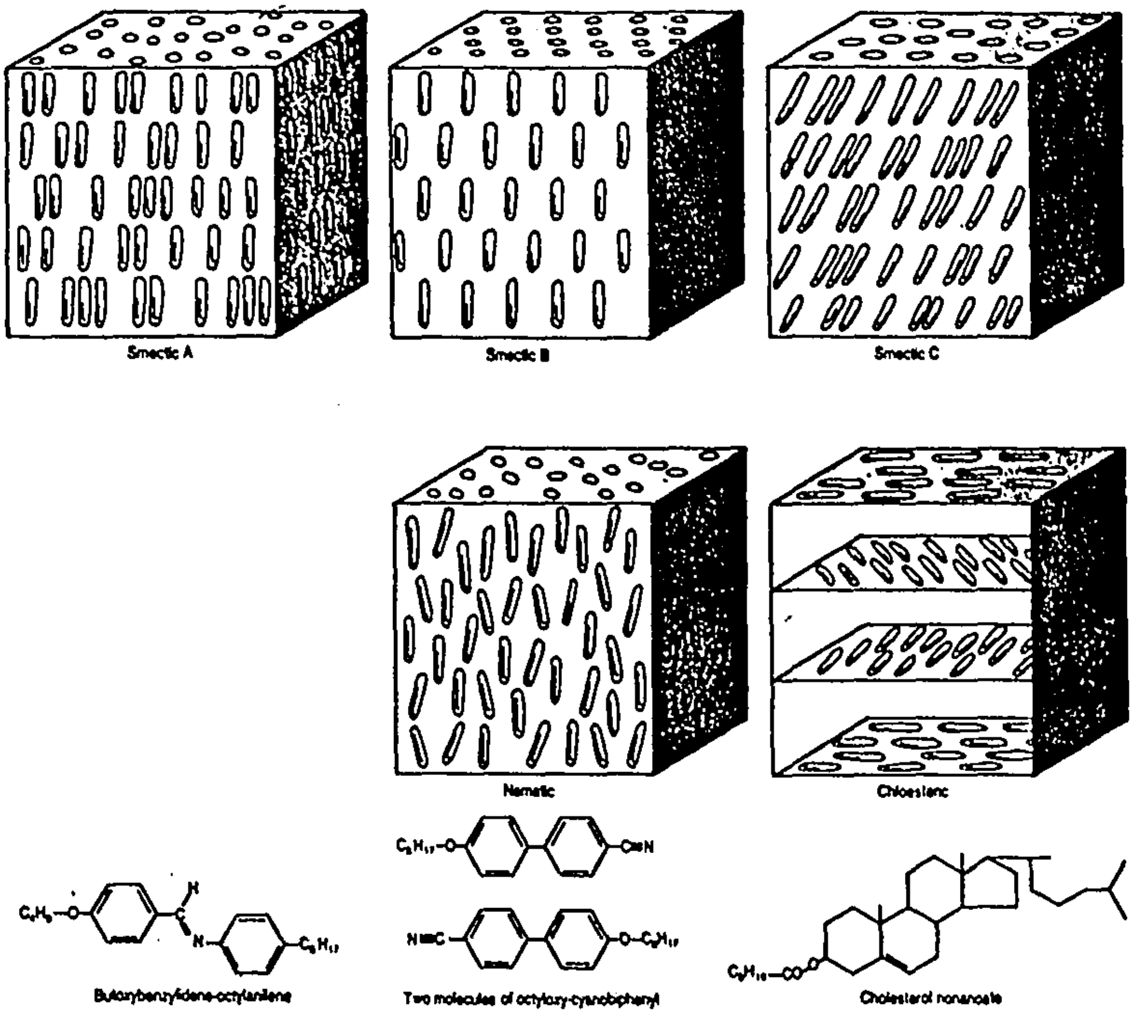

Figure 1.1: Common types of liquid-crystal ordering [After Ref. (Litster and Birgeneau, 1982)].

ular orientation via quadrupole–quadrupole interactions. This phase is used in calculator and wrist-watch displays (Kahn, 1982). The molecules butoxybenzylidene-octylanilene and octyloxy-cyanobiphenyl in Fig. 1.1 both exhibit nematic phases. The thermotropic nematics have one symmetry axis, called the director **n**, and are optically uniaxial with a strong birefringence. The molecules themselves usually lack a center of symmetry but the nematic phase has inversion symmetry and the orientational order parameter has quadrupolar rather than dipolar symmetry. The continuous rotational symmetry of the isotropic liquid phase is broken when the molecules choose a particular direction to orient along in the nematic phase. Another thermotropic phase having only molecular orientational order is formed by chiral molecules. This is the *cholesteric* phase, thermodynamically equivalent to a nematic but with a chiral character that causes the director to twist (see Fig. 1.1) with a pitch that is comparable to the wavelength of light. The name 'cholesteric' derives from the fact that many cholesterol esters exhibit this phase. The strong modulation of the refractive index due to the twist causes Bragg scattering of various colors of light and makes cholesterics the most beautiful of the liquid-crystal phases. The remaining important thermotropic phases are *smectics*. There are many distinct smectic polytypes bearing the labels smectic $A,B,C,...$, with the phases being labeled not according to any microscopic properties but rather by the chronological order of their discovery. It is clear, however, that these liquid-crystal phases have different underlying symmetry properties. The smectics are distinguished by having an intermediate degree of positional order in addition to molecular orientational order. Smectics have usually been identified by the textures they exhibit under a polarizing microscope and by miscibility studies with known phases. The molecules butoxybenzylidene-octylanilene and octyloxy-cyanobiphenyl shown in Fig. 1.1 also exhibit smectic phases.

*Lyotropic* liquid-crystal phases are observed when amphiphilic (from the Greek 'amphi' meaning 'on both sides' and 'philo' meaning 'loving') molecules, such as soaps, are dissolved in water. The simple soap, potassium *n*-octanoate, for example, exhibits such liquid-crystal phases. The molecules of this soap have a hydrocarbon,

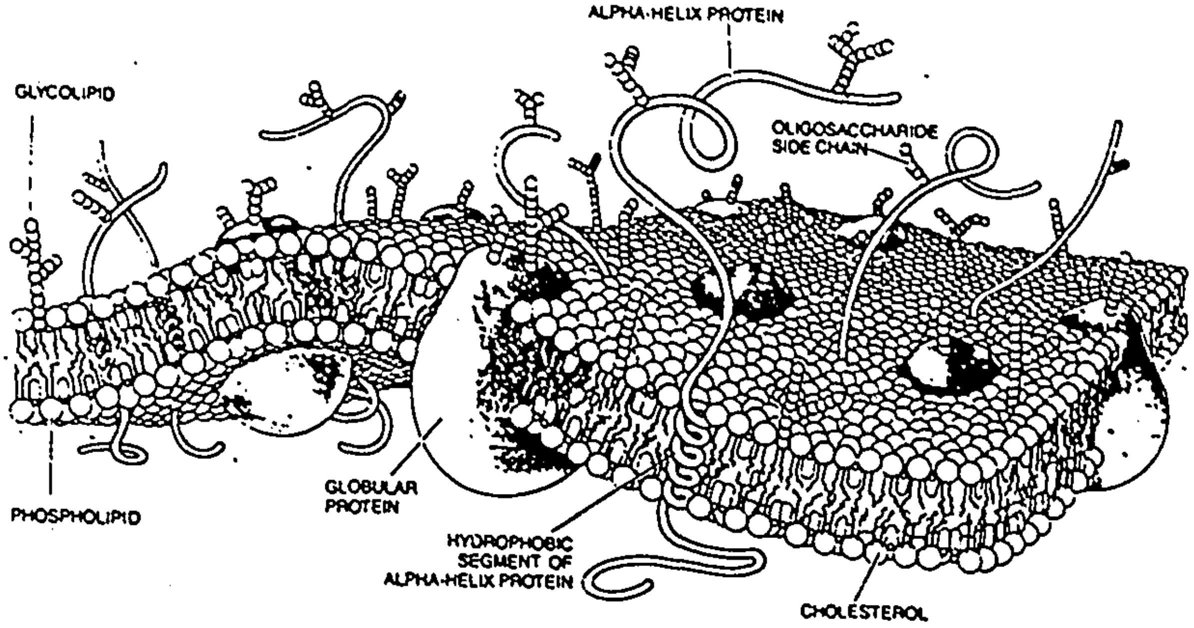

Figure 1.2: A cartoon of the fluid-mosaic model of a biological membrane [After Ref. (Mouritsen, 1987)].

or $n$-alkane part, $CH_3(CH_2)_7$– that is poorly soluble in water and a 'polar head group'—$CO_2^- K^+$ that is exceedingly water-soluble. At suitable concentrations and temperatures, nature resolves these opposite tendencies by forming liquid-crystalline phases in which the molecules are arranged so that the polar head groups shield the hydrocarbon parts from the water.

Lyotropic liquid crystals have long been important to researchers interested in biological membranes. These membranes are, in general, composed of individual lipid and protein molecules in a bilayer structure 60–100 Å thick (Fig. 1.2). The lipid molecules involved in bilayer formation are amphipathic. They are composed of a polar or charged head group attached to a variable-length nonpolar tail. Depending on their molecular structure, lipids in water spontaneously form micelles, vesicles, monolayers, or bilayers. In all cases, the driving force is primarily entropic in nature. The *hydrophobic effect* favors these structures because they minimize the contact between the nonpolar regions of molecules and the surrounding water. Minimizing this contact area minimizes the structural ordering of water molecules around the nonpolar groups. The lipid tails also show van der Waals attractions and the polar head groups show electrostatic and hydrogen bond attraction to the solvent water. Thus, cooperative motion of lipid molecules with long tails seeking a thermodynamic energy minimum leads to the formation and maintenance of the bilayer structure.

Biological membranes play a central role in both the structure and function of all cells, from plant to animal (Gennis, 1989). They provide the cells with a permeability barrier which is necessary in order to maintain chemical and electrical gradients between the intra- and extra-cellular media. They also determine the nature of all communication between the two sides, such as the actual passage of ions. This includes the transport of electrons, the conversion of sunlight to chemical and electrical energy, pumping small molecules against a concentration gradient, and the use of that gradient as a source of energy. What is so remarkable about a biological membrane is that, in a process known as *self-assembly*, its thousands of individual component molecules spontaneously associate, align, and create its precisely defined structure.

The lipid bilayer which will be considered in this thesis is only a small part of the large macromolecular composite which makes up the biological membrane. Proteins constitute from 25% to 80% of the membrane by weight. These membrane proteins fall into two classes. Peripheral proteins bind to the surface of the membrane, generally through polar interactions, ionic bonds, or hydrogen bonds. Integral proteins penetrate the membrane, often extending beyond its surface in both directions. These proteins can also self-assemble with the membrane as it is driven spontaneously to an energy minimum. Non-membrane proteins fold spontaneously with their nonpolar amino acid side chains in the central core, protected from solvent water by the amino acids with polar or charged side chains that appear on the surface. Membrane proteins, on the other hand, fold so that the nonpolar amino acid side chains are on their surface, in contact with the nonpolar tails of the lipids in the interior of the membrane.

With our interest in understanding phase transitions, we examine in this thesis the properties of theoretical models for the nematic–isotropic phase transition in thermotropic liquid crystals and for the gel–fluid transition in lyotropic liquid crystals.

In Chapter 2, we give an introduction to the numerical methods used in the thesis. Then we present our analysis and results in the rest of the chapters of this thesis.

In Chapter 3, we study the three-dimensional Lebwohl-Lasher model for liquid crystals. The Lebwohl-Lasher model is the canonical model of a system which displays a nematic–isotropic phase transition. A better understanding of the model is useful for studying the basic interactions between lipid molecules. In fact, the first model for lipid bilayers was a liquid crystal model. The anisotropic van der Waals interactions between the acyl chains described below for the Pink model of lipid bilayers correspond to a mean-field approximation of the interactions used in the Lebwohl-Lasher model.

In Chapter 4, we are concerned with the main phase transition of pure phospholipid bilayers. A brief introduction to phospholipids and the basic experimental observations for the transition is given in the chapter. Extensions of the Pink model which describe the first-order phase transition are then presented.

In Chapter 5 we propose on the basis of the extended models in Chapter 4 a model for lipid–protein mixtures in order to examine the bilayer phases of these systems. The studies are then compared to experimental results for gramicidin channels and phase diagrams of lipid–protein mixtures.

Polar-head interactions between lipids are discussed in Chapter 6. We present a lattice model for the hydrogen bonding of polar-heads in order to describe the hydration–dehydration transition. The aspect of percolation in the hydrogen bonding model is investigated in detail.

The thesis is concluded in Chapter 7 which contains suggestions for further work.

# Chapter 2

# Numerical Simulation Methods

In this chapter we discuss the numerical simulation methods which are used in the later chapters. Furthermore, we choose the Ising model in a magnetic field as a tutorial example although the applications of the methods are quite general. We begin by giving a general description of the Monte Carlo method and its application to problems in statistical physics (Mouritsen, 1984; Binder and Heermann, 1988) and we then describe the recent extensions due to Ferrenberg and Swendsen (Ferrenberg and Swendsen, 1988) and Lee and Kosterlitz (Lee and Kosterlitz, 1990).

## 2.1 The Monte Carlo Method in Statistical Physics

### 2.1.1 Monte Carlo Methods: General Considerations

Monte Carlo methods are used to solve numerically mathematical problems which are too complex to allow an exact analytical treatment. The problems approached by Monte Carlo methods are conveniently devided into two classes consisting of probabilistic and deterministic problems respectively. In solving a probabilistic problem, one tries to simulate directly the random process inherent in the problem. A classical example is simulation of neutron diffusion in reactors. Solving a deterministic problem by a Monte Carlo calculation requires a transformation of the deterministic problem into another problem of a stochastic nature. The original problem need not itself have anything to do with random processes. The only requirement is that the original problem and the transformed one have solutions which differ by a controlled amount. A example of deterministic problems which have been solved by Monte Carlo methods is that of multi-dimensional integrals in many-body theory. We are then concerned with the type of Monte Carlo methods which allow a numerical evaluation of the multi-dimensional integrals which arise in the physics of interacting many-body systems.

### 2.1.2 Statistical Mechanics

The application of Monte Carlo methods to statistical physics requires the description of some basic statistical mechanical properties. A microstate, or configuration, of a system is described by a set of mechanical variables, $\mathbf{\Omega}$, which contains the values of all possible degrees of freedom for each particle of the system. *Phase space*, $\{\mathbf{\Omega}\}$, is the space spanned by all possible microstates of a system. The properties of the system is governed by a Hamiltonian function, $\mathcal{H}(\mathbf{\Omega})$, defined in terms of the mechanical variables. For a ferromagnetic system described by two-dimensional Ising model, the Hamiltonian is

$$\mathcal{H} = -J\sum_{\langle i,j\rangle} S_iS_j - H\sum_i S_i \quad (J>0) \tag{2.1}$$

where the spin $S_i$, representing a magnet at site $i$, can point up or down along the 'easy axis', the exchange energy $J$ is restricted to nearest neighbors, and $H$ is a magnetic field. In this case, the phase space $\{\mathbf{\Omega}\} \equiv \{S_i\}$ with all possible configurations. In statistical mechanics, a probability, $\rho(\mathbf{\Omega})$, is associated with each configuration. The probability may be expressed in terms of a canonical density function

$$\rho(\mathbf{\Omega}) = \frac{e^{-\mathcal{H}(\mathbf{\Omega})/k_BT}}{Z} \tag{2.2}$$

where $Z$ is a normalization factor (the partition function)

$$Z = \int_{\{\mathbf{\Omega}\}} e^{-\mathcal{H}(\mathbf{\Omega})/k_BT}\, d\mathbf{\Omega}. \tag{2.3}$$

$T$ is the absolute temperature and $k_B$ is Boltzmann's constant. Given the probability distribution of the configuration, the thermodynamic average of a measurable physical quantity, $g(\Omega)$, is obtained in the canonical ensemble as

$$< g >= \int_{\{\Omega\}} g(\Omega)\rho(\Omega) d\Omega \tag{2.4}$$

The properties of the system in thermodynamic equilibrium are then determined by Eq. (2.4) which constitutes the formal connection between the microscopic and macroscopic physical worlds. Based on Eq. (2.4), one has a set of relationships between response functions and equilibrium variances for the corresponding physical quantities. This is the so-called *fluctuation–dissipation theorem* which is expressed as follows in the case of the specific heat $C_P(T)$ and the isothermal compressibility $\chi(T)$:

$$C_P(T) = \frac{1}{nk_BT^2}(\langle \mathcal{H}^2 \rangle - \langle \mathcal{H} \rangle^2) \tag{2.5}$$

$$\chi(T) = \frac{1}{nk_BT}(\langle X^2 \rangle - \langle X \rangle^2) \tag{2.6}$$

where $n$ is the number of particles in system and $X$ is the order parameter.

### 2.1.3 Importance Sampling

The use of the Monte Carlo method in equilibrium statistical mechanics is based on the idea of approximating Eq. (2.4) by a summation using only a characteristic subset of phase space points, $\{\Omega_1, \Omega_2, \ldots, \Omega_N\}$, which are used as a statistical sample. If $N$ is large enough, one has

$$< g > \approx \frac{\sum_{i=1}^{N} e^{-\mathcal{H}(\Omega_i)/k_BT} g(\Omega_i)}{\sum_{i=1}^{N} e^{-\mathcal{H}(\Omega_i)/k_BT}} \tag{2.7}$$

The points, $\{\Omega_i\}$, may be chosen by two kinds of sampling, simple sampling and importance sampling. In *simple sampling*, one chooses the points at random, using 'pseudo-random numbers' produced by a 'random number generator' built into the computer. In the neighborhood of phase transition, however, this procedure is highly inefficient since the Boltzmann weights vary by many orders of magnitude. Important information about the transition may therefore be lost by using simple sampling. *Importance sampling* samples the configuration $\{\Omega_i\}$ not completely random, but preferentially from the region of phase space which is important at temperature $T$. Consider a process where the phase space points, $\{\Omega_i\}$, are selected according to a probability, $P(\Omega_i)$. With the choice of this set $\{\Omega_i\}$ for the calculation of a thermal average, formula (2.7) is now replaced by

$$< g > \approx \frac{\sum_{i=1}^{N} e^{-\mathcal{H}(\Omega_i)/k_BT} g(\Omega_i)/P(\Omega_i)}{\sum_{i=1}^{N} e^{-\mathcal{H}(\Omega_i)k_BT}/P(\Omega_i)} \tag{2.8}$$

One choice for $P(\Omega_i)$ would be $P(\Omega_i) \propto \exp[-\mathcal{H}(\Omega_i)/k_BT]$. The Boltzmann factor cancels out altogether, and Eq. (2.8) is reduced to an arithmetic average

$$< g > \approx \frac{1}{N} \sum_{i=1}^{N} g(\Omega_i) \tag{2.9}$$

The problem is then to find a procedure which implements importance sampling. Such a procedure is due to Metropolis *et al* (Metropolis *et al.*, 1953).

### 2.1.4 The Metropolis Monte Carlo Method

Metropolis *et al.* (Metropolis *et al.*, 1953) chose successive states $\{\Omega_i\}$ stochastically via a Markov process where each state $\Omega_{i+1}$ is obtained from the previous state $\Omega_i$ via a suitable transition probability $W(\Omega_i \rightarrow \Omega_{i+1})$. A sufficient condition for achieving this is the principle of detailed balance

$$P_{eq}(\Omega_i)W(\Omega_i \rightarrow \Omega_{i'}) = P_{eq}(\Omega_{i'})W(\Omega_{i'} \rightarrow \Omega_i) \tag{2.10}$$

Metropolis *et al.* then showed, from the transition probability $W$ in the limit $N \rightarrow \infty$, that the distribution function $P(\Omega_i)$ of the states generated by this Markov process tends towards the equilibrium distribution

$$P_{eq}(\Omega_i) = \frac{1}{Z} e^{-\mathcal{H}(\Omega_i)/k_BT}. \tag{2.11}$$

Eq. (2.10) implies that the ratio of transition probabilities for a 'move' $\Omega_i \rightarrow \Omega_{i'}$ and the inverse move $\Omega_{i'} \rightarrow \Omega_i$ depend only on the energy change $\delta\mathcal{H} = \mathcal{H}(\Omega_{i'}) - \mathcal{H}(\Omega_i)$,

$$\frac{W(\Omega_i \rightarrow \Omega_{i'})}{W(\Omega_{i'} \rightarrow \Omega_i)} = e^{-\delta\mathcal{H}/k_BT} \tag{2.12}$$

Eq. (2.12) does not specify $W(\Omega_i \to \Omega_{i'})$ uniquely, and some arbitrariness in the explicit choice of $W$ remains. One frequently used form for $W$ is

$$W(\Omega_i \to \Omega_{i'}) = \begin{cases} \frac{1}{\tau_s} e^{-\delta\mathcal{H}/k_B T} & \text{if } \delta\mathcal{H} > 0 \\ \frac{1}{\tau_s} & \text{otherwise} \end{cases} \tag{2.13}$$

The quantity $\tau_s$ usually is chosen as unity. On the basis of Eq. (2.13), Metropolis *et al.* proposed the following algorithm for the canonical Monte Carlo method,

1. Specify an initial configuration $\Omega$.
2. Generate a new configuration $\Omega'$.
3. Compute the energy change $\delta\mathcal{H}$.
4. Calculate the transition probability $W$ for the change.
5. Choose a random number $R$ uniformly distributed between 0 and 1.
6. If $R < W$, accept the new configuration; otherwise retain the old configuration.
7. Analyze the resulting configuration as desired, and store its properties to calculate the necessary averages. Then return to step 2.

A measure of the times by which the above algorithm is repeated is Monte Carlo steps per particle (MCS).

### 2.1.5 Dynamic Interpretation of the Metropolis Monte Carlo Method

There are usually correlations which occur between the configurations generated sequentially in the Markov chain described in Sec. 2.1.4. These correlations strongly affect the accuracy that can be obtained from a given number of MCS. They can be understood by interpreting the Monte Carlo averaging in terms of a master equation describing a well-defined dynamic model with stochastic kinetics (Mouritsen, 1984; Binder and Heermann, 1988). The interpretation of correlations as time is useful for estimating of the accuracy and provides the theoretical basis for the application of Monte Carlo methods to the simulation of dynamic processes. One application is the simulation of the Brownian motion of macromolecules. The time $t$ is associated with the scale $i$ of the subsequent configurations. Therefore, the probability that a configuration $\Omega$ occurs at time $t$, $P(\Omega, t)$, corresponds to $P(\Omega_i)$ in a Monte Carlo process, *i.e.* $P(\Omega, t) \equiv P(\Omega_i)$. This probability satisfies the Markovian master equation

$$\frac{dP(\Omega,t)}{dt} = -\sum_{\Omega'} W(\Omega \rightarrow \Omega')P(\Omega,t) + \sum_{\Omega'} W(\Omega' \rightarrow \Omega)P(\Omega',t). \qquad (2.14)$$

In thermal equilibrium, $\frac{dP(\Omega,t)}{dt} = 0$ so that detailed balance, Eq.(2.10), is satisfied.

## 2.2 Ferrenberg-Swendsen Extrapolation Method

The data obtained from standard Monte Carlo simulations described in Sec. 2.1.4 are averages of thermodynamic quantities at the single point in the parameter space for which the simulation is performed. Therefore in order to obtain information over a range of parameters, one has to perform many individual simulations in the parameter range. Recently, Ferrenberg and Swendsen (Ferrenberg and Swendsen, 1988) proposed an efficient method which uses standard simulation methods to generate continuous thermodynamic functions across important regions of parameter spaces. The data from a single simulation can for example be used to study the entire scaling region near a phase transition. The method is especially important when the behavior of the system displays sharp peaks, such as those near first- and second-order phase transitions, which are crucial for understanding the critical behavior of a model. Standard Monte Carlo techniques locate the position of a narrow peak by multiple high-accuracy simulations. The result is a set of discrete points, none of which is exactly at the maximum. With the new method, data from a single simulation can be used to accurately locate the peak position and determine its height.

To illustrate the Ferrenberg-Swendsen method, consider a Monte Carlo simulation of the Ising model. Each configuration is generated with its proper thermal weight and is then averaged over time to give the equilibrium averages of physical quantities of interest. These averages are the usual output of Monte Carlo simulations. However, Ferrenberg and Swendsen (Ferrenberg and Swendsen, 1988) showed that the corresponding histogram can be used to extract more information from the simulation. To this purpose, the average in the formula (2.7) is performed for a point in parameter space, for example at $(T,H)$, for the Ising model. Choosing $S = \sum_{\langle i,j \rangle} S_i S_j$ and $M = \sum_i S_i$ as quantities representing configuration of system, the probability distribution of S and M at space $(T,H)$ can be written as

$$P_{(T,H)}(S,M) = \frac{n(S,M)e^{\frac{1}{k_BT}(JS+HM)}}{\sum_{S,M} n(S,M)e^{\frac{1}{k_BT}(JS+HM)}}, \tag{2.15}$$

where $n(S,M)$ is the degeneracy of the configurations with the same $S$ and $M$. The histogram of values of $(S,M)$ generated by the Monte Carlo simulation is proportional to $P_{(T,H)}(S,M)$. By storing this histogram, one can generate the normalized probability distribution. The histogram can then be used to generate data for different parameters. The normalized probability distribution with new parameters $(T',H')$ can be expressed in terms of the distribution with $(T,H)$ in the following way:

$$P_{(T',H')}(S,M) = \frac{P_{(T,H)}(S,M)e^{(\frac{1}{k_BT'}-\frac{1}{k_BT})(JS+HM)+(H'-H)\frac{M}{k_BT}}}{\sum_{S,M} P_{(T,H)}(S,M)e^{(\frac{1}{k_BT'}-\frac{1}{k_BT})(JS+HM)+(H'-H)\frac{M}{k_BT}}} \tag{2.16}$$

Since $T'$ and $H'$ are continuously variable, any quantities of interest, including the cluster distribution, can be calculated as a continuous function of the parameters (Zhang, Mouritsen and Zuckermann, 1992a; Zhang *et al.*, 1992c). The technique can easily be generalized to other models, including those with continuous symmetry or described by several parameters.

## 2.3 Determination of the Nature of Phase Transitions

Metropolis Monte Carlo simulations can only be performed for finite systems. In the early use of this method, a system with as large a size as possible was used in order to suppress the finite-size effects. However, a knowledge of the finite-size effects is useful not only for the calculation of the various thermodynamic quantities for small systems and their extrapolation to nontrivial thermodynamic limit but also because it is possible to obtain information about the nature of a phase transition (Challa, Landau and Binder, 1986; Mouritsen, 1984; Zhang *et al.*, 1992a).

### 2.3.1 Finite Size Effects of Phase Transitions

A first-order transition is characterized by discontinuities in the first derivatives of the free energy, such as the internal energy and the magnetization in the thermodynamic limit (Landau and Lifshitz, 1980). This results in $\delta$-function singularities in the specific heat and the susceptibility at the transition. The singularities at a first-order transition are due to phase coexistence. At a second-order transition, on the other hand, the divergences are intimately linked to the divergence of the correlation length. In a finite system, however, the above divergences do not occur. Instead, in both types of transition, one sees finite peaks in the specific heat and the susceptibility near the transition point. Two effects appear because of the finite size: a 'rounding' of the transition region occurs with the peak heights increasing with lattice size and the location of the maxima shift in a size-dependent fashion (Challa, Landau and Binder, 1986; Fisher, 1971). In a second-order transition the rounding is due to the correlation length being limited by the lattice size, $L$, so that the scaling theory predicts that the maximum of the specific heat diverges as $L^{\alpha/\nu}$ and that the half-width decreases as $L^{-1/\nu}$. At a first-order transition, $L$ appears only in terms of the volume, $L^d$, in $d$ dimensions. The maxima therefore grows as $L^d$ and the $\delta$-function limit is obtained because the width decreases as $L^{-d}$. The scaling for the specific heat and the susceptibility is given by (Mouritsen, 1984; Fisher, 1971)

$$\begin{aligned} c_L^{max} &= a + bL^{\psi} \\ \chi_L^{max} &= a' + b'L^{\psi} \end{aligned} \tag{2.17}$$

where $\psi = d$ for a first-order transition and $\psi = \alpha/\nu$ for a second-order transition. Note that these specific predictions only apply when $L$ is large enough.

The fourth-order cumulant proposed by Binder (Binder, 1981) is a useful quantity to measure in a simulation since it behaves quite differently at first-order and continuous transitions. This quantity is defined in terms of the configurational energy, $E$, as follows

$$\sigma(L) = 1 - \frac{\langle E^4 \rangle}{3\langle E^2 \rangle^2}. \tag{2.18}$$

For continuous transitions, $\sigma(L) \to \frac{2}{3}$ for all temperatures as $L \to \infty$. For first-order transitions, $\sigma(L)$ takes on the value 2/3 for both high and low temperatures, tending toward a nontrivial minimum value at the transition temperature. The minimum value, $\sigma_L^{min}$, of $\sigma(L)$ scales as $L^{-d}$ in the thermodynamic limit. However this method suffers from severe crossover effects.

### 2.3.2 Lee-Kosterlitz Method

An unambiguous method which determines the order of a phase transition was proposed by Lee and Kosterlitz (Lee and Kosterlitz, 1990). This method consists of calculating the free energy as a function of the order parameter, $X$, from the probability distribution at the transition. In the Ising model, $X$ would be the magnetization per spin. The distribution of the order parameter $\mathcal{P}(X,T,L)$, as already described in Sec. 2.2, can be obtained from the histogram of $X$ generated in a single Monte Carlo simulation at $T$ for the system with size $L$. The free-energy-like quantity, $\mathcal{A}(X,T,L)$, defined by

$$\mathcal{A}(X,T,L) \sim -\ln \mathcal{P}(X,T,L) \tag{2.19}$$

differs from the bulk free energy, $\mathcal{F}(X)$, by a $T$- and $L$-dependent additive quantity. However, at fixed $T$ and $L$, the shape of $\mathcal{A}(X,T,L)$ is identical to that of $\mathcal{F}(X)$ and furthermore $\mathcal{A}(X)-\mathcal{A}(X') = \mathcal{F}(X)-\mathcal{F}(X')$. A measurement of $\delta\mathcal{A} = \mathcal{A}(X)-\mathcal{A}(X')$ therefore gives a direct evaluation of the corresponding $\delta\mathcal{F} = \mathcal{F}(X) - \mathcal{F}(X')$.

At a first-order transition, $\mathcal{F}(X)$ has pronounced double minima corresponding to two coexisting phases at $X = X_1$ and $X = X_2$ separated by a barrier with a maximum at $X_{max}$ corresponding to a domain boundary between the two phases. The height of the barrier measures the interfacial free energy between the two coexisting phases and is given by

$$\delta\mathcal{F} = \mathcal{F}(X_{max}) - \mathcal{F}(X_1) \sim L^{d-1}. \tag{2.20}$$

Therefore, an increase in $\delta\mathcal{F}$ with increasing $L$ implies a first-order transition whereas a decreasing $\delta\mathcal{F}$ which vanishes at large $L$ implies the absence of a transition. Finally a constant $\delta\mathcal{F}$ indicates the occurrence of a continuous transition. This method is used widely in the following chapters for the identification of the nature of the phase transition for a variety of microscopic models.

# Chapter 3

# Model for Nematic Liquid Crystals

In this chapter, we present the results of extensive Monte Carlo simulations of a thermotropic liquid crystal model, the Lebwohl-Lasher model, for both transitional properties and director fluctuations. These results will be compared with experimental observations.

## 3.1 Introduction

Nematic liquid crystals differ structurally from normal isotropic liquids only in the spontaneous orientation of the molecules with their long axes parallel. In the absence of orienting fields, the preferred direction of the long axes is not constant over large areas, but varies continuously with position in real space (Saupe, 1968). However a complete understanding of the nature of intermolecular interactions is not available. Maier and Saupe (Maier and Saupe, 1959; Maier and Saupe, 1960) proposed a simple model for the nematic–isotropic phase transition. It was assumed that the interactions between molecules are dependent on both their positions, $\vec{r}$, and relative orientations, $\theta_{\vec{r}\vec{r}'}$, through the Legendre polynomial, $P_2(x)$, which describes the orientational ordering of the molecules. The interaction term can then be written as follows

$$J = -\epsilon(|\vec{r} - \vec{r}'|)P_2(\cos\theta_{\vec{r}\vec{r}'}). \qquad (3.1)$$

Since $P_2(x)$ is the lowest term in the expansion of $x$ for an uniaxial function, it can be considered as the simplest expression for interactions between molecules in the nematic phase of liquid crystals. Maier-Saupe theory in the mean field approximation is equivalent to the Landau-de Gennes theory (de Gennes, 1974) in which the nematic order in liquid crystals is characterized by a second-rank tensor order parameter, **Q**, and the free energy is expanded in components of this order parameter as follows

$$F = F_o + \frac{1}{2}A(T)Q_{\alpha\beta}Q_{\beta\alpha} + \frac{1}{3}B(T)Q_{\alpha\beta}Q_{\beta\gamma}Q_{\gamma\alpha} + \mathcal{O}(Q^4). \qquad (3.2)$$

In contrast to the dipolar symmetry of ferromagnets, the sign of the order parameter is important in a nematic. **Q** and $-\mathbf{Q}$ correspond to positive and negative birefringence and hence to quite different physical arrangements of the molecules. Therefore there is a term of order $\mathbf{Q}^3$ in the free energy for the purely geometrical reasons. Symmetry does not forbid a third-order invariant in $F$ and this implies that the model should exhibit a first-order transition. Although the mean-field solution to the Maier-Saupe model is consistent with most of experimental observations for the nematic–isotropic phase transition, it fails to estimate the spinodal temperature, $T_-^*$, which marks the stability limit of the isotropic phase. The result for $T_-^*$ is displaced relative to the equilibrium transition temperature, $T_c$, by $(T_c - T_-^*)/T_c \sim 10^{-1}$ which is almost two orders of magnitude larger than typical experimental values (de Gennes, 1974; Stinson and Litster, 1970; Thoen, Marynissen and Van Dael, 1982).

The following approach to the Maier-Saupe model was proposed by Lebwohl and Lasher (Lebwohl and Lasher, 1972) in 1972. They introduced the lattice version of the Maier-Saupe model in order to define the simplest possible microscopic lattice model of a regular array of rotor variables that has an orientational transition. Only nearest-neighbor interactions needed to be considered since the factor of $\epsilon(|\vec{r} - \vec{r}'|)$ in Eq. (3.1) was found to decay very rapidly with increasing distance between molecules (Lasher, 1970). In the Lebwohl-Lasher model, therefore, the rotor variables are coupled by the

Hamiltonian

$$\mathcal{H} = -\epsilon_2 \sum_{i,j} P_2(\cos\theta_{ij}), \tag{3.3}$$

where $P_2(\cos\theta_{ij}) = \frac{1}{2}(3\cos^2\theta_{ij} - 1)$, $\theta_{ij}$ is the angle between the axes of rotors at nearest-neighbor sites $i$ and $j$, and $\epsilon_2$ is a coupling parameter. The rotors are continuous variables and since the interaction in Eq. (3.3) is fully isotropic there is no coupling between the orientational properties and any preferred spatial directions. Below the equilibrium phase transition temperature, $T_c$, the orientational isotropy is broken and an orientationally ordered phase characterized by the nematic order parameter is formed. Even though the Lebwohl-Lasher model neglects the coupling between positional degrees of freedom and molecular orientation which is present in real nematogens, the orientational transition in the Lebwohl-Lasher model is believed to resemble the nematic–isotropic phase transition in liquid crystals (de Gennes, 1974).

The nature and the properties of the nematic–isotropic phase transition in the Lebwohl-Lasher model have been under active investigation since 1972 both in three (Lebwohl and Lasher, 1972; Lebwohl and Lasher, 1973; Lasher, 1972; Luckhurst and Simpson, 1982; Fabbri and Zannoni, 1986; Zannoni, 1986; Biscarini *et al.*, 1991; Cleaver and Allen, 1991; Zhang, Mouritsen and Zuckermann, 1992b; Zhang *et al.*, 1992b; Zhang, Zuckermann and Mouritsen, 1992; Cleaver and Allen, 1992) and two spatial dimensions (Chiccoli, Pasini and Zannoni, 1988). Strong numerical evidence for a first-order transition in the three-dimensional Lebwohl-Lasher model has been presented (Fabbri and Zannoni, 1986; Zannoni, 1986) but only recently (Zhang, Mouritsen and Zuckermann, 1992b) has unambiguous evidence for the first-order nature of the transition as presented below been found using the latest advances in numerical Monte Carlo simulation techniques described in Sec. 2.2 and Sec. 2.3.2. From these calculations (Zhang, Mouritsen and Zuckermann, 1992b) it was found that the Lebwohl-Lasher model can account for the close proximity of the experimentally observed stability limit of the isotropic phase to the transition point and that the Maier-Saupe mean-field approximation grossly overestimates the range of metastable states in the model.

The computational problems arising in studies of the orientational-ordering transition in the Lebwohl-Lasher model are related to the strong pretransitional effects which make it difficult to reveal the nature of the transition and to accurately determine the transitional properties. In particular it is troublesome to calculate the limits of stability of the two phases, *i.e.* to locate the spinodal points. In Sec. 3.3 we describe the results of extensive Monte Carlo computer-simulation calculations on the three-dimensional Lebwohl-Lasher model involving a determination of order-parameter distribution functions which permit free-energy functions to be derived. From a finite-size scaling analysis of these functions the nature of the orientational transition is shown to be of first order. The first-order transition is, however, extremely weak with strong precursor effects. From the variation of the free energy around the equilibrium transition temperature, it is possible to derive the limits of stability (the spinodal points) of the nematic and isotropic phases. The spinodal points are found to be extremely close ($\sim 10^{-3}$) to the equilibrium transition temperature, $T_c$. Results are also presented for the specific heat, the axial and biaxial susceptibilities, as well as the enthalpy and discontinuity in the nematic-order parameter at the transition. It is also shown (Zhang, Zuckermann and Mouritsen, 1992) that inclusion of a term $P_4(\cos\theta_{ij})$ in the Hamiltonian,

$$\mathcal{H} = -\epsilon_2 \sum_{i,j} P_2(\cos\theta_{ij}) - \epsilon_4 \sum_{i,j} P_4(\cos\theta_{ij}), \tag{3.4}$$

where $P_4(\cos\theta_{ij}) = \frac{1}{8}(35\cos^4\theta_{ij} - 30\cos^2\theta_{ij} + 3)$ is the 4th order Legendre polynomial, enhances the first-order character of the transition and leads to a displacement of the limits of stability away from $T_c$.

We have also investigated the director fluctuations in the Lebwohl-Lasher model by simulating equilibrium time series of the nematic director and its magnitude, the nematic order parameter. The results are described in Sec. 3.4. From a statistical analysis of these time series in terms of the auto-correlation function, $C(t)$, and the power spectrum, $P(f)$, of the accumulated fluctuations we have obtained the following results: (i) the correlation of the director fluctuations scales as $C(t) \sim t^{2H}$ and the power spectrum as $P(f) \sim f^{-(2H+1)}$ with the value of the Hurst exponent being $H \simeq 1$ for all temperatures in the nematic phase, (ii) in the isotropic phase, $C(t)$ scales as $C(t) \sim t^{2H}$ and $P(f)$ scales as $P(f) \sim f^{-(2H+1)}$ with $H \simeq 0.5$ independent of temperature, and (iii) in the presence of a unidirectional ordering field, $-h^2 \cos^2 \theta_i$, there is a crossover from $H \simeq 1$ to $H \simeq 0.5$ in the nematic phase, whereas the presence of the field does not affect the Hurst exponent in the isotropic phase. For comparison we show that the correlation function of the order-parameter fluctuations and the corresponding power spectrum is characterized by a Hurst exponent, $H \simeq 0.5$, independent of the phase, independent of the temperature, and independent of the presence of an ordering field. These results show that the director fluctuations exhibit fractional Brownian motion (Mandelbrot, 1982; Feder, 1988; Feder, 1991), *i.e.* $H > \frac{1}{2}$, in the nematic phase whereas whenever the continuous degeneracy is broken, the fluctuations follow ordinary Brownian motion, *i.e.* $H = \frac{1}{2}$. The field-induced crossover between fractional and normal Brownian motion is consistent with the findings from a recent neutron-scattering study of the nematogen d-PAA (deuterated para-azoxy-anisole) (Zhang *et al.*, 1992b; Otnes and Riste, 1992).

## 3.2 Details of the Simulations

We used the Metropolis Monte Carlo computer-simulation method, described in Sec. 2.1.4, to determine a canonical equilibrium ensemble of microstates for the Lebwohl-Lasher model. In the Lebwohl-Lasher model, the orientation of the $i$th rotor can be described by a unit vector, $\mathbf{u}_i$, which is stored as $\cos\theta_i$ and $\phi_i$ in our simulations for the phase transitional properties, where $\theta_i$ and $\phi_i$ are the polar and azimuthal angle of the symmetry axis of the rotor. On a simple cubic lattice with linear size, $L$, the microstate of system is given by the set of $N$ such orientations, $\{\phi_i, \theta_i\}$, where $N = L^3$ is the number of rotors. The angle between the symmetry axes of rotors $i$ and $j$, $\theta_{ij}$, is determined by the polar angles of the rotors, *i.e.* $\cos\theta_{ij} = \cos\theta_i \cos\theta_j + \sin\theta_i \sin\theta_j \cos(\phi_i - \phi_j)$. The periodic boundary conditions are imposed on the lattice in order to suppress the boundary effects. In order to generate a new microstate, we first chose rotors randomly and the orientations of the chosen rotors are then changed by generating two uniformly random values for $\cos\theta$ and $\phi$. Considering the uniaxial property of rotors, we chose $\cos\theta \in (0,1)$ and $\phi \in (0,2\pi)$ respectively. The acceptance rate is about 40% in our simulations.

Monte Carlo simulations are performed in three steps. First, simulations are performed to evaluate the specific heat, $C(T)$, and the susceptibility, $\chi(T)$, as functions of temperature. The results of these simulations are used to determine the peaks in $C(T)$ and $\chi(T)$ as accurately as possible. Secondly, very extensive simulations are then performed at the position of the peak of $C(T)$ or $\chi(T)$ for different values of the system size, $L$. These simulations involve 1 - $2\times10^6$ Monte Carlo steps per site (MCS). The basic thermal averages over a microstate are calculated and stored every 20 MCS.

The basic thermal quantities are the internal energy per rotor, $E(T) = \langle\mathcal{H}\rangle/N$, and the nematic order parameter. The value of nematic order parameter is determined as

$$\langle P_2\rangle = L^{-d}\left\langle\sum_i\left(\frac{3}{2}\cos^2\theta_i - \frac{1}{2}\right)\right\rangle, \tag{3.5}$$

where $\theta_i$ is the angle between the axis of the $i$th rotor molecule and the nematic director. Due to the non-broken continuous symmetry of the nematic ordering, the direction of the nematic director varies and has to be determined during the simulation in order to calculate $\langle P_2\rangle$. This is facilitated by diagonalization of the tensor order parameter **Q**,

$$Q_{\alpha\beta} = L^{-d}\sum_i\left(\frac{3}{2}n_{\alpha,i}n_{\beta,i} - \frac{1}{2}\delta_{\alpha\beta}\right), \quad \alpha,\beta = x,y,z, \tag{3.6}$$

where $n_{\alpha,i}$ is the $\alpha$-component of a unit vector, $\mathbf{n}_i$, which specifies the orientation of the $i$th molecule. The instantaneous value of the order parameter is then given by the largest eigenvalue, $\lambda_1$, of **Q** (Zannoni, 1986). The corresponding eigenvector, **n**, determine the direction of the nematic director. From the two smaller eigenvalues, $\lambda_2$

and $\lambda_3$, of the order-parameter tensor the biaxial susceptibility, $\delta(T)$, can be derived

$$\delta(T) = \langle|\lambda_2 - \lambda_3|\rangle. \tag{3.7}$$

On the basis of the data, the nature of transition can be determined by using the Lee-Kosterlitz method described in Sec. 2.3.2 and the properties of system near transition temperature are calculated by using the method of Ferrenberg and Swendsen described in Sec. 2.2. The thermodynamic order parameter is obtained as the average,

$$\langle\lambda_1\rangle \equiv \langle P_2\rangle_\lambda. \tag{3.8}$$

The response functions like the specific heat and the ordering susceptibility, $C(T)$ and $\chi(T)$, are calculated according to the fluctuation–dissipation theorem [Eqs. (2.5) and (2.6)]. Furthermore, free energies, $\mathcal{F}(E,T,L)$ and $\mathcal{F}(\lambda,T,L)$, are obtained as

$$\begin{aligned} \mathcal{F}(E,T,L) &\sim -\ln\mathcal{P}(E,T,L) \\ \mathcal{F}(\lambda,T,L) &\sim -\ln\mathcal{P}(\lambda,T,L) \end{aligned} \tag{3.9}$$

where the energy and the order-parameter distribution functions, $\mathcal{P}(E,T,L)$ and $\mathcal{P}(\lambda,T,L)$, can be derived from the data.

## 3.3 Results for Transition Properties

### 3.3.1 Response Functions: Susceptibilities and Specific Heat

Fig. 3.1 shows the data for the susceptibility, $\chi(T)$, as functions of temperature and system size for a range of temperatures in the transition region. A similar plot for the specific heat, $C(T)$, is shown in Fig. 3.2. The two functions exhibit a pronounced maximum signaling the orientational transition. The maximum increases as a function of system size for both functions and the position of the maximum moves correspondingly towards lower temperatures. The inserts of Figs. 3.1 and 3.2 show that the maxima scale with system size in such a way that the scaling forms, Eq. (2.17) are approximately obeyed. The data for $\chi_L^{\max}$ clearly approach the scaling regime earlier than the data for $C_L^{\max}$. Hence we conclude that the expected scaling relations for a first-order transition hold. Even though the maximum value of the response functions appears to have approached the asymptotic scaling regime, the full functional form of the two functions are not in the scaling regime for the system sizes investigated. This is demonstrated in Fig. 3.3 which shows plots of $CL^{-d}$ and $\chi L^{-d}$ vs the scaling variable, $\Delta T L^d$. Here $\Delta T = T - T_c(L)$ and the finite-size transition temperature, $T_c(L)$, is defined as the position of the peak of the response function in question. Again even though the data for the susceptibility appear to scale approximately over a range of temperatures in the transition region, the data for the specific heat are not yet in the scaling regime.

### 3.3.2 Internal Energy and Nematic Order Parameter

Fig. 3.4 shows the simulation data for the internal energy per rotor, $E(T)$, and the orientational order parameter, $\langle P_2(T)\rangle_\lambda$ in Eq. (3.5), for a wide range of temperatures. Only results for the two largest system sizes studied are exhibited. These figures clearly show that the transition is so strongly influenced by fluctuations that the variation of both the internal energy and the order parameter is smooth and effectively continuous throughout the transition region even for the largest system size.

### 3.3.3 Nature of the Nematic–Isotropic Phase Transition

The data for the free energy functionals, Eq. (3.9), for different system sizes calculated at temperatures, $T_c^{\mathcal{F}}(L)$, were determined by matching local minima in $\mathcal{F}(\lambda, T, L)$ and are displayed in Fig. 3.5. The finite-size behavior of $\mathcal{F}(\lambda, T, L)$ in Fig. 3.5(a) is quite clear: as the system size is increased, a double-well structure develops in the free energy. This is conclusive numerical evidence in favor of a first-order phase transition (Sec. 2.3.2). Since the barrier between the two minima is well pronounced for the two larger system sizes only, we have insufficient data to find the exact scaling behavior of the barrier height, cf. Eq. (2.20). This shows that the first-order transition is very weak. In fact it is considerably weaker than the first-order transitions in the three-dimensional three-state Potts model (Lee and Kosterlitz, 1991a; Stephanov and Tsypin, 1991) and the two-dimensional five-state Potts model (Lee and Kosterlitz, 1990) which are well known to exhibit weak first-order transitions. The free energy functional, $\mathcal{F}(E,T,L)$ in Fig. 3.5(b), derived for the internal energy distribution function is found to be a much weaker indicator of the nature of the orientational transition for the system sizes studied. A two-well behavior has barely developed for the largest system size. However, the strong deviation from a Gaussian shape suggests that a barrier is about to develop.

The first-order nature of the phase transition is further supported by the scaling behavior of the susceptibility maximum in Fig. 3.1, cf. Eq. (2.17).

### 3.3.4 Equilibrium Transition Temperature

Fig. 3.6 shows the results for the different measures of the finite-system phase transition temperature and how they scale with system size. The finite-system transition temperatures are defined from the position of the maximum in the specific heat, $T_c^C(L)$, from the position of the maximum in the susceptibility, $T_c^\chi(L)$, and from the criterion that the two minima in the free energy are equally deep, $T_c^{\mathcal{F}}(L)$. For finite systems, these three different measurements of the transition temperature have different values, but they all should approach the same value in the thermodynamic limit, $L \rightarrow \infty$. The data in Fig. 3.6 show that this is indeed the case. Furthermore, Fig. 3.6 demonstrates that the finite-size scaling relation,

$$\Delta T = T_c - T_c(L) \sim L^{-d}, \tag{3.10}$$

expected to hold at a first-order phase transition, applies. Extrapolation to the thermodynamic limit yields the following estimate of the equilibrium first-order transition temperature, $T_c = (1.1232 \pm 0.0001)\epsilon_2/\mathrm{k_B}$.

The transition temperature obtained from an earlier high-precision Monte Carlo simulation study of the Lebwohl-Lasher model (Fabbri and Zannoni, 1986), $T_c =$

$(1.1232 \pm 0.0006)\epsilon_2/k_B$, was obtained from an analysis of the finite-size behavior of the specific heat. This value is identical to the value obtained here. As indicated by the data in Fig. 3.6, the size-dependence of $T_c^{C}(L)$ is less pronounced in the scaling regime than that of $T_c^{\chi}(L)$ and $T_c^{\mathcal{F}}(L)$ and hence highly accurate values of the transition temperature can be obtained directly from specific-heat data for large systems as seen in Ref. (Fabbri and Zannoni, 1986).

### 3.3.5 Location of Pseudo-Spinodal Points: Stability Limits of the Isotropic and Nematic Phases

We now turn to a discussion of the pretransitional effects (de Gennes, 1974) near the orientational transition. The extremely weak emergence of the first-order orientational transition in the Lebwohl-Lasher model suggests that the fluctuations of the nematic order in the transition region are controlled by singularities from nearby critical-points which lie at the termini of the metastable branches of the free energy. The use of distribution functions, such as $\mathcal{P}(\lambda, T, L)$, and the derived free-energy functional, $\mathcal{F}(\lambda, T, L)$ in Eq. (3.9), allows us to make a detailed study of the limits of stability of both the nematic and the isotropic phase. These limits of stability are not rigorously defined for a system with short-range interactions (Gunton, San Miguel and Sahni, 1983) but correspond to relatively blurred regions. Hence we refer here to these limits, $T_{\pm}^{*}$, as pseudo-spinodal points rather than spinodal points. $T_{-}^{*}$ denotes the stability limit of the isotropic phase within the nematic phase and $T_{+}^{*}$ denotes the stability limit of the nematic phase within the isotropic phase.

The numerical data from which the pseudo-spinodal points, $T_{\pm}^{*}(L)$, are determined are shown in Fig. 3.7. The free energy is displayed in this figure for the largest system size studied, $L^3 = 28^3$, and for different values of the temperature around the equilibrium transition temperature. The figure shows the 'classic' behavior of a free-energy function near a first-order transition as usually presented from the Landau theory (Stanley, 1971). The pseudo-spinodal points in the finite system are estimated as the temperatures where the second, local minima of the free energy vanish when the temperature is varied away from the transition temperature.

The pseudo-spinodal points, $T^*_\pm$, in the thermodynamic limit have been determined from an empirical extrapolation, as indicated in Fig. 3.6. We note that we have no rigorous basis for this type of finite-size scaling behavior of $T^*_\pm(L)$. Presumably a more rigorous scaling analysis should involve the exponents characterizing the pseudo-spinodal singularities. Therefore, the quoted estimates of $T^*_\pm$ should be considered as maximal displacements of the pseudo-spinodal points from the transition. The main result obtained from Fig. 3.6 is that the pseudo-spinodal points are extremely close to the equilibrium transition temperature,

$$|T_c - T^*_\pm|/T_c \lesssim 0.5 \times 10^{-3}. \tag{3.11}$$

Within the numerical accuracy of our data, the two pseudo-spinodal points are equally close to the transition point.

We wish to remark that we have only been able to obtain these results for the pseudo-spinodal points due to the availability of methods such as the powerful reweighting technique by Ferrenberg and Swendsen (Sec. 2.2). By this method it becomes feasible to generate numerical data for the free energy, cf. Figs. 3.5 and 3.7. These data give detailed insight into the non-equilibrium properties of a system which undergoes such a weak first-order transition as the three-dimensional Lebwohl-Lasher model. This is probably the reason why earlier numerical work on systems as large as $30^3$ molecules (Fabbri and Zannoni, 1986) on the model using more conventional techniques, but also involving distribution functions, had difficulty in matching the two free-energy minima. In the work by Fabbri *et al.* (Fabbri and Zannoni, 1986) the stability limit of the isotropic phase was investigated by an extrapolation analysis of an Ornstein-Zernike expression for the pair correlation function. The result found for a $30^3$ system, $(T_c - T^*_-)/T_c \simeq 3 \times 10^{-3}$, is in an order-of-magnitude agreement with the value obtained in the present calculation which indicates that the assumptions underlying the work in Ref. (Fabbri and Zannoni, 1986) are reasonable.

### 3.3.6 Transition Enthalpy, Nematic-Order Discontinuity, and Biaxial Susceptibility

The value of the transition enthalpy, $\Delta H = \int C(T)\mathrm{d}T$, can be estimated from the finite-size scaling behavior of the specific heat. From the data for the larger system sizes studied we estimate that $\Delta H \simeq (0.20 \pm 0.04)\epsilon_2$. There is another way to estimate the transition enthalpy since, in the thermodynamic limit, the separation between two minima of $\mathcal{F}(E)$ would directly amount to $\Delta H$. However, as remarked earlier, we have found that the specific heat approaches the scaling regime much slower than the susceptibility does. The distribution function for the internal energy in the transition region is strongly non-Gaussian for the larger system sizes studied, but as seen in Fig. 3.5(b) two clear minima cannot be discerned within the accuracy of the data. We are therefore not able to determine the transition enthalpy with high precision.

The value of the discontinuity in the nematic order parameter, $\Delta\langle P_2\rangle_\lambda$, at the first-order transition was determined from an empirical finite-size scaling analysis at the equilibrium transition temperature. The data for $\langle P_2\rangle_\lambda$ in a wide temperature range were shown in Fig. 3.4(a). From this figure we have obtained the estimate $\Delta\langle P_2\rangle_\lambda \simeq 0.39$ at the transition. It should be noted that the approach to the thermodynamic limit for this quantity is extremely slow implying that our estimate is somewhat tenuous. The position of the upper minimum in the free-energy function, $\mathcal{F}(\lambda, T, L)$ in Fig. 3.5(a), show only a very weak size dependence.

The biaxial susceptibility, $\delta(T)$ in Eq. (3.7), is zero by symmetry in the thermodynamic limit for the isotropic Lebwohl-Lasher model. However, for a finite system there is a non-zero difference between the two smaller eigenvalues of the nematic order parameter tensor and $\delta(T)$ will attain a finite value and have a non-trivial and interesting temperature dependence. Since there is some interest in the behavior of nematic droplets, we show in Fig. 3.8 data for two different system sizes. As expected, $\delta$ decreases for increasing system size and will vanish in the limit $L \rightarrow \infty$. It is seen that $\delta(T)$ is very weak compared to the order-parameter susceptibility in Fig. 3.1 but it has a sharp cusp-like maximum at the transition. Furthermore, $\delta(T)$ is highly asymmetric around the transition.

### 3.3.7 Enhancement of a Weakly First-Order Phase Transition

As shown above, the first-order transition in the Lebwohl-Lasher model of Eq. (3.3) is extremely weak and associated with strong pretransitional effects, stability limits and pseudo-spinodal points which are very close to the equilibrium transition temperature. We now show that by adding to the Hamiltonian a term, $P_4(\cos\theta_{ij})$ in Eq. (3.4), which does not break the continuous degeneracy of the orientational ordering, the first-order character of the transition is enhanced. Fig. 3.9(a) shows the data for the free energy $\mathcal{F}(\lambda, T, L)$ as a function of system size evaluated at the transition temperatures, $T_c^{\mathcal{F}}(L)$, for the case of $\epsilon_4/\epsilon_2 = 0.1$. The free-energy barrier develops and increases in height as the system size is increased. This demonstrates that the transition is of first order as in the absence of the $P_4$-term. We used a finite-size scaling analysis to estimate the equilibrium transition temperature in the case $\epsilon_4/\epsilon_2 = 0.1$ to be $T_c = (1.1628 \pm 0.0001)\epsilon_2/k_B$. By comparing Fig. 3.9(a) with the analogous data in Fig. 3.5 for $\epsilon_4 = 0$, it is seen that the barrier height for the same system sizes is larger when the $P_4$-term is present. This is demonstrated in Fig. 3.9(b) which for a large system size, $L = 24$, shows a comparison between $\mathcal{F}(\lambda, T, L)$ for the two cases. From this figure we conclude that the $P_4$-terms acts so as to enhance the first-order character of the transition: not only the barrier height (*i.e.* interfacial tension) but also the distance between the two minima increases with system size.

When the first-order transition in the Lebwohl-Lasher model is made more strongly first order by adding the $P_4$-term, the pseudo-spinodal points, and hence the stability limits of the two phases, are further displaced from the equilibrium transition temperature. This is illustrated in Fig. 3.10 in the case of $\epsilon_4/\epsilon_2 = 0.1$. This figure should be compared with Fig. 3.7 for $\epsilon_4 = 0$. From a finite-size analysis similar to that described in Sec. 3.3.5 we estimated that the pseudo-spinodal points for $\epsilon_4/\epsilon_2 = 0.1$ are positioned at $|T_c - T_\pm^*|/T_c \lesssim 0.8 \times 10^{-3}$.

Our finding of an enhancement of the first-order character of the orientational transition of the Lebwohl-Lasher model in the presence of the $P_4$-term is consistent with earlier mean-field (Zannoni, 1979) and conventional Monte Carlo simulation studies (Chiccoli *et al.*, 1988; Fuller, Luckhurst and Zannoni, 1985).

## 3.4 Results for Director Fluctuations

A renewed interest in the study of temporal fluctuations in complex dynamical systems has emerged since Mandelbrot (Mandelbrot, 1982) introduced the concept of fractional Brownian motion. In contrast to ordinary Brownian motion which reflects independent stochastic processes, fractional Brownian motion implies persistence or anti-persistence and power-law correlations in the fluctuations.

An interesting possibility for observing fractional Brownian motion in a cooperative many-particle system exists in the case of fluctuating modes in a symmetry-broken state of continuous degeneracy. A candidate for a system exhibiting this type of behavior is a liquid crystal within the nematic phase where the director fluctuations correspond to a dynamical mode which is critical for all temperatures in the nematic phase (de Gennes, 1974). We shall here show that the three-dimensional Lebwohl-Lasher model provides a convenient and simple model framework within which fractional Brownian motion and its consequences can be observed.

### 3.4.1 Time-Series Analysis and the Hurst Exponent

We used the standard interpretation of a Monte Carlo simulation via a Master-equation formulation to associate a time parameter (Markov time) with the sequence of states generated for the equilibrium ensemble by the stochastic Monte Carlo process (Sec. 2.1.5). Obviously, the associated time scale is not the true physical time scale since we have not invoked the true equation of motion. In particular we have not strictly unforced the conservation law for the nematic order parameter (de Gennes, 1974). However, the average of the orientational order parameter is conserved during the simulation and we assume in the following that the Monte Carlo time series have some relevance for the equilibrium nematodynamics. Since our elementary excitation is a single-site rotor reorientational process we basically study the overdamped regime of the dynamics.

We first calculated equilibrium time series of the nematic director, given by the components, $n_\alpha(t)$, of the unit eigenvector corresponding to the highest eigenvalue of Q, as well as the nematic order parameter, $\langle P_2\rangle_\lambda(t)$. The time is measured in units of Monte Carlo steps per lattice site (MCS). Time series were determined for different temperatures in both the nematic (Sec. 3.4.2) and the isotropic phase (Sec. 3.4.3) as well as in the presence of an ordering-field term (Sec. 3.4.4), $-h^2\cos^2\theta_i$, which was added to the Hamiltonian in Eq. (3.3).

The time series have been analyzed in terms of power spectra as well as by the rescaled-range ($R/S$) method (Mandelbrot, 1982; Feder, 1991) which was originally developed by Hurst (Hurst, 1951) to analyze statistical fluctuations of water levels in large natural reservoirs. In the case of a component, $n_\alpha$, of the nematic director, the $R/S$ analysis is based on a range

$$R = \max[X(t,\tau)] - \min[X(t,\tau)], \quad 0 \le t \le \tau \tag{3.12}$$

and an accumulated standard deviation

$$S = \left(\frac{1}{\tau}\sum_{t=1}^{\tau}[n_\alpha(t) - \langle n_\alpha\rangle_\tau]^2\right)^{1/2}, \tag{3.13}$$

where the average of the stochastic variable $n_\alpha(t)$ over the time range $\tau$ is

$$\langle n_\alpha\rangle_\tau = \frac{1}{\tau}\sum_{t=1}^{\tau} n_\alpha(t). \tag{3.14}$$

The accumulated fluctuations over the same time range are

$$X(t,\tau) = \sum_{t'=1}^{t}[n_\alpha(t') - \langle n_\alpha\rangle_\tau]. \tag{3.15}$$

$X(t,\tau)$ is the basic stochastic variable of the process we consider. An autocorrelation function, $C(t)$, for this variable can be defined as

$$C(t) = \langle X(0)X(t)\rangle. \tag{3.16}$$

The Hurst exponent, $H$, is defined as (Feder, 1991),

$$R/S \sim \tau^{H}, \tag{3.17}$$

or equivalently

$$C(t) \sim t^{2H}. \tag{3.18}$$

The corresponding scaling form for the power spectrum is

$$P(f) = |\int X(t) \exp(-i2\pi f t) \mathrm{d}t|^2 \sim f^{-\beta}. \tag{3.19}$$

Scaling implies the relation $\beta = 2H + 1$ (Feder, 1991). Statistical independence of stochastic events leads to $H = \frac{1}{2}$ and ordinary Brownian motion. In the case of $H \neq \frac{1}{2}$, the correlation function has power-law decay and infinitely long correlations. This latter case is associated with fractional Brownian motion (Mandelbrot, 1982). An equivalent formalism can be written down in the case of the time series for the nematic order parameter, $\langle P_2 \rangle_\lambda(t)$.

### 3.4.2 Fractional Brownian Motion of Director Fluctuations in the Nematic Phase

The director fluctuations are recorded in terms of the fluctuations in one of the components of the unit directional vector. All three components are found to behave statistically in a similar manner and we therefore only examine one of them. Furthermore, we found that the fluctuations in the polar angle also behave in the same manner. Fig. 3.11 shows untreated simulation data illustrating the director fluctuations both without ($h = 0$) and with a symmetry-breaking field ($h^2/\epsilon_2 = 1$). The top panel in Fig. 3.11 shows an example of one of the Cartesian components of the director for the two cases and the bottom panel shows blow-ups of a small part of the two time series for the same two cases. The figures show that the director fluctuations exhibit structure on all time scales and they illustrate the self-similar nature of the director fluctuations.

Data for the director fluctuations were analyzed by the $R/S$–method of Eqs. (3.12)–(3.17), and the results are shown in Fig. 3.12(a) for two different temperatures in the nematic phase. This figure demonstrates that the director fluctuations display a remarkably clear scaling behavior over a wide range of $\tau$. Both data sets are well described by a Hurst exponent, $H \simeq 1$, which implies fractional Brownian motion and long-range power-law correlations. This implies that the Hurst exponent is independent of temperature in the nematic phase.

The results of an analysis of the director fluctuations in terms of the power spectrum, Eq. (3.19), are given in Fig. 3.12(b) for a temperature in the nematic phase. Although the data for the power spectrum are much less smooth, they also provide evidence for power-law scaling. The data for the power spectrum are, however, not accurate enough to decide whether the scaling relation $\beta = 2H + 1$ breaks down.

### 3.4.3 Brownian Motion of Director Fluctuations in the Isotropic Phase

By contrast to our findings of fractional Brownian motion of director fluctuations in the nematic phase, the data for the director fluctuations in the isotropic phase in Fig. 3.13 demonstrate that ordinary Brownian motion, $H \simeq 1/2$, prevails over long times in the isotropic phase. Both the $R/S$–analysis shown in Fig. 3.13(a) and the analysis of the power spectrum shown in Fig. 3.13(b) give the same result, and the scaling relation, $\beta = 2H + 1$ appears to hold.

### 3.4.4 Field-Effects on Director Fluctuations

The continuous degeneracy of the nematic order can be broken by adding a uniaxial ordering field to the Hamiltonian,

$$\mathcal{H} = -\epsilon_2 \sum_{i,j} P_2(\cos\theta_{ij}) - h^2 \sum_i \cos^2\theta_i, \qquad (3.20)$$

where $h$ is the field strength and $\cos\theta_i$ is the angle between the axis of the $i$th rotor molecule. The average nematic director direction is then controlled by the direction of the applied field. In the presence of this field, the fractional Brownian motion in the nematic phase is destroyed and there is a crossover to ordinary Brownian motion over long time ranges. Fig. 3.14 also shows that the presence of the field in the isotropic phase does not alter the ordinary Brownian motion characteristics of the director fluctuations.

Fig. 3.15 gives the results of a closer study of the crossover effects induced by the applied field. It is seen that there are two time regimes in the fluctuation characteristics in the presence of the field. For short time ranges, the field has not yet made its influence felt on the director motions and an effective fractional Brownian motion with $H \simeq 1$ is observed. At longer time ranges a crossover to ordinary Brownian motion with $H \simeq 1/2$ takes place. The crossover occurs at shorter times the stronger the field is. At very high field strengths the signal saturates. In the crossover regime, effective Hurst-exponent values between 0.5 and 1 can be assigned to the data. As expected, this effective exponent is very sensitive to the sampling density employed whereas the limiting behaviors are not.

### 3.4.5 Effects on Director Fluctuations Due to Walls

We also simulated the effects of another type of symmetry-breaking field on the director fluctuations which is of relevance for interpreting certain experimental data. This type of field may be considered as due to a wall which imposes a local boundary condition on the nematic ordering. This type of boundary condition is only expected to have an effect on finite systems except near wetting transitions. In the present realization, the wall is simulated by fixing all rotors in an $x-y$ plane of the lattice to point along the $y-$axis. For lattices of the typical sizes we have studied in this chapter, the effect on the director fluctuations due to this particular type of boundary condition is shown in Fig. 3.16. From a $R/S$-analysis of the data an effective Hurst-exponent value of $H \simeq 0.82$ is obtained. The exponent value depends on the specific boundary condition and the size of the system.

### 3.4.6 Fluctuations of the Nematic Order Parameter

By contrast to the fluctuations in the nematic director (in the absence of a field) the fluctuations in the nematic order parameter correspond to independent stochastic processes and hence to ordinary Brownian motion ($H = \frac{1}{2}$) in either phase and independent of temperature, as illustrated by the data in Fig. 3.17. Both the $R/S$–analysis and the power spectra leads to $H \simeq 0.5$ for long times.

## 3.5 Comparison with Experiments

### 3.5.1 Transition Properties

In this section we compare our simulation results for the three-dimensional Lebwohl-Lasher model to relevant experimental data for the nematic–isotropic transition in liquid crystals. It should again be noted that the Lebwohl-Lasher model, being a lattice model, neglects the positional degrees of freedom of real nematics but the model should still capture the essential physics of the orientational degrees of freedom which are mainly responsible for the nematic–isotropic phase transition. It has been found (de Gennes, 1974; Stinson and Litster, 1970; Thoen, Marynissen and Van Dael, 1982) for a large number of room-temperature nematogens that the transition enthalpy and the relative stability limit of the isotropic phase are only slightly sensitive to the material in question. Hence it is reasonable to compare experimental results for such transitional properties with corresponding data obtained from the simple Lebwohl-Lasher model.

As a specific example we consider the liquid crystal octylcyanobiphenyl (8CB) (Stinson and Litster, 1970; Thoen, Marynissen and Van Dael, 1982). 8CB has been found experimentally to have the following transitional parameters, $T_c = 40.8°\mathrm{C}$ and $\Delta H = 612\mathrm{J/mol}$. From the experimental transition temperature we can determine the value of the energy parameter, $\epsilon_2$, which leads to $\Delta H = 460\mathrm{J/mol}$ for the Lebwohl-Lasher model. This is in reasonably good agreement with the model result.

Since nematics usually cannot be supercooled (Thoen, Marynissen and Van Dael, 1982), the experimental determination of the stability limit of the isotropic phase is not very accurate since it is obtained by extrapolation of the equilibrium data for the susceptibility or the specific heat from the isotropic phase into the nematic phase and vice versa. The experimental values (Stinson and Litster, 1970; Thoen, Marynissen and Van Dael, 1982) quoted for $|T_c - T_-^*|/T_c$ lie in the range $\sim 0.2 - 3 \times 10^{-3}$ which is in good agreement with our results from the Lebwohl-Lasher model. Hence one cannot discard the Lebwohl-Lasher model as a model of nematics on the basis of a large discrepancy between the experimental values of stability limits and the values obtained from Maier-Saupe theory, which provides the mean-field solution to the Lebwohl-Lasher model. Mean-field theory strongly underestimates both the fluctuations and the pretransitional effects in the Lebwohl-Lasher model and also predicts a first-order transition which is far too strong. It appears likely from the results presented in Sec. 3.3.7 on the enhancement effects due to the additional term, $P_4$, of the interactions that an extended Lebwohl-Lasher model, Eq. (3.4), with varying $\epsilon_4/\epsilon_2$, may account for the slight differences between the stability limits found for different nematogens.

### 3.5.2 Director Fluctuations

Recent neutron-scattering studies of director fluctuations in the nematic phase of d-PAA (deuterated para–azoxy–anisole) by Otnes and Riste (Zhang *et al.*, 1993; Otnes and Riste, 1992) found evidence for power-law correlations of the director fluctuations and hence fractional Brownian motion. Otnes and Riste analyzed the raw time-series data obtained from the scattering experiment using the same formalism as described in Sec. 3.4.1.

The first neutron-scattering study (Otnes and Riste, 1992) showed that the director fluctuations in the nematic phase exhibit scaling and fractional Brownian motion characterized by a Hurst exponent, $H = 0.74$, whereas ordinary Brownian motion applies in the isotropic and solid crystalline phases. In a later experiment (Zhang *et al.*, 1993), the conditions for the first experiment in the nematic phase were changed with a view to minimizing effects due to convection-flow alignment which tends to reduce the effective exponent of $H$. It was then found that the Hurst exponent value is close to $H \simeq 1$, in excellent agreement with the results from the Lebwohl-Lasher model, cf. Fig. 3.12. Furthermore, it was found in the experiment, where a symmetry-breaking magnetic field was applied, that lower effective values of $H$ result which tended towards $H \simeq 0.5$ for large field values. These results are consistent with the field-induced crossover phenomena found in the Lebwohl-Lasher model, cf. Fig. 3.15.

## 3.6 Conclusions

In this chapter we presented results from a combined numerical study of the phase transition and director fluctuations in the Lebwohl-Lasher model of the nematic–isotropic phase transition in liquid crystals.

We first exploited modern computer-simulation techniques described in Chapter 2 involving the Ferrenberg-Swendsen reweighting technique (Ferrenberg and Swendsen, 1988) in combination with the Lee-Kosterlitz finite-size scaling analysis (Lee and Kosterlitz, 1990; Lee and Kosterlitz, 1991b) in order to investigate the nature of the orientational phase transition in the three-dimensional Lebwohl-Lasher model. The methods of analysis operate on a level of the free-energy which makes it possible to examine the nature of the transition and to determine the transitional properties accurately. We found unambiguous evidence for a very weak first-order transition with stability limits extremely close to the equilibrium phase transition temperature. The results show that the Lebwohl-Lasher model gives a good description of those properties of the nematic–isotropic phase transition which are not particularly material dependent.

Secondly, we analyzed time-series data for the director fluctuations and found evidence for fractional Brownian motion of the director fluctuations in the nematic phase. As a symmetry-breaking field is applied, a crossover to ordinary Brownian motion is observed. These findings are in excellent agreement with recent neutron-scattering experiments on nematogens by Otnes and Riste (Zhang, Mouritsen and Zuckermann, 1992b; Otnes and Riste, 1992).

The physical interpretation of the numerical simulation of the director fluctuations are as follows. In a nematic, ordered phase, the director is subject to a continuous degeneracy since its direction is not coupled to the lattice and there is no activation barrier for directional rotation. Hence, the director field is subject to critical fluctuations and power-law correlations at all temperatures within the nematic phase (de Gennes, 1974). This leads directly to fractional Brownian motion of the director. In contrast, the nematic order parameter is not a critical mode, except at a singular temperature, the pseudo-critical point, where it displays power-law scaling. At all other temperatures the order-parameter fluctuations in both the nematic and the isotropic phase are short range effects and are associated with ordinary Brownian motion. The continuous degeneracy of the nematic director can be lifted by an ordering field, in which case the fluctuations become quenched and the mode is no longer critical. Ordinary Brownian motion then results over long time ranges as observed. At short times the symmetry-breaking field is not capable of destroying the power-law correlations and only for longer times is there a crossover to ordinary Brownian motion. This crossover occurs for shorter times the stronger the field is. A similar behavior can be expected for a number of other models with a continuous order-parameter degeneracy, including the three-dimensional Heisenberg ferromagnet where the fluctuations in the magnetization direction should also exhibit fractional Brownian motion. This is supported by the results from computer simulations on the Heisenberg model without conservation laws (Zhang, Mouritsen and Zuckermann, 1992c).

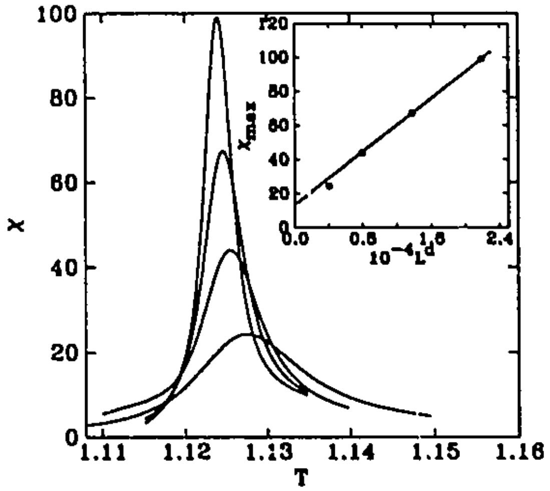

Figure 3.1: Ordering susceptibility, $\chi(T)$ (in units of $\epsilon_2^{-1}$), as functions of temperature, $T$ (in units of $\epsilon_2/k_B$), for four different lattice sizes, $L^3 = 16^3, 20^3, 24^3$, and $28^3$. The inserts show the finite-size scaling behavior of the maximum of $\chi(T)$.

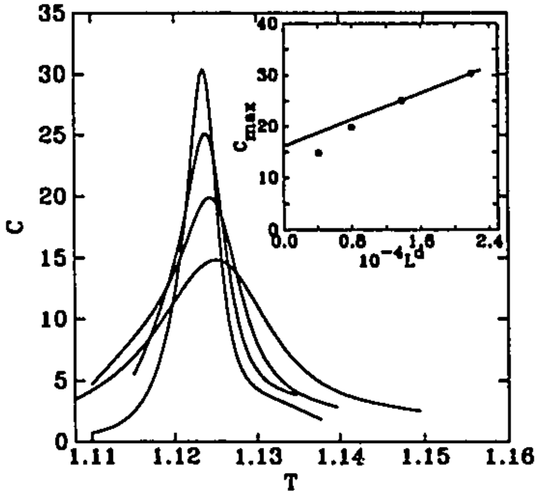

Figure 3.2: specific heat, $C(T)$ (in units of $k_B$), as functions of temperature, $T$ (in units of $\epsilon_2/k_B$), for four different lattice sizes, $L^3 = 16^3, 20^3, 24^3$, and $28^3$. The inserts show the finite-size scaling behavior of the maximum of $C(T)$.

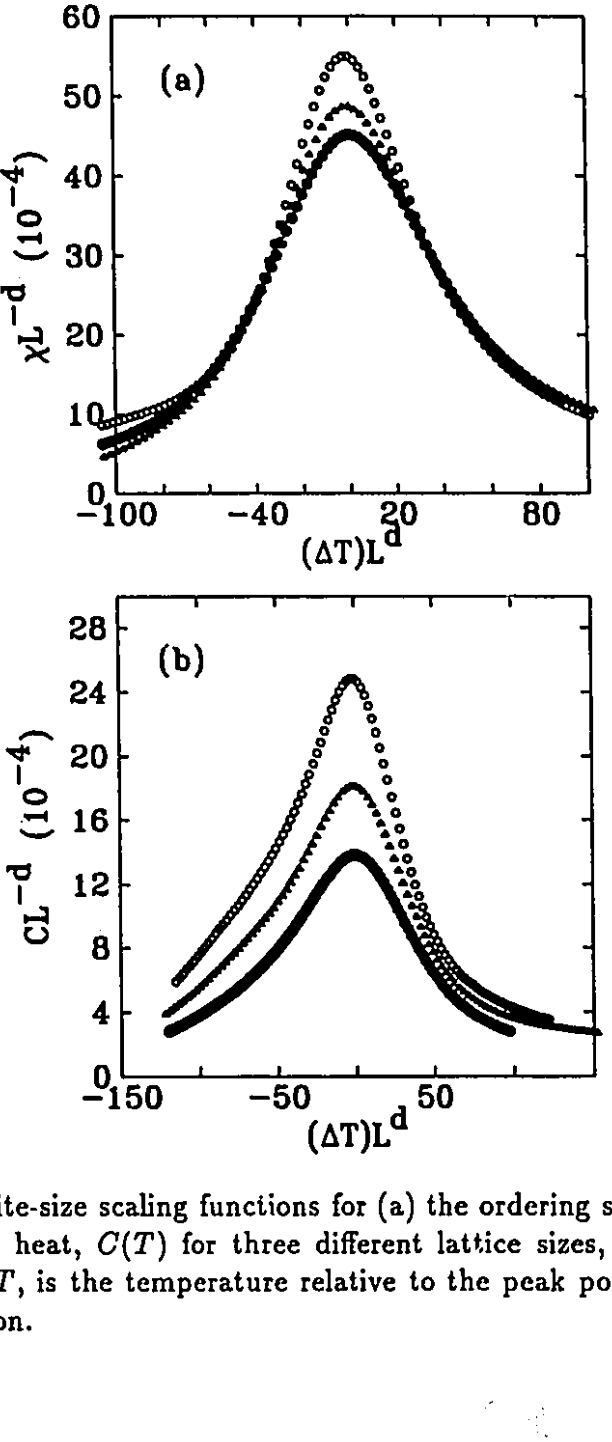

Figure 3.3: Finite-size scaling functions for (a) the ordering susceptibility, $\chi(T)$ and (b) the specific heat, $C(T)$ for three different lattice sizes, $L^3 = 20^3\,(\circ), 24^3\,(\triangle)$, and $28^3\,(\bullet)$. $\Delta T$, is the temperature relative to the peak position of the respective response function.

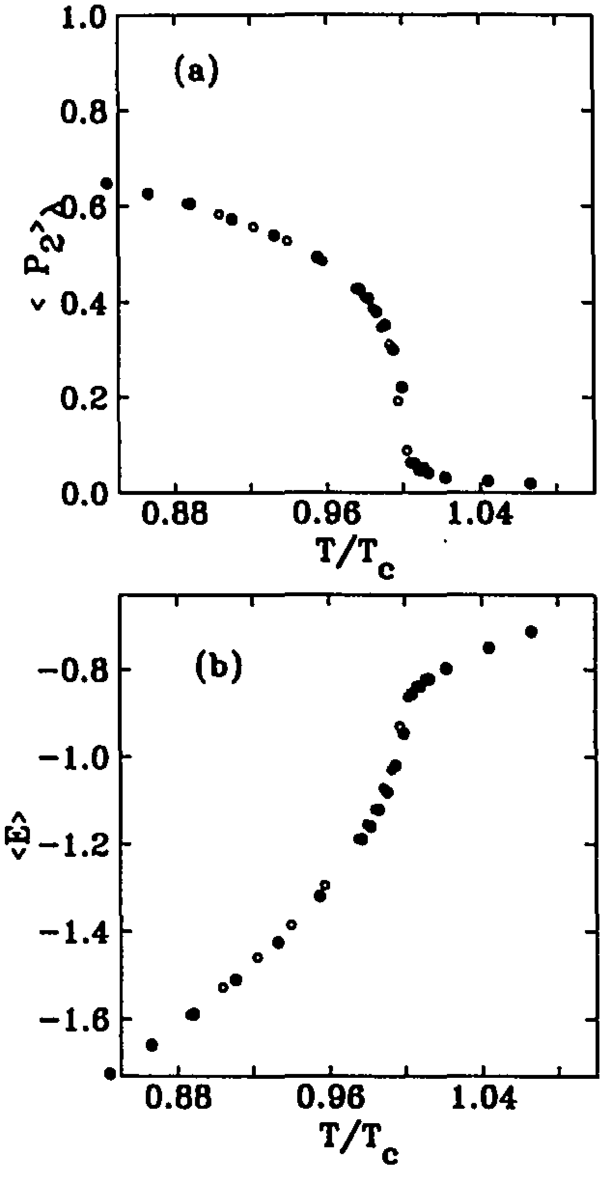

Figure 3.4: (a) Nematic order parameter, $\langle P_2 \rangle_\lambda$, and (b) internal energy per rotor, $E = \langle H \rangle$ (in units of $\epsilon_?$), as functions of reduced temperature, $T/T_c$, where $T_c$ is the transition temperature in the thermodynamic limit. Results are shown for two different lattice sizes, $L^3 = 24^3$ (o) and $28^3$ (•).

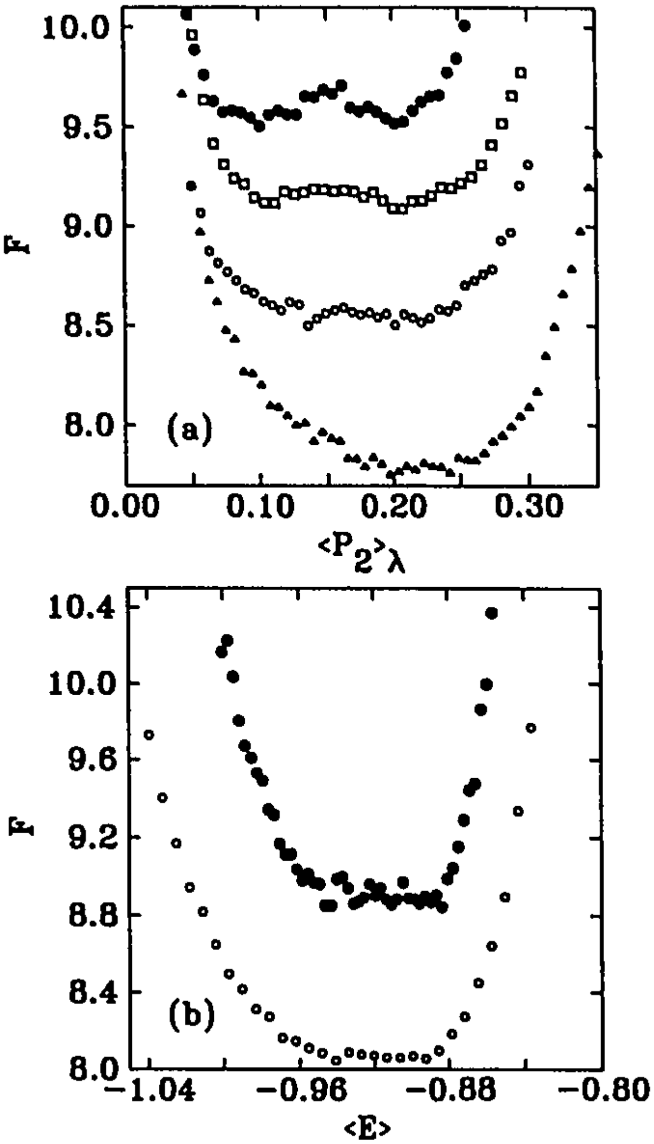

Figure 3.5: Free energy, $\mathcal{F}$ (in units of $\epsilon_2$), as a function of nematic order (a), $\langle P_2 \rangle_\lambda$, and as a function of internal energy (b), $E$, for four different lattice sizes, $L^3 = 16^3\,(\triangle), 20^3\,(\circ), 24^3\,(\square)$, and $28^3\,(\bullet)$. The different sets of data are displaced vertically for the sake of clarity.

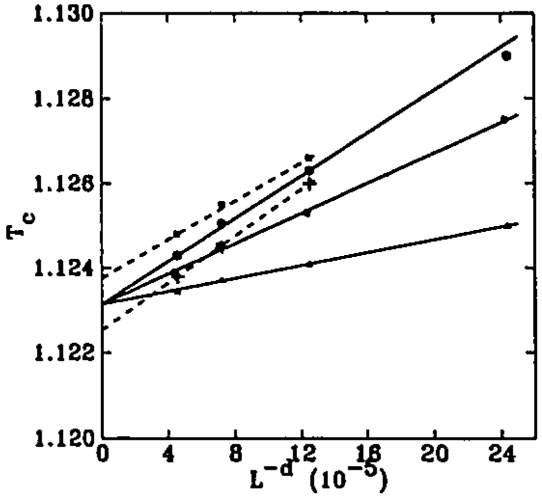

Figure 3.6: Finite-size scaling behavior shown for three different measures of the finite-system transition temperature, $T_c(L)$: $T_c^{\mathcal{F}}(L)$ (•), $T_c^{\chi}(L)$ (○), $T_c^{C}(L)$ (△). The estimates of the finite-size pseudo-spinodal points $T_-^*(L)$ (+) and $T_+^*(L)$ (□) are also shown. Extrapolations to the thermodynamic limits, $T_c(\infty)$ and $T_\pm^*(\infty)$ are denoted by solid and dashed lines respectively.

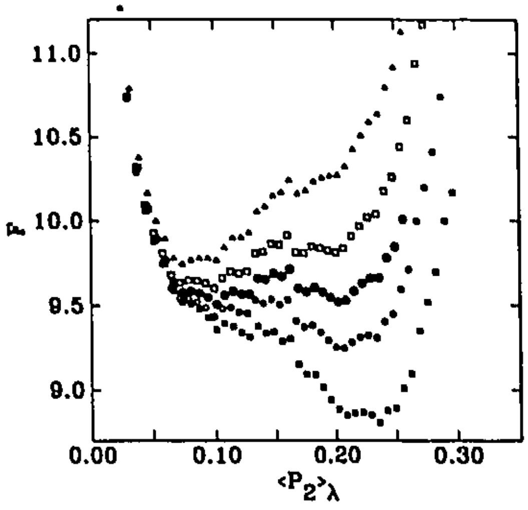

Figure 3.7: Free energy, $\mathcal{F}$ (in units of $\epsilon_2$), as a function of nematic order, $\langle P_2 \rangle_\lambda$, for a lattice with $L^3 = 28^3$ sites. Results are given corresponding to seven different temperatures near the nematic-isotropic transition. From bottom to top the temperatures (in units of $\epsilon_2/k_B$) are: 1.1238 (■), 1.1241 (○), 1.1243 (●), 1.1245 (□), and 1.1248 (△). The middle curve corresponds to the finite-size equilibrium transition temperature, $T_c(L)^{\mathcal{F}}$. The sets of curves in either direction away from the transition in either direction correspond to metastability and pseudo-spinodal behavior respectively. For the sake of clarity, the different sets of data are displaced vertically.

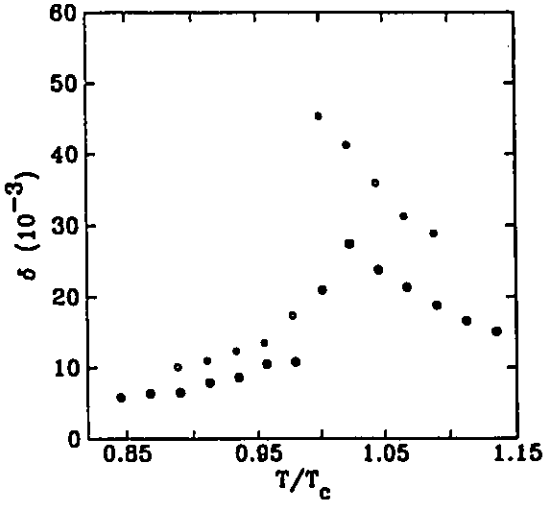

Figure 3.8: Biaxial susceptibility, $\delta(T)$, as a function of temperature for system sizes $L = 20^3$ (○) and $L^3 = 28^3$ (●).

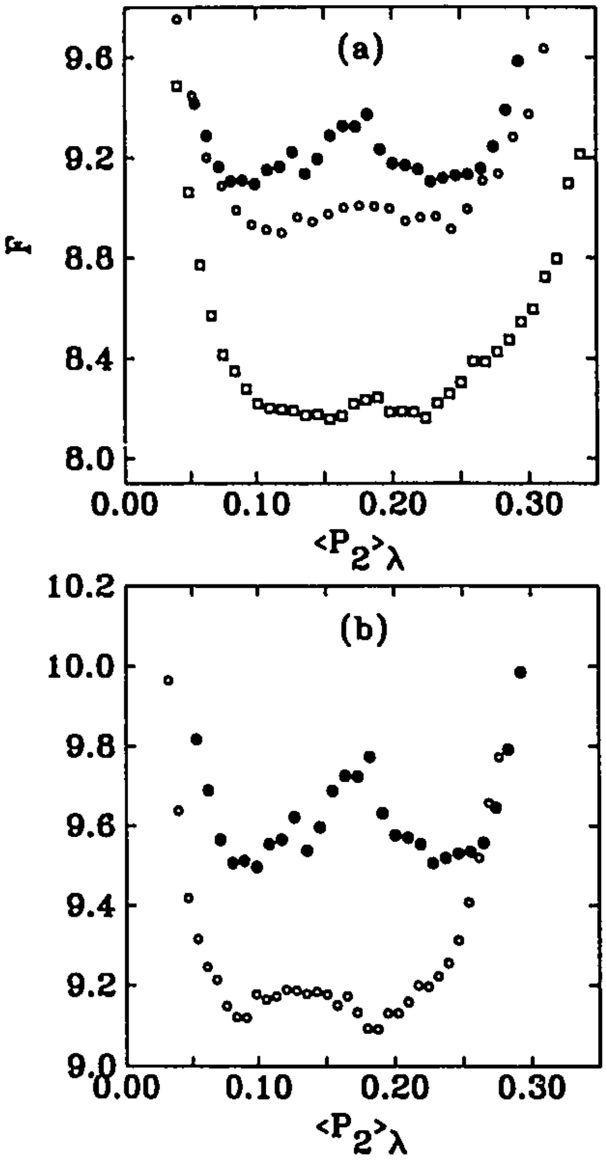

Figure 3.9: (a) Free energy, $\mathcal{F}$ (in units of $\epsilon_2$), as a function of nematic order, $\langle P_2 \rangle_\lambda$, for the Lebwohl-Lasher model in the presence of a term $P_4(\cos\theta_{ij})$ in the Hamiltonian, cf. Eq. (3.4), with $\epsilon_4/\epsilon_2 = 0.1$ for three different lattice sizes, $L^3 = 16^3\,(\square), 20^3\,(\circ)$, and $24^3\,(\bullet)$. (b) A comparison of the free-energy functions for a system of size $L^3 = 24^3$ in the case of $\epsilon_4/\epsilon_2 = 0\,(\circ)$ and $0.1\,(\bullet)$. For the sake of clarity, the different sets of data have been displaced vertically.

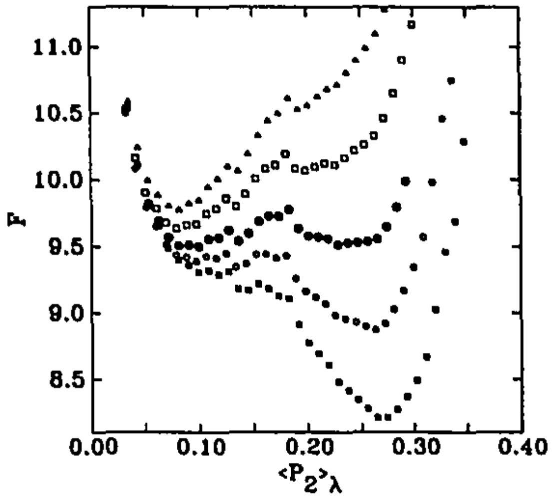

Figure 3.10: Free energy, $\mathcal{F}$ (in units of $\epsilon_2$), as a function of nematic order, $\langle P_2\rangle_\lambda$, for a lattice with $L^3 = 24^3$ sites in the case of $\epsilon_4/\epsilon_2 = 0.1$. Results are given corresponding to five different temperatures near the nematic-isotropic transition. From bottom to top the temperatures (in units of $\epsilon_2/k_B$) are: 1.1637 (□), 1.16415 (○), 1.1646 (●), 1.16505 (□), and 1.1655 (△). The middle curve corresponds to the finite-size equilibrium transition temperature, $T_c(L)^{\mathcal{F}}$. The sets of curves away from the transition in either direction correspond to metastability and pseudo-spinodal behavior, respectively. For the sake of clarity, the different sets of data have been displaced vertically.

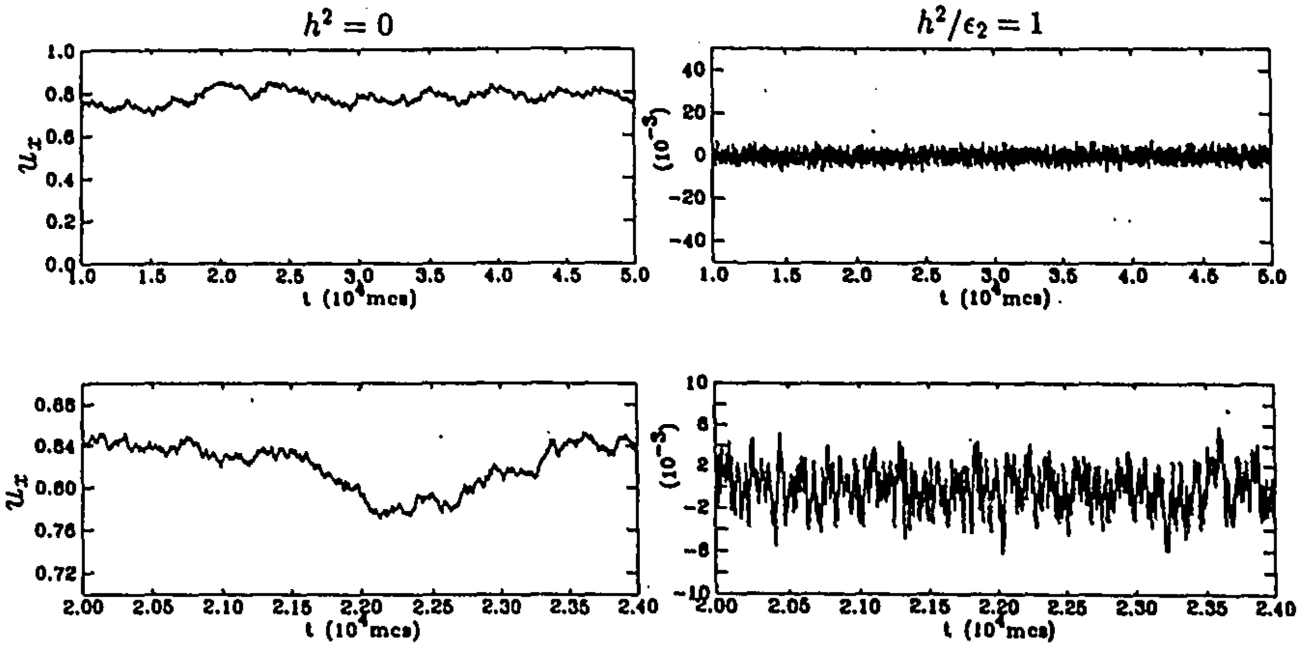

Figure 3.11: Raw data for the director fluctuations given as time series, $u_x(t)$, for one of the Cartesian components of the director **u**. The time, $t$, is given in units of Monte Carlo steps per lattice site (mcs). Results are shown for a temperature $T = 0.85\epsilon_2/k_B$ both in the absence, $h^2 = 0$ (a), and in the presence, $h^2/\epsilon_2 = 1$ (b), of an ordering field. The lower panels show blow-ups of a small part of the corresponding time series in the top panels.

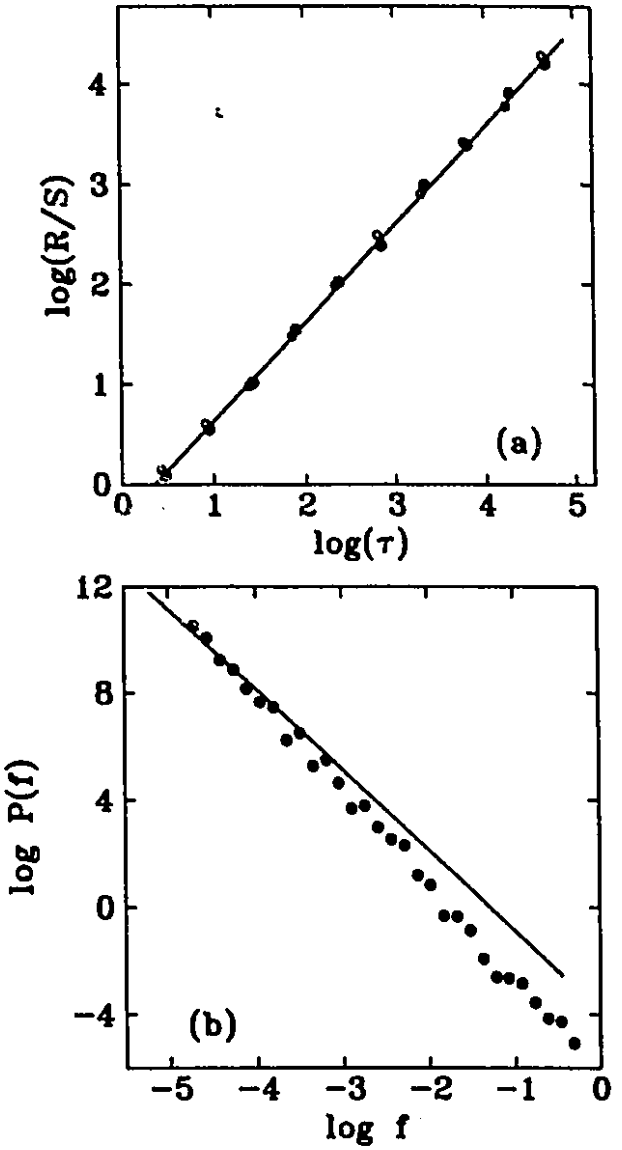

Figure 3.12: (a) Log–log plot of the $R/S$-value vs time range $\tau$ for the nematic director fluctuations at two temperatures in the nematic phase, $T = 0.85\epsilon_2/k_B$ (•) and $T = 1.00\epsilon_2/k_B$ (∘). The best linear fit to the data set is given by the solid line, $R/S \sim \tau^H$, with $H \simeq 1$. (b) Log–log plot of the power spectrum, $P(f)$, for the data at $T = 1.00\epsilon_2/k_B$. The solid line denotes the function $P(f) \sim f^{-\beta}$ with $\beta = 3$.

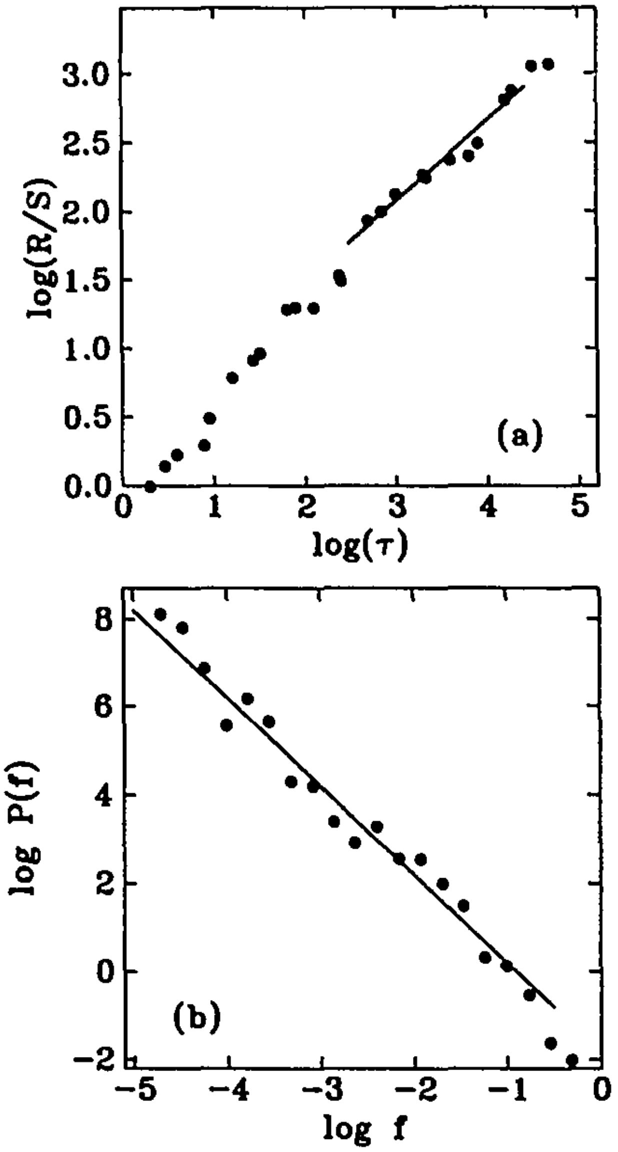

Figure 3.13: (a) Log–log plot of the $R/S$-value vs time range $\tau$ for the nematic director fluctuations at a temperature, $T = 1.30\epsilon_2/k_B$ (•) in the isotropic phase. The best linear fit to the data set over long time ranges is given by the solid line, $R/S \sim \tau^H$, with $H \simeq 0.59$. (b) Log–log plot of the corresponding power spectrum, $P(f)$. The solid line denotes the function $P(f) \sim f^{-\beta}$ with $\beta = 2$.

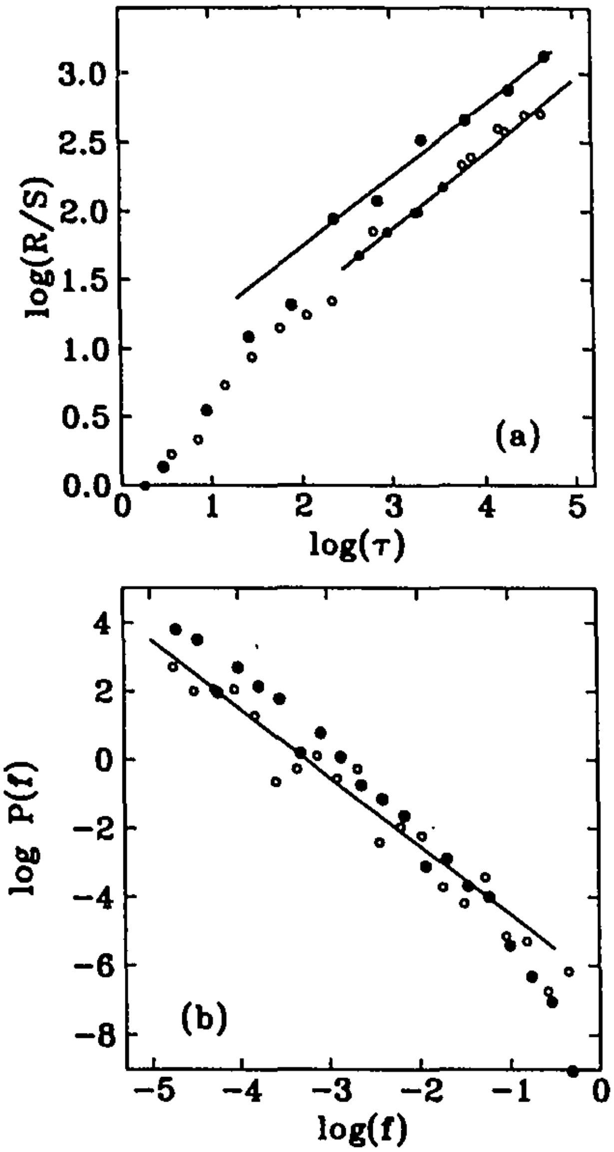

Figure 3.14: (a) Log-log plot of the $R/S$-value vs time range $\tau$ for the nematic director fluctuations in the presence of an ordering field of strength $h^2/\epsilon_2 = 1$. Results are shown for a temperature, $T = 1.00\epsilon_2/k_B$ (•), in the nematic phase and a temperature, $T = 1.30\epsilon_2/k_B$ (o), in the isotropic phase. The best linear fits to the two data sets over long time ranges are given by the solid lines, $R/S \sim \tau^H$, with $H \simeq 0.52$ and 0.55 respectively. (b) Log-log plot of the corresponding power spectra, $P(f)$. The solid line denotes the function $P(f) \sim f^{-\beta}$ with $\beta = 2$.

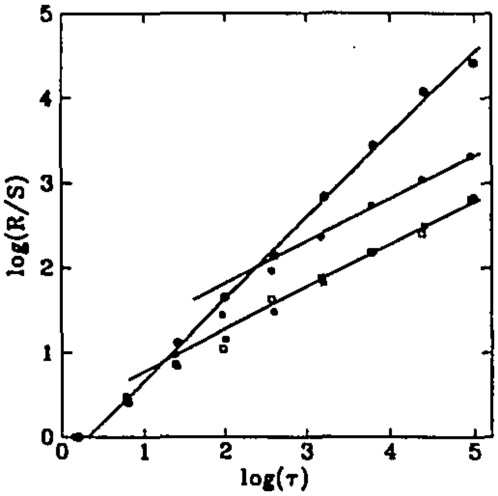

Figure 3.15: Log–log plot of the $R/S$-value vs time range $\tau$ for the nematic director fluctuations at temperature in the nematic phase, $T = 1.00\epsilon_2/k_B$. The data correspond to four different values of the applied field, $h^2 = 0$ (●), 0.05 (○), 0.4 (□) and 1 (■). The best linear fits to the data sets over long time ranges are given by the solid lines, $R/S \sim \tau^H$, with $H \simeq 1$ for zero field and $H \simeq 0.5$ for finite fields.

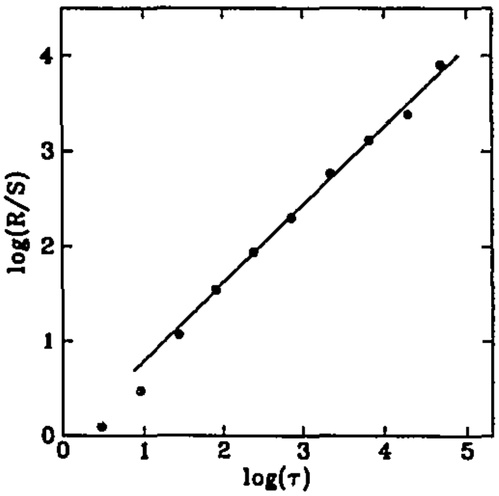

Figure 3.16: Log–log plot of the $R/S$-value vs time range $\tau$ for the nematic director fluctuations at temperature in the nematic phase, $T = 1.00\epsilon_2/k_B$ in the case of a symmetry-breaking wall boundary condition imposed on a system with $L^3 = 28^3$ sites. The solid line denotes $R/S \sim \tau^H$ with $H \simeq 0.82$.

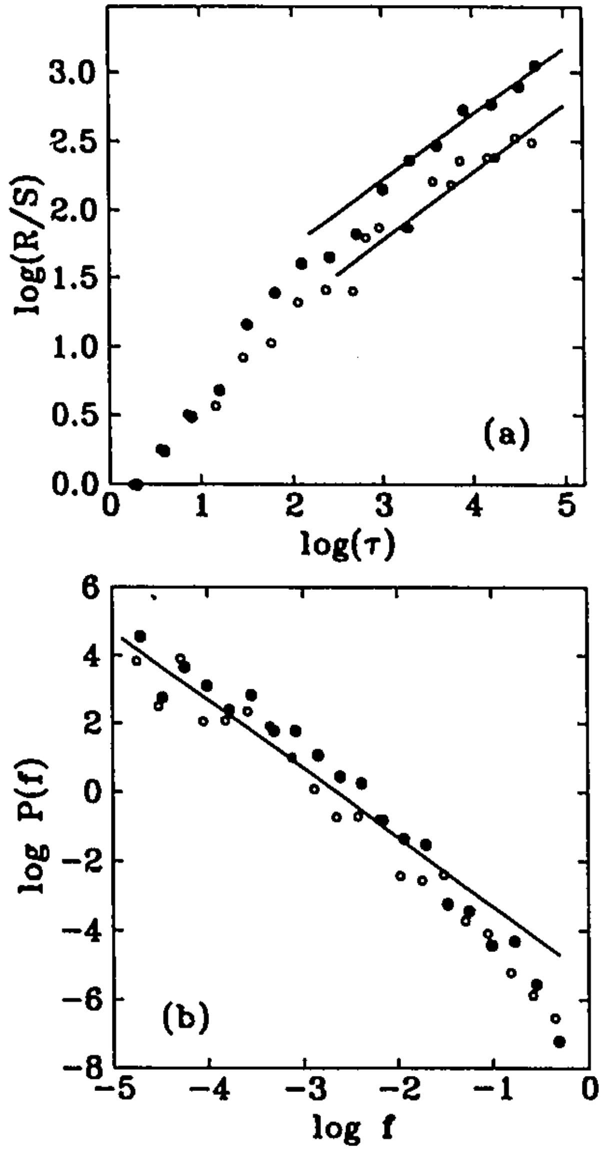

Figure 3.17: (a) Log-log plot of the $R/S$-value vs time range $\tau$ for the nematic order-parameter fluctuations for a temperature, $T = 1.00\epsilon_2/k_B$ (•), in the nematic phase and a temperature, $T = 1.30\epsilon_2/k_B$ (o), in the isotropic phase. The best linear fits to the entire data set over long time ranges are given by the solid lines, $R/S \sim \tau^H$, with $H \simeq 0.48$ and 0.49 respectively. (b) Log-log plot of the corresponding power spectra, $P(f)$. The solid line denotes the function $P(f) \sim f^{-\beta}$ with $\beta = 2$.

# Chapter 4

# Phase Behavior of Pure Lipid Bilayers

## 4.1 Introduction

Lipid molecules are amphiphilic surfactants which self-organize into a variety of phases when mixed with water. These phases are called *lyotropic* liquid crystal phases since they are controlled by both temperature and water concentration. Lipid molecules are, on the basis of their structure, major components of biological membranes, which consist of a lipid bilayer containing proteins and cholesterol usually attached to a cytoskeleton (see Fig. 1.2). The properties of the membrane are to some extent controlled by the lipid bilayer which provides a relatively impermeable fluid barrier to ions and nutrients.

The lipid bilayer in a membrane is composed of different types of lipid molecules. When the lipid components of a membrane are extracted and then redissolved in water at room temperature, the lipid molecules self-organize to form liposomes or multi-bilayer membranes in an 'onion' structure. These can be further treated by sonication to form unilamellar vesicles which are composed of a single bilayer and, if large enough ($\sim 1\mu m$), can be used as membrane models.

In this chapter we are concerned with pure single-component lipid–water systems.

A commonly used lipid is dipalmitoyl phosphatidylcholine (DPPC) which has a zwitterionic (dipolar) polar head and two saturated palmitoyl (C16) chains (Fig. 4.1). Fig. 4.4 shows the phase diagram for DPPC–water systems (Sackmann, 1983). The phases of interest to us are $L_{\beta'}, P_{\beta'}$ and $L_\alpha$. $L_{\beta'}$ is a quasi-2$d$ crystalline (gel) phase in which the lipid chains are tilted. $P_{\beta'}$ is also a quasi-2$d$ crystalline (gel) phase known as the ripple phase in which the bilayer interface supports a long wavelength ripple and $L_\alpha$ is a quasi-2$d$ fluid phase known as the liquid crystalline or fluid phase. An abrupt first-order phase transition occurs between the $P_{\beta'}$ phase and the $L_\alpha$ phase in DPPC. This is known as the main phase transition whose nature is the object of our study via microscopic interaction models. Our description of the main transition involves the extension of the Pink model to include hydrophobic mismatch interactions between the lipid acyl-chain conformational states and direct trans-bilayer interactions between the two monolayers. The bilayer properties in the transition region are analyzed with particular emphasis on the lateral density fluctuations and the related dynamic heterogeneity of the bilayer.

The lipid bilayer can be considered as a lamellar liquid-crystal phase. The bilayer thickness depends on the lipid chain length and lies in the range from 50–100 $\mathring{A}$ with a polar headgroup region of about 5 $\mathring{A}$. The width of the hydration layer is of the order of 10 $\mathring{A}$, depending on the nature of the polar head. To have an idea of how thin the bilayer is, these numbers should be compared to the linear extensions of biological cells which typically lie in the range $10^5$–$10^6 \mathring{A}$.

### 4.1.1 Structure and Properties of Lipid Molecules

Most lipids are amphiphilic molecules which consist of a hydrophilic polar head and at least two hydrophobic hydrocarbon chains. Lipid species differ with respect to the number of carbons and degree of saturation in the chains, as well as nature of the polar head. Hydrocarbon chains which only contains single $\sigma$-bonds between the carbons are called saturated chains. Hydrocarbon chains are quite flexible because isomeric rotations around the $C$–$C$ bond involve much smaller energies ($\sim 1\ kcal/mol$) than

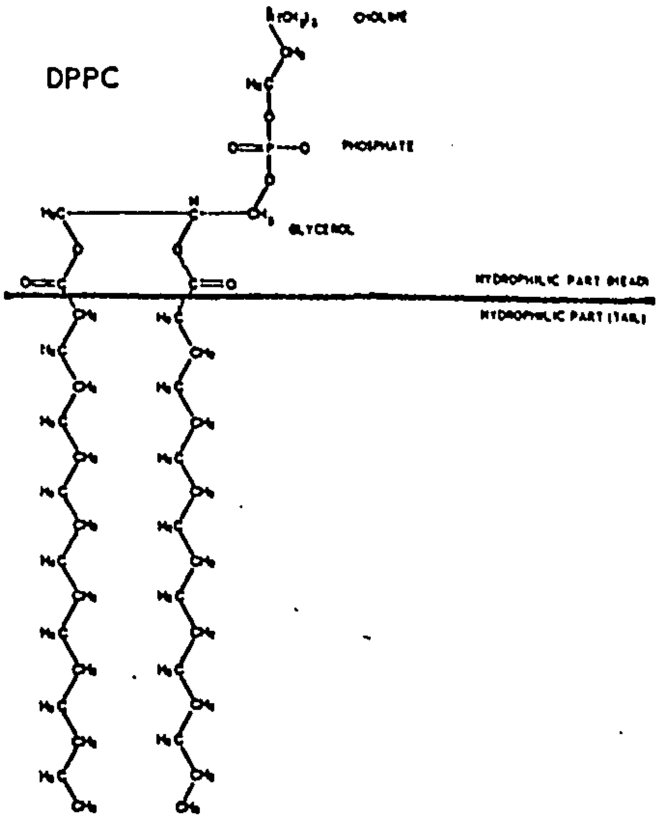

Figure 4.1: Chemical structure of dipalmitoyl phosphatidylcholine (DPPC) [Adapted from Ref. (Mouritsen, 1987)].

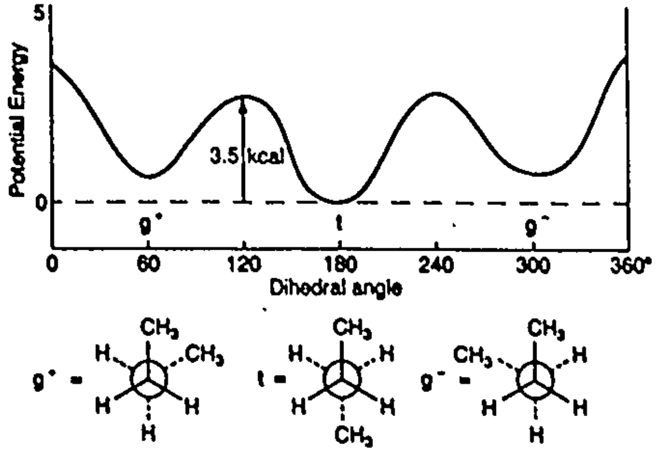

Figure 4.2: Potential energy curve for rotation about a carbon–carbon bond in an alkane. Below is the Newman projection diagram of the minimum energy *gauche* and *trans* conformations of butane:$g^+$,$g^-$, and $t$. [After Ref. (Gennis, 1989)]

the covalent bonds ($\sim$ 90 $kcal/mol$) between the carbon atoms. The potential energy curve for the rotation in an alkane is shown in the Fig. 4.2. The *trans* configuration is most stable and there is an estimated energy barrier of 3.5 kcal/mol for rotation to the *gauche* form. The all-trans configuration allows the chain to be maximally extended, whereas a gauche bond alters the direction of the chain. A gauche–trans–gauche sequence for three consecutive $C$–$C$ bonds results in a kink in the chain which effectively displaces the portions of the chain above and below the kink, as shown in Fig. 4.3. Note that each gauche configuration can be designated $g^+$ or $g^-$ depending on the sense of rotation in going from $C_1$ to $C_4$. A kink which results in a simple displacement can be either $g^+tg^-$ or $g^-tg^+$. The presence of kinks or other deviations from the simple all-trans chain configuration results in increasing the cross-sectional area of the hydrocarbon chain from the minimum of about 20 $\AA^2$.

X-ray diffraction, neutron diffraction and Raman spectroscopy (Hauser *et al.*, 1981; Seelig and Seelig, 1980) indicate that in the gel phase, the hydrocarbon chains of saturated diacyl phospholipids are predominantly in the all-trans configuration. In the liquid crystalline phase, the introduction of gauche configurations increases the effective chain cross section considerably.

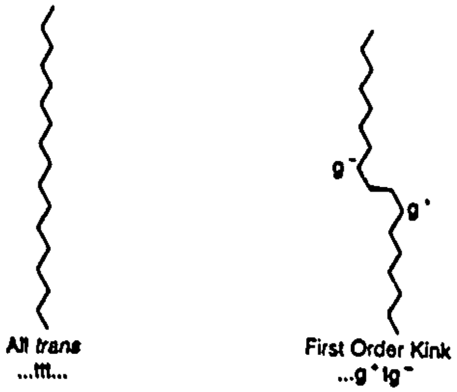

Figure 4.3: Illustration of two alkyl chain configurations [Adapted from Ref. (Gennis, 1989)].

### 4.1.2 Lipid–Water Mixtures

Lipids display remarkable physical properties when they are mixed with water. The nonpolar hydrocarbon portions of lipid molecules are aggregated and the polar headgroups are in contact with water. The major thermodynamic driving force stabilizing the self-organization of hydrated lipid aggregates is the hydrophobic effect. This effect is entropic in origin and is caused by the unfavorable constraints placed on water in direct contact with nonpolar hydrocarbons.

The structure and dynamics of pure water are complex and are dominated by intermolecular hydrogen bonds. When a nonpolar hydrocarbon is dissolved in water, it causes an unfavorable organization of the water around the hydrocarbon by reducing the number of hydrogen bonds. The water molecules orient themselves in such a way as to maintain intermolecular hydrogen bonds, but since those water molecules in direct contact with the nonpolar solute molecule have fewer water molecules as neighbors, there are substantial configurational constraints on the system. Hence, there is a decrease in the entropy of the system. As a result, the net free energy change upon transferring a nonpolar solute from a nonpolar solvent to water is unfavorable due to this entropic effect on the water solvent.

Some of the important phases found for lipid–water systems (as summarised

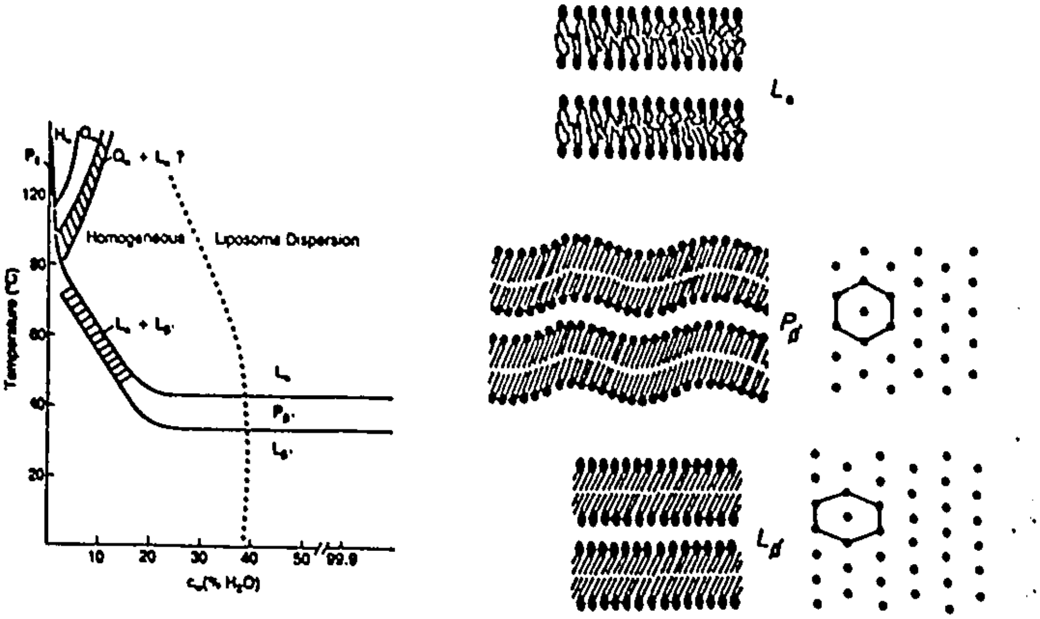

Figure 4.4: Phase diagram for the DPPC–water mixture [Adapted from Ref. (Gennis, 1989)].

above) are:

1. The lamellar liquid crystalline phase ($L_\alpha$): this phase is present for the majority of lipid species in biological membranes. There is considerable disorder in the acyl chains as indicated by the X-ray diffraction data and the lipid molecules can diffuse laterally.

2. Lamellar gel phases ($L_\beta, L_{\beta'}$): these are low temperature phases for lipids which form the lamellar structure. The molecules are tightly packed in a lattice structure and the acyl chains are highly ordered, corresponding mostly to the all-trans configuration. Because the chains are maximally extended in the gel phase, the bilayer thickness is greater than in the liquid crystalline phase. The density of the gel phase is slightly greater than that of the liquid crystalline phase. $L_\beta$ is an untilted phase whereas $L_{\beta'}$ denotes that the chains are tilted with respect to the bilayer normal. There is no lateral diffusion in this phase, but the molecules can librate.

3. The ripple phase $P_{\beta'}$: in this phase, the surface of the bilayer is rippled and presents a wave-like appearance in electron micrographs. The thermotropic phase transition $P_{\beta'} \rightarrow L_\alpha$ is known as the main transition, whereas the transition $L_{\beta'} \rightarrow P_{\beta'}$ is called the pretransition. When the ripple phase is not present, the main phase transition can be from $L_\beta \rightarrow L_\alpha$.
4. Hexagonal I phase ($H_I$): in this phase, the lipids are organized into cylinders with the polar groups on the outside, in contact with water. The cylinders are packed in a $2d$ hexagonal pattern. This and the next phase are non-bilayer phases.
5. Hexagonal II phase ($H_{II}$): the lipids are into cylinders, but in this case the polar groups face the inside, where there is a column of water. The cylinders are again packed in a $2d$ hexagonal array.

### 4.1.3 Summary of Experimental Observations for the Main Phase Transition of Lipid Bilayers

A selection of experimental results on the thermal behavior of fully hydrated lipid bilayers is presented in Fig. 4.5 for DPPC and DMPC. All experiments indicate that the bilayers display striking thermal anomalies. For example, Fig. 4.5(a) shows that the specific heat exhibits a pronounced peak. At the peak temperature, a discontinuous change in the multi-lamellar repeat distance and therefore bilayer thickness occurs as shown in Fig. 4.5(c). The change in bilayer thickness is accompanied by an equally dramatic change in bilayer area as shown in Fig. 4.5(d) for DMPC. Fig. 4.5(b) presents the results for the first two moments of the distribution of quadrupolar splittings in the nuclear magnetic resonance (NMR) spectrum of perdeuterated DPPC. Again there is a dramatic decrease in the moments over a narrow temperature interval. This temperature interval is lower than the equivalent temperature in Figs. 4.5(a) and (c) due to deuteration of the chains. The moments are direct measures of the average segmental order along the deuterated hydrocarbon chain, *i.e.* Eq. (4.3). To a

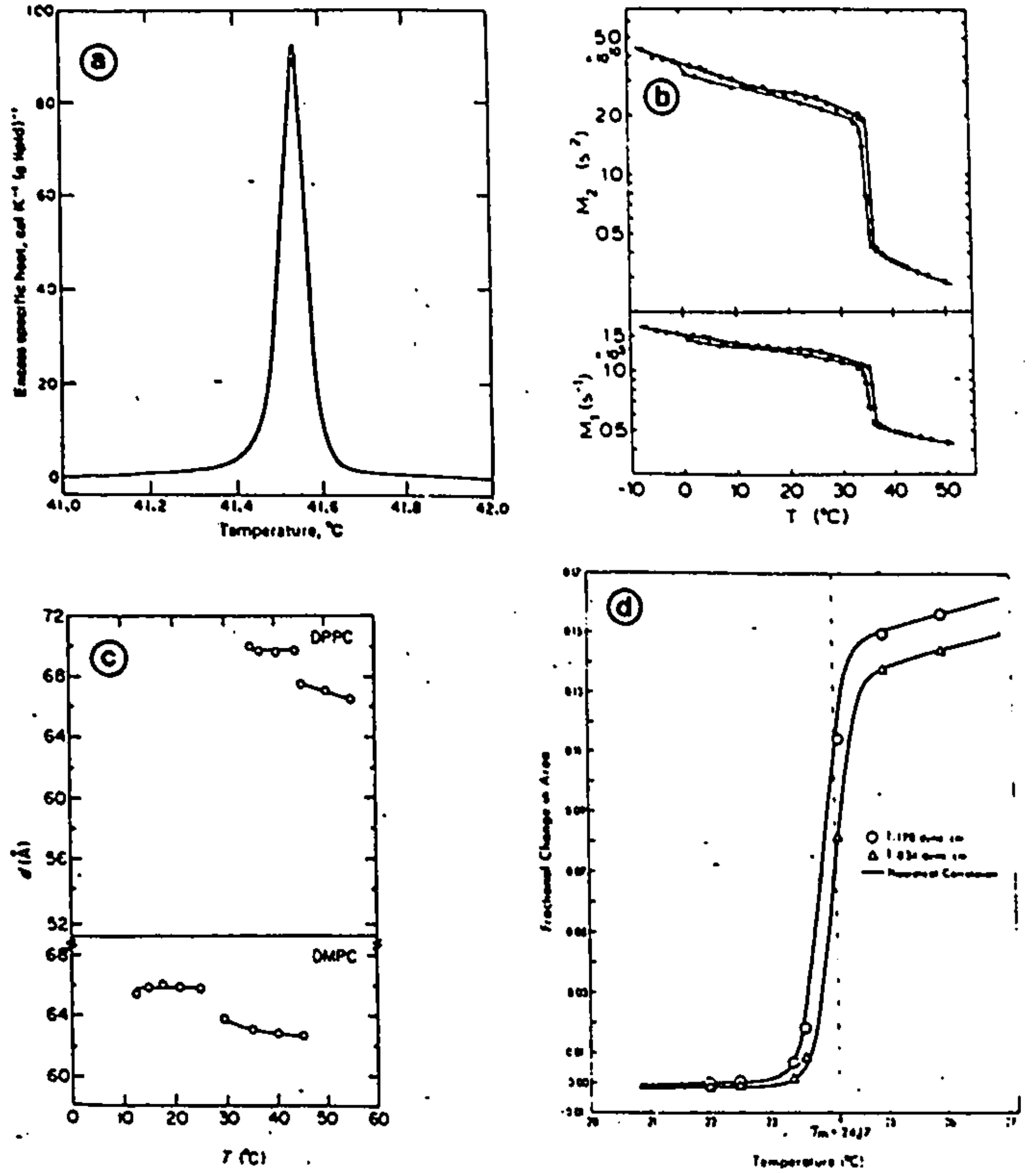

Figure 4.5: Thermal behavior of one-component lipid bilayers of DPPC (C16) and DMPC (C14). (a) Specific heat for DPPC determined by differential scanning calorimetry; (b) First and second moment of the quadrupolar magnetic resonance spectrum of $d_{62}$-DPPC; (c) Lamellar repeat distance determined by low-angle X-ray scattering on DMPC and DPPC; and (d) Cross-sectional area change for DMPC determined by micromechanics measurements.

good approximation, $M_1$ is proportional to the hydrophobic thickness of the bilayer (Seelig and Seelig, 1980; Shinitzky and Yuli, 1982).

The sharp thermal anomalies are distinct signals of a phase transition in the bilayer. This transition, commonly referred to as the main transition, or the gel–fluid transition, takes the bilayer from a low-temperature $2d$ solid (gel) to a high-temperature fluid (liquid crystalline) phase. The main gel–fluid lipid bilayer phase transition has the following characteristics: (i) a sharp endothermal first-order transition at a temperature $T_m$; (ii) a large area expansion, typically $\Delta A(T_m) \simeq 20\%$, (iii) a small volume change, $\Delta V(T_m) \leq 5\%$, and (iv) a large transition entropy, $\Delta S(T_m) \sim 15 k_B$/molecule.

## 4.2 The Pink Model

In this section we present the microscopic phenomenological model used in this section to describe the main phase transition.

### 4.2.1 Microscopic Models of the Main Transition

There are several types of theoretical models and accompanying methods which have been used to analyze the properties of lipid system (including lipid bilayers). These fall into the following categories:

1. Packing models;
2. Full simulation of the bilayer using molecular dynamics;
3. Continuous $2d$-models;
4. $2d$-microscopic phenomenological models.

There are both lattice and off-lattice models in the last category. The exclusive volume is automatically included in the lattice models. Furthermore the translation degrees of freedom are neglected since the high value of the specific heat at the main transition temperature and the fact that it increases with chain length implies that main phase transition is entropic. Also, as Doniach (Doniach, 1978) pointed out, the transition is triggered by changes in chain-conformations and the related change in entropy is much greater than the latent heat due to crystal melting. The model lattice therefore fixes the number of nearest neighbors and assigns pre-selected single chain conformational states to each lattice point. Since these states have different cross-sectional areas, the total area of the system changes with temperature. $2d$ lattice models include the two-state model of Doniach, the multi-state Pink model and its extension by Tevlin *et al.* (Tevlin *et al.*, 1986) and the Pink–Potts model of Mouritsen and Zuckermann (Mouritsen and Zuckermann, 1987; Zuckermann and Mouritsen, 1987) which makes an attempt to include translation degrees of freedom. Off-lattice models include the 7-state model of Scott and the off-lattice version of the Doniach model (Fraser *et al.*, 1991). The problem with lattice models is that they do not include sterically induced correlations between chain conformation. However they are very useful for the understanding of phase transitions close to or at a critical point, as is likely to be the case for the main phase transition (Doniach, 1978). In this chapter we use the term *chain-melting* to refer to the dominant effect of the change in chain conformations on the main phase transition, which is entropic in nature.

### 4.2.2 The Pink Model

The Pink model, which is an extension of the 2-state Doniach model, is a multi-state lattice model in which each acyl chain is positioned on a regular (*e.g.* hexagonal) two-dimensional lattice. It is also assumed that the conformational properties of a single acyl chain can be described by a small number of selected conformational states corresponding to the mapping of the three-dimensional acyl-chain conformations upon a finite, discrete set of projected two-dimensional coarse-grained variables. The number of states included in a multi-state model depends on the level of detail required.

Pink *et al.* (Pink, Green and Chapman, 1980; Pink, 1983) used the model to calculate the temperature dependence of the intensity of the $1130cm^{-1}$ Raman band, which is a hydrocarbon chain $C$–$C$ skeletal stretch mode (Snyder, 1970), by extrapolating the calculations of Snyder (Snyder, 1967; Snyder, 1970). In constructing a model of chain melting they assumed that the lipid chain conformational states were given by the rotational isomeric model (Flory, 1975; Flory, 1969), and found that nine low-energy hydrocarbon chain states with cross-sectional area $\leq 25\mathring{A}^2$, ranging from the all-*trans* state to states with three *gauche* bonds, contributed significantly to the Raman intensity of the $1130 cm^{-1}$ band. The limit on the area per chain was then imposed to account for hard-core steric hindrance in the gel phase, where only conformations with small cross-sectional area could be thermally excited. These nine states, plus a high-energy melted state (see below) formed the basis of the Pink model. The mean-field results for the Raman intensities were found to be in good agreement with the measured intensities (Pink, Green and Chapman, 1980).

In the Pink lattice model the conformational chain variables are coupled by hydrophobic anisotropic van de Waals interactions by analogy with anisotropic liquid crystals. The lattice approximation automatically takes care of the excluded volume interactions. The interaction between the hydrophilic moieties can be modeled by a Coulomb force or an effective intrinsic lateral pressure (Caillé *et al.*, 1980). It is assumed that each site of a hexagonal lattice is occupied by one of the hydrocarbon chains of the phospholipid molecule with $M$ carbon nuclei. The selected conformational states of the chain can be described as follows:

1. The all-trans ground state which is non-degenerate and has internal energy $E_1 = 0$ and area $A_1 = 20.4\mathring{A}^2$.

2. Eight intermediate states of energy, $E_n$, area, $A_n$, and degeneracy, $D_n$ ($n = 2,\ldots,9$). Here $D_n$ is proportional to $M$ and $A_n \leq 26\mathring{A}^2$. The energies, $E_n$, are less than or equal to $3E_g$ where $E_g$ is the energy required to form a gauche bond. The corresponding chains are at most three units shorter than the all-trans state.

3. One high-energy 'melted' state which is taken to have an area $A_{10}$, an energy

$E_{10}$, and a degeneracy $D_{10} \propto 3^M$. This state represents the average over all the conformations which occur in the fluid phase.

Experimental observations for the bilayer volume change (Sec. 4.1.3) suggest that the hydrophobic membrane volume is almost constant (Marčelja, 1974; Träuble and Haynes, 1971) and therefore the areas of all 10 states are related to their hydrophobic length $d_n$ by

$$A_n = A_1 \frac{d_1}{d_n}. \tag{4.1}$$

The inter-chain interactions are taken to be van de Waals interactions. The van de Waals dispersion forces are induced by quantum zero-point fluctuations of electronic systems. The attractive interactions, $W(r)$, between long parallel saturated chains at short distance varies as $r^{-5}$ (Salem, 1962). The van de Waals interaction between neighboring chains in states $m$ and $n$ is approximated as (Wulf, 1977; Mouritsen, 1990)

$$V_{mn}(r) = S_m S_n W(r). \tag{4.2}$$

Here $S_n$ is the orientational order parameter of the $n$-th chain conformation and is written by:

$$S_n = \frac{1}{2(M-1)} \sum_{q=1}^{M-1} (3\cos^2(\theta_{nq}) - 1) \tag{4.3}$$

where $\theta_{nq}$ is the angle between the normal spanned by the $q$th $C$-$H_2$ group and the long axis of the chain. The order parameter can be measured by $^2H$-NMR since deuterium can be chemically substituted for hydrogen at specific places in the lipid molecule. This substitution is generally considered nonperturbing. As an approximation, the $C$–$C$–$C$ bond is assumed to have an angle 120°. Then the geometrical constraints give a simple relation between $S_n$ and $d_n$ (Seelig and Seelig, 1980):

$$S_n = 1.8\frac{d_n}{d_1} - 0.8. \tag{4.4}$$

The distance between the two neighboring chains at state $m$ and $n$ is $R_{mn} = R_m + R_n$ in a close-packed configuration. Using (Caillé *et al.*, 1980)

$$W(R_{mn}) \propto R_{mn}{}^{-5} \propto R_m{}^{-5/2} R_n{}^{-5/2}, \tag{4.5}$$

the van de Waals interaction between the chains, the Eq. (4.2), can be written as

$$V_{mn} = -J_0 I_m I_n \tag{4.6}$$

where $J_0$ is a coupling constant and $I_n = \omega_n S_n (A_n/A_1)^{-\frac{5}{4}}$, since the radius $R_n$ of a cylindrical chain is related to its cross-section, $A_n$, by $R_n = \sqrt{A_n/\pi}$. The factor, $\omega_n$, is only different from unity for the highly excited state for which the approximation of the acyl chain as a long rod is poor.

The interactions between the polar headgroups are not taken into account in a detailed manner, because they are expected to play a minor role in the main phase transition in comparison to the chain behavior. The entropy change in the transition comes primarily from the increase in internal entropy in going from the ordered gel state ($n = 1$) to the highly excited fluid state ($n = 10$). The interactions are approximated by an effective lateral pressure, $\Pi$, which couples to the cross sectional area, $A_n$, in the term of $\Pi A_n$. The interaction between the headgroups such as hydrogen bonding will be discussed later in Chap. 6.

The Hamiltonian of the Pink model can be written as follows:

$$\mathcal{H}_0 = \sum_i \sum_{\alpha=1}^{10} (E_\alpha + \Pi A_\alpha) \mathcal{L}_{\alpha,i} - \frac{J_0}{2} \sum_{\langle i,j \rangle} \sum_{\alpha,\beta=1}^{10} I_\alpha I_\beta \mathcal{L}_{\alpha,i} \mathcal{L}_{\beta,j} \tag{4.7}$$

where $\langle i,j \rangle$ are nearest-neighbor indices. $\mathcal{L}_{\alpha,i}$ is an occupation variable, which is unity when the $i$th chain is in the $\alpha$th conformational state and zero otherwise. The model was first examined in the mean-field approximation and the model parameters used were determined by fitting to thermodynamic data for saturated phosphatidylcholine (PC) bilayers of different acyl-chain length. For example, the values of the parameters $J_0$ and $\Pi$ found for dipalmitoyl phosphatidylcholine (DPPC) are $J_0 \approx 0.71 \times 10^{-13}$ erg and $\Pi = 30$ dyn/cm by fitting to experimental values for the transition temperatures $T_m$ and transition enthalpies $\Delta H$ of DPPC. The mean-field calculations predicted first-order phase transitions for all chain lengths ($M$ = 12–22) examined with the phase transitions becoming sharper as chain length increases. Monte Carlo simulation work of Mouritsen and co-workers (Mouritsen, 1990) indicated that the transition predicted by Pink model with the fitted parameters is at best a weak first-order phase transition close to a critical point. Furthermore, these results showed that the model exhibits dynamic heterogeneity in the transition region, which could be interpreted in terms of thermal fluctuations in the form of clusters of the minority phase in the majority phase. Ipsen *et al.* (Ipsen, Jørgensen and Mouritsen, 1990) suggested that the fluctuations could be characterized by a finite length and that they behaved in a pseudocritical manner in the transition region. It is however rather difficult, using conventional methods of analyzing the transition, to assess whether the transition is continuous or of first order, or whether there is a transition at all. Corvera *et al.* (Corvera, Laradji and Zuckermann, 1993), using the method of Lee and Kosterlitz, found no phase transition in the Pink model for the fitted parameters. They showed that the system was close to a critical point and that the dynamic heterogeneity predicted by the Pink model is related to long-lived short-range order effects. In fact, the finite-size behavior of the peak in the specific heat remained constant with varying system size up to lattices of size 300 × 300 (Ipsen, 1991). It does not scale as expected for a first-order phase transition. In contrast to the most of experimental results, the maximum of the specific heat calculated in the Pink model is also very small.

## 4.3 Extensions of the Pink Model

As seen in the previous section, the Pink model with the fitted parameters for saturated PC bilayers does not give a phase transition, but rather describes a fluctuating lipid monolayer beyond a critical point. In this section we propose two models based on the Pink model, but with additional interactions appropriate for lipid bilayers.

### 4.3.1 Pink Model with Mismatch Interactions

The form of the interactions used in the Pink model applies to a single monolayer, such as a lipid monolayer spread on an air–water interface. The question therefore arises: what type of interactions present in bilayers and not in monolayers leads to a first-order phase transition? One type of interaction is due to the mismatch between lipids in different conformational states, which is analogous to the mismatch interaction between lipids and proteins in the 'mattress model' proposed by Mouritsen and Bloom (Mouritsen and Bloom, 1984). In the mattress model this interaction was assigned to the mismatch between neighboring lipids and proteins with unequal interfacial lengths of hydrophobic contact. This effect was represented by a repulsive interaction between the aqueous medium and the superfluous hydrophobic length. The same interaction should occur between neighboring lipids in different rotameric conformational states having unequal hydrophobic contact lengths and it should only occur in bilayers, since, for monolayers, the superfluous hydrophobic length can make contact with air (or oil) at negligible energy cost (Zhang *et al.*, 1992a).

An additional term in the Hamiltonian describing the mismatch interaction among different conformational states of the acyl chains can be written as follows by analogy with the case of lipid–protein interactions (Zhang *et al.*, 1992a):

$$\mathcal{H}_{\mathrm{m}} = \frac{\gamma_{\mathrm{mis}}}{2} \sum_{(i,j)} \sum_{\alpha,\beta} |d_\alpha - d_\beta| \mathcal{L}_{\alpha,i} \mathcal{L}_{\beta,j}, \tag{4.8}$$

where $d_\alpha$ is the hydrocarbon chain length for the $\alpha$th conformational state, and $\gamma_{\mathrm{mis}}$ is the parameter related to the hydrophobic effect. The approximation made here is that two monolayers of a phospholipid bilayer are identical and do not interact directly with one another. The two monolayers only interact with each other indirectly via the mismatch interaction. The total Hamiltonian of the extended model is therefore

$$\mathcal{H} = \mathcal{H}_0 + \mathcal{H}_{\mathrm{m}} \tag{4.9}$$

### 4.3.2 Inter-Monolayer Coupling Model

Another type of interaction presents in bilayers but not in monolayers is the direct coupling between the two monolayers in a bilayer. The effect of the inter-monolayer was first studied theoretically in a two-state lattice model proposed by Georgallas *et* *al.* (Georgallas *et al.*, 1984). They showed by both analytical and simulation methods that even a weak inter-monolayer interaction is sufficient to change the critical point dramatically.

In a more realistic description of bilayers, the monolayers are no longer identical so the monolayers should be described separately. The Hamiltonian for two non-interacting monolayers, according to Eq. (4.7), is

$$\mathcal{H}_0 = \sum_{n=1}^{2}\{\sum_{i}\sum_{\alpha=1}^{10}(E_\alpha + \Pi A_\alpha)\mathcal{L}^n_{\alpha,i} - \frac{J_0}{2}\sum_{\langle i,j\rangle}\sum_{\alpha,\beta=1}^{10} I_\alpha I_\beta \mathcal{L}^n_{\alpha,i}\mathcal{L}^n_{\beta,j}\}. \tag{4.10}$$

$\mathcal{L}^n_{\alpha,i}$ is the occupation variable which is unity when the $i$th chain of the $n$th monolayer is in the $\alpha$th conformational state and zero otherwise. The mismatch interaction of Eq. (4.8) between different conformational states of the acyl chains across the bilayer should be re-written as

$$\mathcal{H}_m = \frac{\gamma_{mis}}{2}\sum_{\langle i,j\rangle}\sum_{\alpha 1,\beta 1}\sum_{\alpha 2,\beta 2}|d_{\alpha 1} + d_{\beta 1} - d_{\alpha 2} - d_{\beta 2}|\mathcal{L}^1_{\alpha 1,i}\mathcal{L}^2_{\beta 1,i}\mathcal{L}^1_{\alpha 2,j}\mathcal{L}^2_{\beta 2,j}. \tag{4.11}$$

Finally, we consider a Hamiltonian, $\mathcal{H}_i$, which represents a direct contribution from the interlayer coupling. We assume that every acyl chain interacts with its nearest neighbors in the opposite monolayer in a pair-wise manner with an energy $-J_2\Omega_\alpha\Omega_\beta$ where $\Omega_\alpha$ are state-dependent parameters. In the fluid phase the acyl chains are disordered and the lateral diffusion coefficient is at least two orders of magnitude greater than in the gel phase. This implies that the interlayer coupling between the chains in the all-trans state is much greater than that in the highly excited fluid state. We therefore take $\Omega_1 = 1$ and $\Omega_{10} = 0$. For the intermediate states we choose $\Omega_{2,3,4} = \frac{2}{3}$, $\Omega_{5,6,7} = \frac{1}{3}$, and $\Omega_{8,9} = \frac{1}{9}$. $\mathcal{H}_i$ can be written as follows

$$\mathcal{H}_i = -J_2\sum_{i}\sum_{\alpha,\beta}\Omega_\alpha\Omega_\beta\mathcal{L}^1_{\alpha,i}\mathcal{L}^2_{\beta,i}. \tag{4.12}$$

The total Hamiltonian of the extended model (Zhang, Mouritsen and Zuckermann, 1992a) described in this section is therefore

$$\mathcal{H} = \mathcal{H}_0 + \mathcal{H}_m + \mathcal{H}_i. \tag{4.13}$$

Models describing the complete bilayer as a system of interacting monolayers are useful since they can be extended to include and distinguish between peripheral and integral membrane-bound proteins. Furthermore, they enable us to model monomer–dimer dissociations for certain integral proteins such as gramicidin A (Sec. 5.3).

## 4.4 Phase Behavior in the Extended Pink Models

We examine the extended Pink models described in Sec. 4.3 by performing numerical simulations described in Chap. 2 on $L \times L$ triangular lattices with periodic boundary conditions. Very long simulations are performed at the transition temperature in order to obtain good statistics. The temperature at which the simulations are performed were chosen as close as possible to the transition temperature $T_m(L)$, and it was found that $2 \times 10^6$ Monte Carlo steps per site (MCS) are sufficient to obtain the required accuracy (Zhang *et al.*, 1992a; Zhang, Mouritsen and Zuckermann, 1992a).

### 4.4.1 Nature of the Phase Transition (I) – Effect of the Mismatch Interaction

It is clear, from the Eq.( 4.8), that the mismatch interactions affect the bilayer mainly in the region where there are strong fluctuations in the hydrocarbon chain length. The extended model is therefore mainly different from the original Pink model in transition region. The effect of the mismatch interaction is to suppress the fluctuations and drive the transition away from criticality into a region of well-defined first-order transitions. The effect of suppressing the fluctuations around the transition region is illustrated in Fig. 4.6 in the case of the specific heat. The specific heat in the thermodynamic limit for temperatures outside the transition region decreases as the value of $\gamma_{mis}$ is increased. At the transition Fig. 4.7 shows the emergence of the first-order phase transition with increasing $\gamma_{mis}$ via the appearance of the maximum in $\Delta\mathcal{F}(L)$.

The finite size scaling methods described in Chap. 2 are applied to determine the nature of the phase transition in the model described in Sec. 4.3.1. The temperature at which a finite system undergoes a first-order phase transition usually depends on the size of the system. It also depends on which quantity is used to identify the finite-size transition point. In the case of the free energy, the transition temperature $T_m^{\mathcal{F}}$ is defined by requiring $\mathcal{F}(A_1, L) = \mathcal{F}(A_2, L)$, where $\mathcal{F}(A_1, L)$ and $\mathcal{F}(A_2, L)$ are the free energies of the gel and fluid phases respectively. The free energy functions are calculated for several values of the mismatch parameter $\gamma_{mis}$, in order to examine the phase behavior of the system and to locate the critical point. The data for three different cases are presented in Fig. 4.8, which show that free energy as function of area per lipid molecule exhibits two minima with a barrier in between. We find that the system does not exhibit a phase transition for values of $\gamma_{mis}$ below $4 \times 10^{-16} erg/\AA$ (Fig. 4.8a). At this value of $\gamma_{mis}$, the system is either at or extremely close to the critical point (Fig. 4.8b). Above this value of $\gamma_{mis}$ the transition is of first order (Fig. 4.8c). The height of the barrier, $\Delta\mathcal{F}(L)$, changes considerably with system size for different values of $\gamma_{mis}$. This can be seen in Fig. 4.9, where $\Delta\mathcal{F}(L)$ is shown as a function of system size for the three values of $\gamma_{mis}$ corresponding to Fig. 4.8. Fig. 4.9 shows that $\Delta\mathcal{F}(L)$ decreases with increasing $L$ for $\gamma_{mis} = 3 \times 10^{-16} erg/\AA$ (implying the absence of a transition) and increases with increasing $L$ for $\gamma_{mis} = 5 \times 10^{-16} erg/\AA$ (implying the occurrence of a first-order phase transition). For $\gamma_{mis} = 4 \times 10^{-16} erg/\AA$, the height of the barrier does not depend on system size to within numerical error, indicating that the transition for this parameter value is very close to a continuous transition.

The temperature dependence of the specific heat and the susceptibility obtained by using the method of Ferrenberg and Swendsen are shown in Figs. 4.10 and 4.11 respectively for $\gamma_{mis} = 5 \times 10^{-16} erg/\AA$ and for several system sizes. As the system size increases, the peak height of both response functions increases while the width of the peaks decreases. The peak heights of both quantities are plotted as functions of $L^d$ in Figs. 4.12 and 4.13 and a linear behavior is observed in agreement with Eq. (2.17). The temperature $T_m^C$ at which the specific heat exhibits a maximum is, for large-enough system sizes, identical to the corresponding temperature for the susceptibility maximum. The full finite-size scaling behavior is investigated for the case of the specific heat. The results are given in Fig. 4.14 and they exhibit the expected scaling behavior for a first-order phase transition. Results for the fourth-order cumulant are given in Fig. 4.15 for $\gamma_{mis} = 5 \times 10^{-16} erg/\AA$. As $L$ increases, the minimum of the cumulant goes to a value different from 2/3 at a certain temperature $T_m^{\sigma}(L)$, and to 2/3 at other temperatures, as expected. The nontrivial limit is obtained by extrapolating the data for the larger sizes, as shown in Fig. 4.16.

There are different values of the transition temperature depending on the size of system and the physical quantity used to define the transition (Sec. 3.3.4). However they tend to the same temperature in the thermodynamic limit, *i.e.*, as $L \rightarrow \infty$. This is demonstrated in Fig. 4.17, which shows that for $\gamma_{mis} = 5 \times 10^{-16} erg/\AA$ the transition temperature $T_m = 313.7K$ in the thermodynamic limit. This is a good agreement with the experimental observations (Albon and Sturtevant, 1978; Biltonen, 1990).

The absolute value of the mismatch interaction required to induce a first-order phase transition is small compared to the strength of van der Waals interactions between lipid chains. This is due to the closeness of the critical point. The ratio of the maximum value of the mismatch interaction used in this model to the coupling constant of the van der Waals interaction is only of the order of 5%.

The latent heat of the first-order transition can be obtained from an integration over a narrow temperature range around the transition. Indeed according to the universal curve of the specific heat (Fig. 4.14), the integral $\int c(T)dT$, the area under the curve of the specific heat is independent of the size of system, $L$. Therefore, the quantity is a measure of the latent heat in the thermodynamic limit. The latent heat obtained by this way is about 8.12 $kcal/mol$, which is almost same as that found by calculating the difference in free energy between the minima at the first order transition (Zhang *et al.*, 1992a).

### 4.4.2 Nature of the Phase Transition (II) – Effect of Inter-Monolayer Coupling

Although there is no direct measurement of the interlayer coupling, previous studies suggested that it should be very weak in comparison with the van der Waals interactions between the chains in the same monolayer. In order to investigate the effects of both the mismatch and the interlayer interactions, we choose their respective strengths in such a way that the bilayer would not have a phase transition in the thermodynamic limit in the absence of interlayer coupling but would be extremely close to a critical end-point. A value of $J_2 = 0.04 J_0$ in Eq. (4.12) is chosen in accordance with the earlier work on inter-monolayer coupling (Georgallas *et al.*, 1984). We find that the system does not exhibit a phase transition for values of $\gamma_{mis}$ below $3 \times 10^{-16} erg/\mathring{A}$ and exhibits a weak first-order phase transition at $\gamma_{mis} = 4 \times 10^{-16} erg/\mathring{A}$ (Zhang, Mouritsen and Zuckermann, 1992a).

The results for the model described in Sec. 4.3.2 are similar to those shown in the previous subsection, because they are typical of a first-order phase transition. However Fig. 4.18 shows that there is a finite-size effect in the free energies for the smaller lattice sizes, *i.e.* an additional well is present because the monolayers are in different phases, one being in a gel phase and the other in a fluid phase. Hence in this case, the weak coupling between the finite-size monolayers is overcome by strong lateral fluctuations within the monolayers. Fig. 4.18 also shows that the additional well disappears as the size of system increases, since the interlayer coupling then ensures that the entire bilayer is in either the gel phase or in the fluid phase at any given temperature. It can be seen from the figure that the two phases are separated by an energy barrier whose height increases with increasing $L$. This indicates that the system undergoes a first-order phase transition in the thermodynamic limit.

## 4.5 Cooperativity in the Main Phase Transition

In this section, we examine the physical properties of the bilayers in the neighborhood of a first-order phase transition, such as the lateral heterogeneity, and compare the results with those obtained for a single monolayer of Pink model which has no phase transition in the thermodynamic limit but is close to a critical point (Zhang, Mouritsen and Zuckermann, 1992a; Mouritsen, 1990). To avoid hysteresis effects encountered in standard Monte Carlo calculations, the extrapolation method of Ferrenberg and Swendsen is used to analyze bilayer heterogeneity (Zhang, Mouritsen and Zuckermann, 1992a).

The clusters can be described by a size-distribution function $n_\ell^p(T)$ which gives the number of clusters of type $p$ with $\ell$ lipid chains (Mouritsen, 1990). Here $p$ refers to the fluid chain state if $T < T_m$ or the gel and intermediate chain states if $T > T_m$. The clusters are defined via a nearest-neighbor connectivity criterion dictated by the interaction range. The average cluster size is then

$$\xi(T) = \sum_\ell \ell n_\ell^p(T) / \sum_\ell n_\ell^p(T) \tag{4.14}$$

where the summation is restricted by a lower cut-off in the value of $\ell$ (corresponding three acyl chains in our case) in order to exclude local fluctuations controlled by the Glauber dynamics. Fig. 4.19 shows that average linear dimension $\xi$ of the fluctuating clusters of the minority phase as a function of temperature for both in the presence and absence of the mismatch and the inter-layer interactions. It is seen that $\xi$ is considerably reduced at any given temperature in the presence of the additional interactions, implying that the transition region has narrowed considerably and that the wings of the transition are confined to a much narrower temperature range. This is understandable because of the high energy barrier for the formation of cluster interfaces in a first-order transition. $\xi$ could be interpreted as a measure of the correlation length of the cooperativity. Fig. 4.19, therefore, shows the difference in the correlation length for the presence and absence of a first-order phase transition.

We analyze the spatial pattern of the lipid clusters by dividing each monolayer into three regions: the background phase (bulk, b), the clusters (c) and the interface (i) between the clusters and the bulk. The interfacial region is composed of those acyl chains which have nearest-neighbor bonds close to the cluster boundary. The spatial pattern is then described in terms of the corresponding fractional areas of the membrane (*i.e.* $a_b$, $a_c$, and $a_i$) and the relative occurrences of acyl-chain states in the different regions.

Fig. 4.20 shows that the fraction of the membrane area in the clusters and in the interfaces is considerably lower in the case of a first-order phase transition. This figure also shows that the fractional areas of the bulk, interface and cluster regions are similar close to $T_m$ in the absence of a phase transition, whereas in the case of a first-order transition the bulk dominates in this temperature range. The interfacial region can be probed by calculating the relative occurrence of the acyl-chain conformational states in the first interfacial layer between the clusters and the bulk. This layer is defined as the set of acyl chains which are connected by nearest-neighbor lattice bonds to the cluster boundary. Fig. 4.21 shows the relative occurrence of the all-*trans* (g), the intermediate (i), and the fluid (f) states in the first interfacial layer. The same quantities are given for the bulk in Fig. 4.22. A comparison of Figs. 4.21 and 4.22 demonstrates that the first interfacial layer is dominated by chains in intermediate conformational states. This kind of soft interface in a cell membrane would certainly have a biological significance (Mouritsen *et al.*, 1992). These figures also show that the variation with temperature in the neighborhood of $T_m$ of the relative occurrences of the different chain states are similar in the absence and in the presence of a first-order phase transition, although considerably sharper in the latter case.

The chain orientational order parameter, $S$, is calculated as follows

$$S = \frac{1}{2} L^{-2} \sum_{n=1}^{2} \sum_{i} \sum_{\alpha=1}^{10} (1.8 A_1 A_\alpha^{-1} - 0.8) \mathcal{L}^n_{\alpha,i}. \qquad (4.15)$$

In order to obtain values of $S$ for a large system over a wide temperature range, we computed this quantity by using the standard Monte Carlo method rather than via Ferrenberg-Swendsen method. In Fig. 4.23 we present the results of the acyl-chain orientational order parameter both in the absence and in the presence of a first-

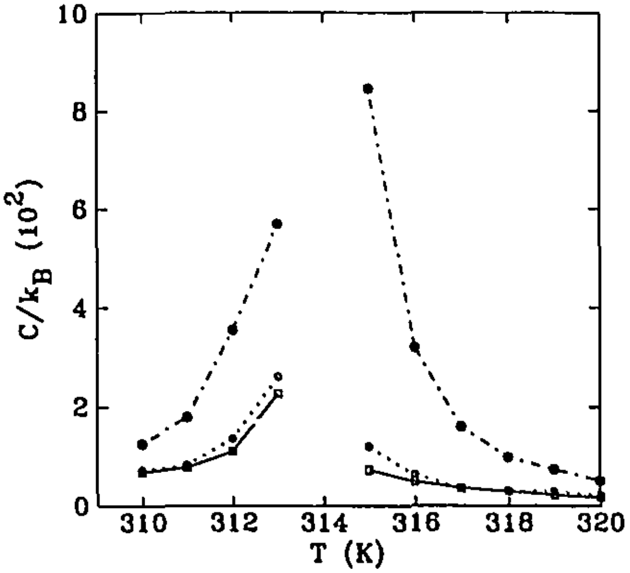

Figure 4.6: Specific heat in the thermodynamic limit for temperatures outside the transition region shown for $\gamma_{mis} = 0, 4, 5 \times 10^{-16}$ erg/$\AA$ (from top to bottom). The specific heat is in units of $k_B$.

order phase transition. Theoretical results, Eq. (4.15), were obtained from model simulations on a $60 \times 60$ bilayer. We also show the experimental data of Davis (Davis, 1979) for $S$ obtained from the first moment of the quadrupolar nuclear magnetic resonance spectrum of $d_{62}$-DPPC bilayers. The experimental order-parameter data exhibit a sharp variation in the transition region. The model results in the presence of a first-order phase transition also exhibit a sharp jump at $T_m$, which is in closer agreement with the experimental results. In contrast, the Pink model gives a curve for $S$ which is much smoother than the experimental results. The reason for the difference in the value of $T_m$ between the experimental and theoretical results is related to the fact that the experiments were performed on fully deuterated chains whereas the theory applies to fully protonated chains. In fact the pretransition of DPPC bilayers has not been considered in the theoretical analysis, whereas it clearly affects the experimental results.

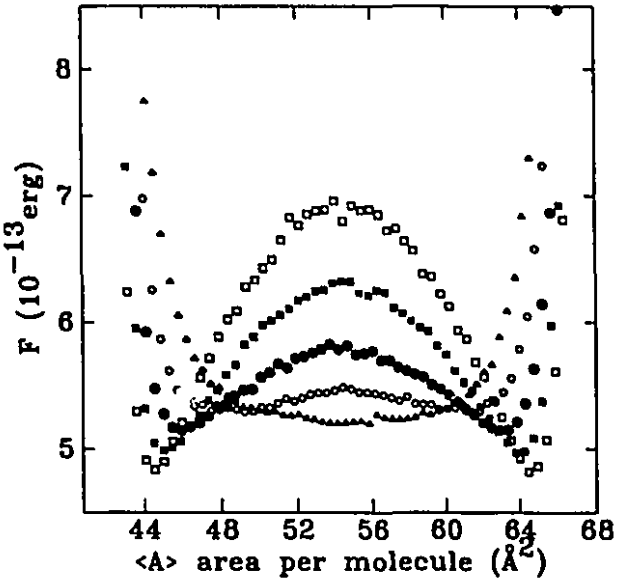

Figure 4.7: Free energy $\mathcal{F}(T_m(L))$ for $\gamma_{mis} = 1\text{–}5 \times 10^{-16} erg/\AA$ (from bottom to top) and $L = 24$.

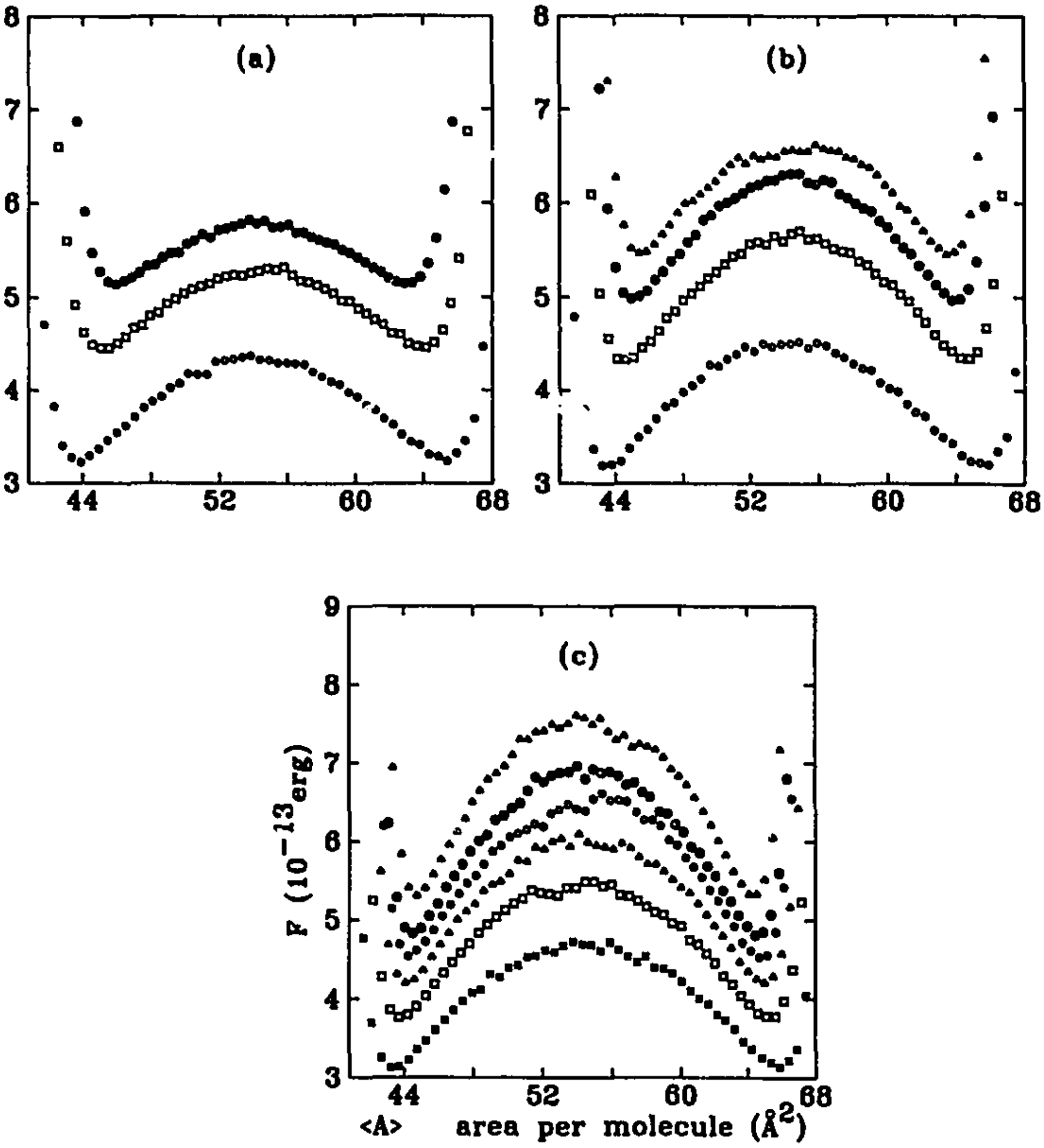

Figure 4.8: $\mathcal{F}(T_m(L))$ for (a) $L = 8, 16, 24$ and $\gamma_{mis} = 3 \times 10^{-16} erg/\mathring{A}$; (b) $L = 8, 16, 24, 32$ and $\gamma_{mis} = 4 \times 10^{-16} erg/\mathring{A}$; (c) $L = 8, 12, 16, 20, 24, 32$ and $\gamma_{mis} = 5 \times 10^{-16} erg/\mathring{A}$.

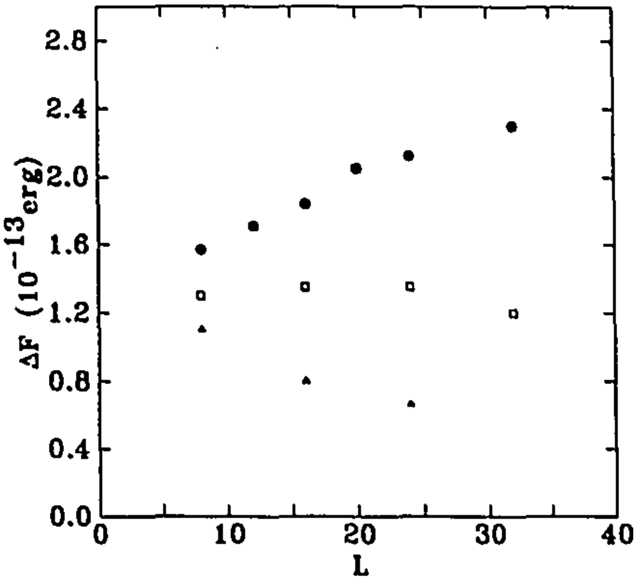

Figure 4.9: Peak height $\Delta F(T_m(L))$ for $\gamma_{mis} = 3\text{-}5 \times 10^{-16} erg/\AA$. The solid points correspond to $\gamma_{mis} = 5 \times 10^{-16} erg/\AA$.

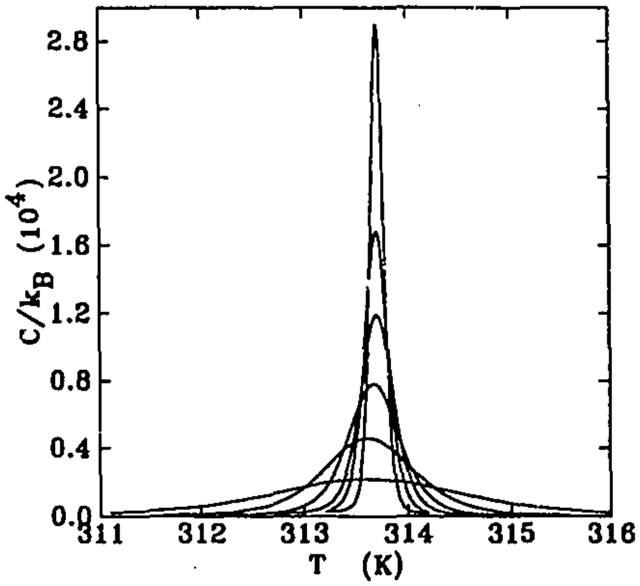

Figure 4.10: Temperature dependence of the specific heat, C(T), for $L = 8, 12, 16, 20, 24, 32$ and $\gamma_{mis} = 5 \times 10^{-16} erg/\AA$.

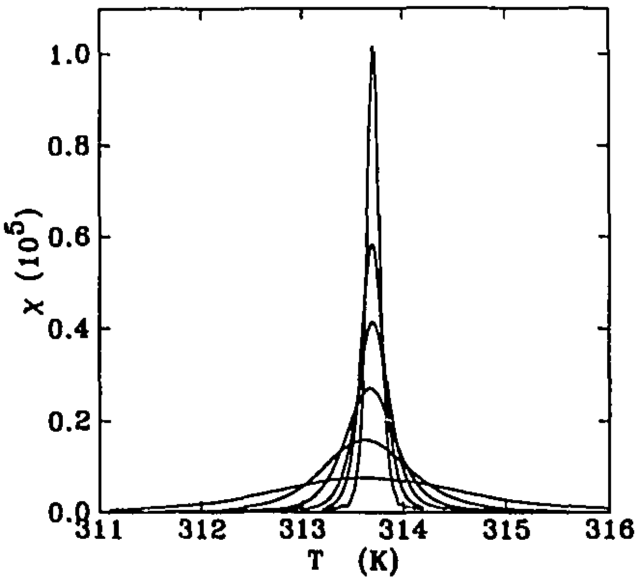

Figure 4.11: Temperature dependence of the lateral compressibility, $\chi(\text{T})$, for $L = 8, 12, 16, 20, 24, 32$ and $\gamma_{mis} = 5 \times 10^{-16}$ erg/$\AA$. The lateral compressibility is in units of $10^{13} \AA^4$ erg$^{-1}$.

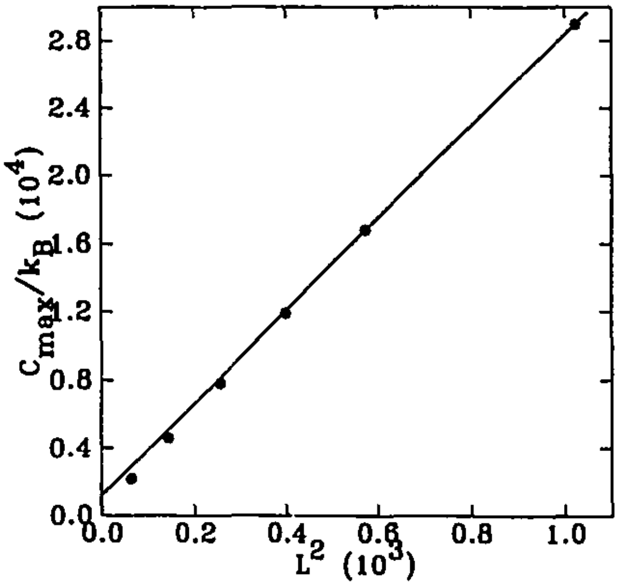

Figure 4.12: Dependence of the specific-heat maximum on $L^d$ for $L = 8, 12, 16, 20, 24, 32$ and $\gamma_{mis} = 5 \times 10^{-16} erg/\AA$.

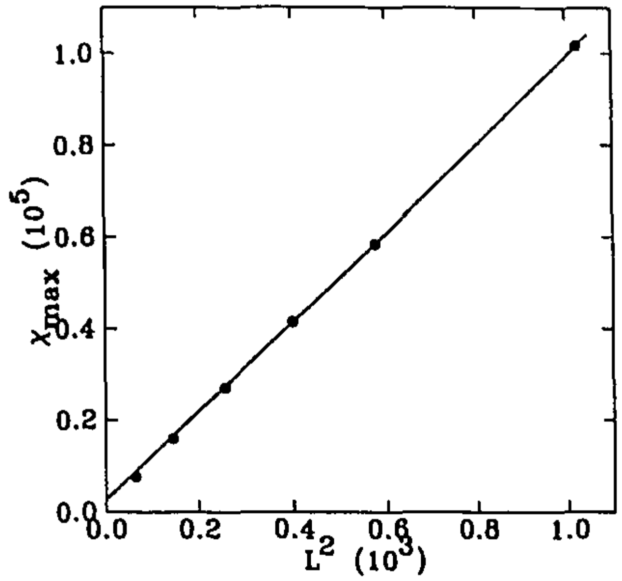

Figure 4.13: Dependence of the lateral compressibility maximum on $L^d$ for L= $8,12,16,20,24,32$ and $\gamma_{mis} = 5 \times 10^{-16} erg/\AA$. The lateral compressibility is in units of $10^{13}\AA^4 erg^{-1}$.

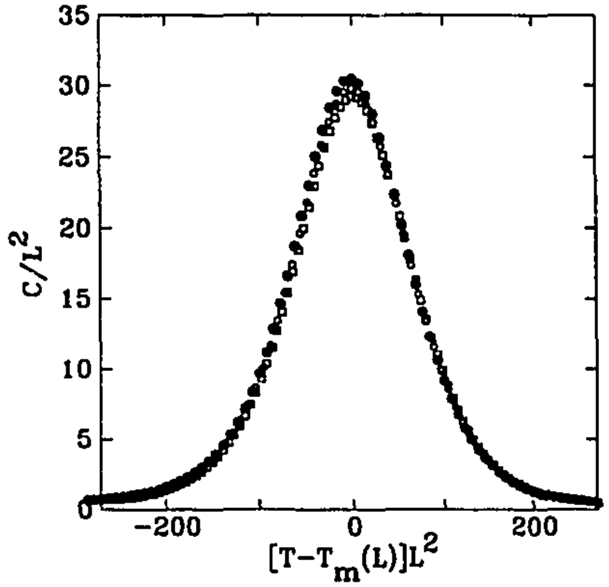

Figure 4.14: Scaling function for the specific heat for L= $16,20,24,32$ and $\gamma_{mis} = 5 \times 10^{-16} erg/\AA$. The specific heat is in units of $k_B$.

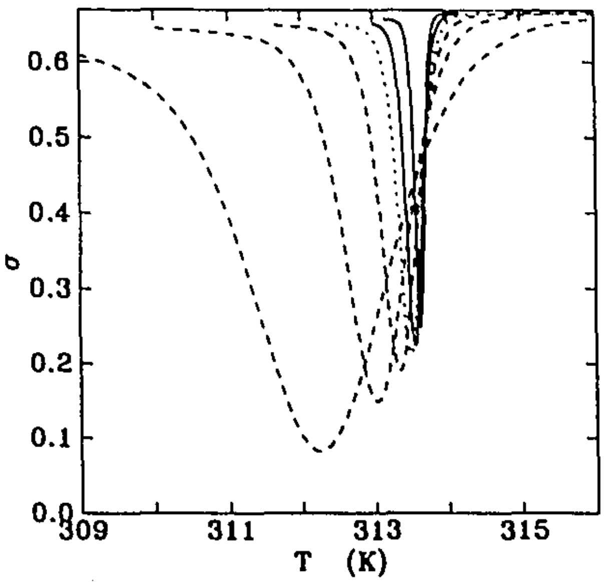

Figure 4.15: The fourth-order cumulant $\sigma_L$ as a function of temperature for $L = 8, 12, 16, 20, 24, 32$ and $\gamma_{mis} = 5 \times 10^{-16} erg/\AA$. The data was obtained from the same simulations as used for Fig. 4.10.

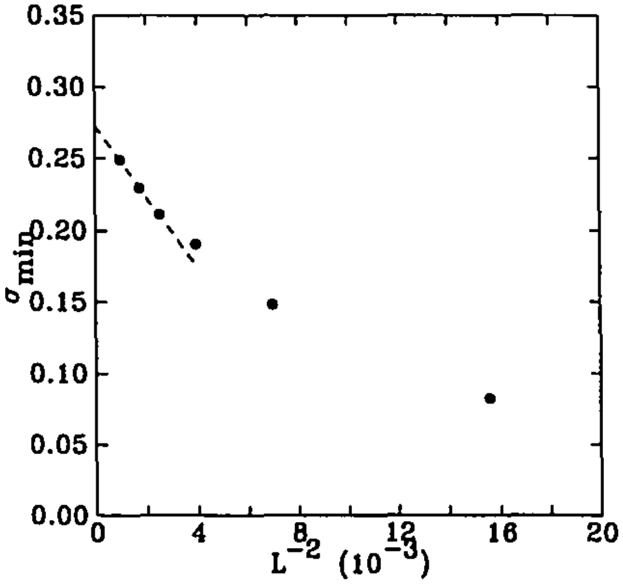

Figure 4.16: Dependence of $\sigma_{min}$ on $L^{-d}$. Results for the non-trivial limit are given by the dashed line.

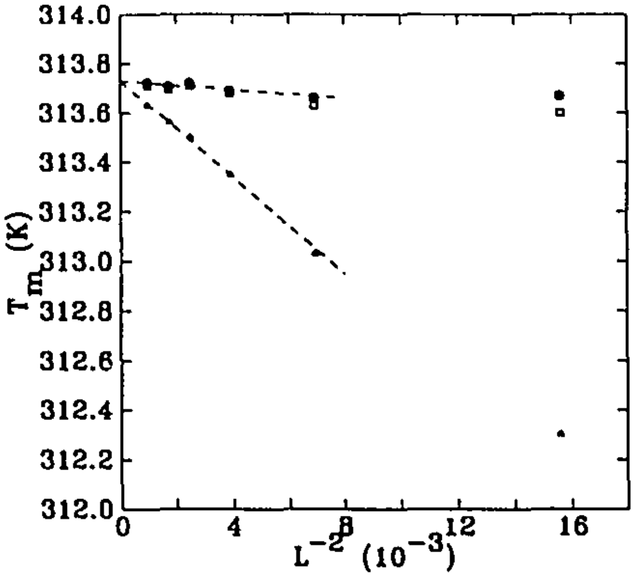

Figure 4.17: Finite-size transition temperatures $T_m^{\mathcal{F}}(L)$, $T_m^{C}(L)$, and $T_m^{\sigma}$, as determined by the free energy $\mathcal{F}(A_1, T_m(L)) = \mathcal{F}(A_2, T_m(L))$, the maximum of the specific heat (or the lateral compressibility), and the minimum of the fourth-order cumulant, respectively. The mismatch parameter is $\gamma_{mis} = 5 \times 10^{-16} erg/\AA$.

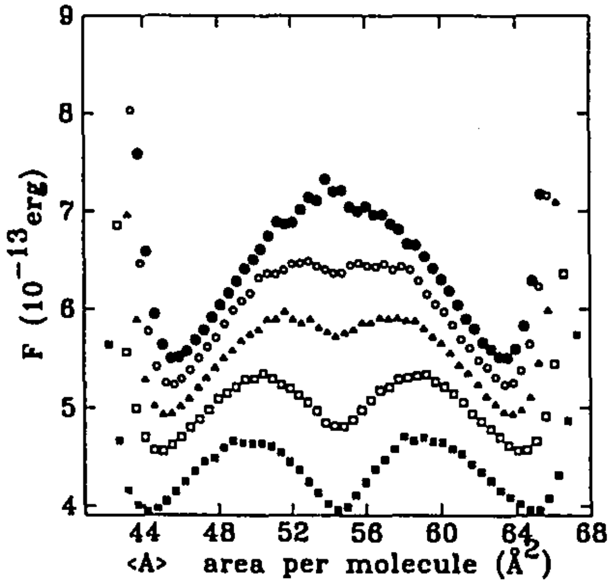

Figure 4.18: Free energy $\mathcal{F}(T_m(L))$ as a function of order parameter, $\langle A \rangle$, for lattice sizes $L \times L$, $L = 8, 12, 16, 20, 24$ from bottom to top, for $\gamma_{mis} = 4 \times 10^{-16}$erg/Å and $J_2/J_0 = 0.04$. $T_m(L)$ refers to the transition temperature for a system of linear size $L$.

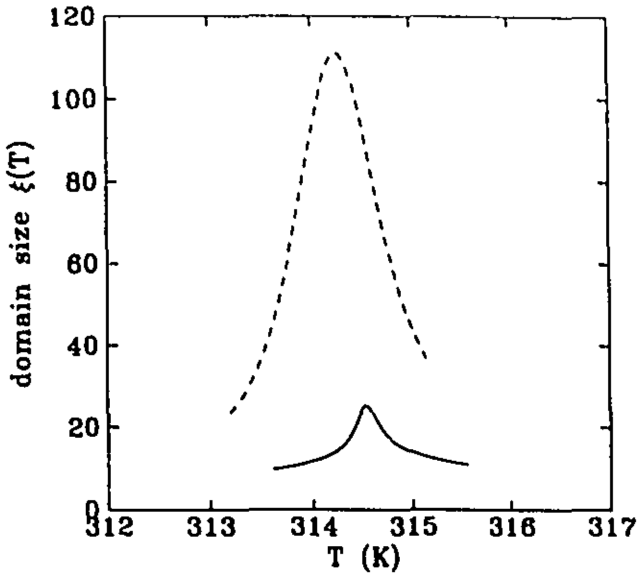

Figure 4.19: Average domain size (number of chains), $\xi(T)$, as a function of temperature for the Pink model (dashed line) and the model with mismatch and intermonolayer interactions (solid line), respectively. The curves are obtained from Ferrenberg-Swendsen simulations on a 24 × 24 lattice. The lower cut-off cluster size is taken to be three acyl chains.

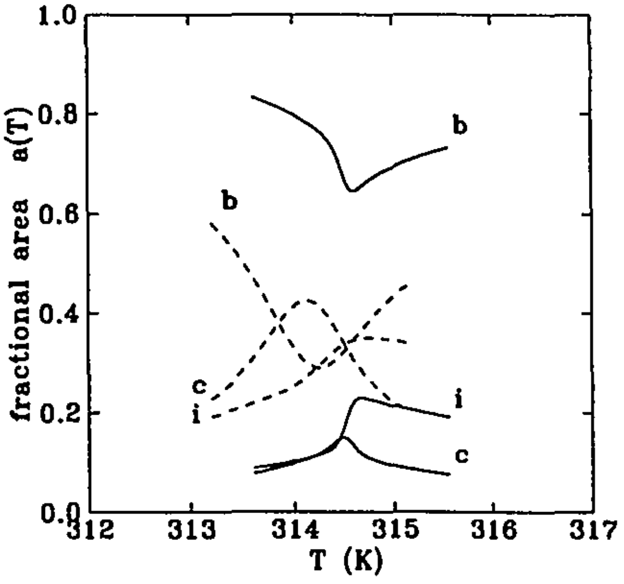

Figure 4.20: Temperature dependence of the fractional areas, $a(T)$, in the bulk (b), in the clusters (c), and in the first interfacial layer (i) for the Pink model (dashed lines) and for the model with mismatch and interlayer interactions (solid lines). Both sets of results are obtained from a 24 × 24 lattice using the Ferrenberg-Swendsen method.

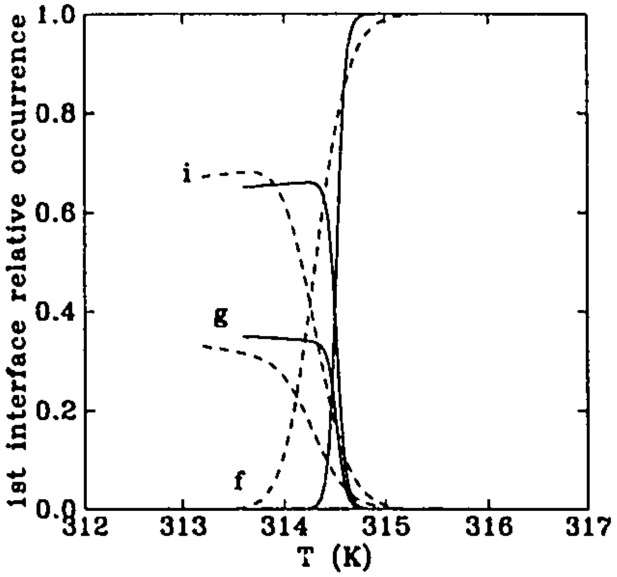

Figure 4.21: Relative occurrence of gel (g), intermediate (i), and fluid (f) acyl-chain conformational states in the first interfacial layer of lipids chains for the Pink model (dashed lines) and for the model with mismatch and interlayer interactions (solid lines). The results are obtained from a $24 \times 24$ lattice using the Ferrenberg–Swendsen method.

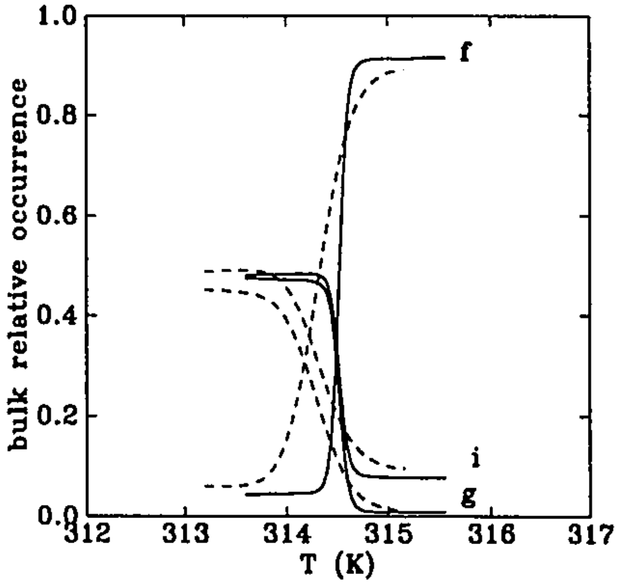

Figure 4.22: Relative occurrence of gel (g), intermediate (i), and fluid (f) acyl-chain conformational states in the bulk for the Pink model (dashed lines) and for the model with mismatch and interlayer interactions (solid lines). The results are obtained from a $24 \times 24$ lattice using the Ferrenberg–Swendsen method.

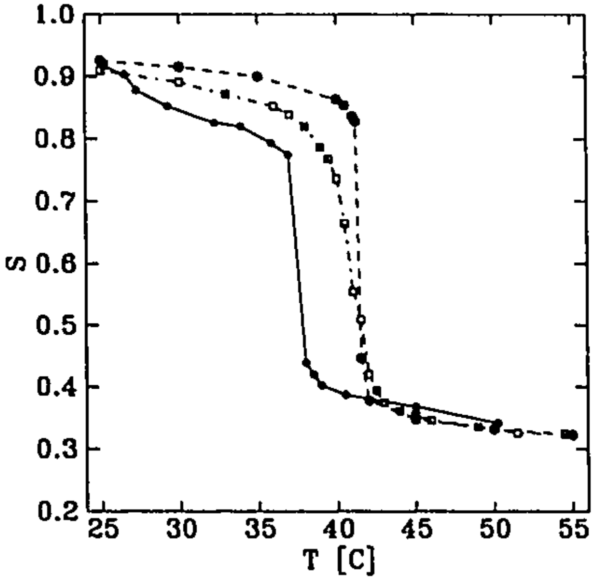

Figure 4.23: Acyl-chain orientational order parameter, $S$, as a function of temperature. Theoretical results shown for the Pink model (□) and for the model with mismatch and interlayer interactions (•). Experimental data (∘) shown for $d_{62}$-DPPC lipid bilayers (Ref. (Davis, 1979)).

# Chapter 5

# Protein–Lipid Mixtures

In this chapter, we present microscopic lattice models for lipid–protein and lipid–polypeptide mixtures in order to study the effects of proteins on the physical properties of lipid bilayers, gramicidin channel formation and the phase diagram for the binary mixtures, based on the models in the previous chapter.

## 5.1 Introduction

Proteins are the most abundant organic molecules in cells, constituting 50% or more of their dry weight (Lehninger, 1979). They are found in every part of every cell and they are fundamental for all aspects of cell structure and function. There are many different kinds of proteins, each specialized for a different biological function. A fundamental question arises as to how the proteins affect the properties of lipid systems and, conversely, how the lipids modulate protein function.

So far, little is known regarding internal molecular conformational states of integral membrane proteins and their relation to modes of protein activity. The bulk of our quantitative information on the physical effects of the interaction between lipids and proteins is concerned with the perturbing effects of proteins on their lipid environment (Mouritsen and Sperotto, 1992). However, it seems reasonable to postulate that most integral (trans-bilayer) membrane proteins have as part of their structure $\alpha$-helices, which have predominantly hydrophobic residues and which span the hydrophobic region of the lipid bilayer (Henderson, 1981). This implies that there are well-defined restrictions on the length and hydrophobicity of the proteins. This leads to the concept of *hydrophobic matching* between the hydrophobic length of protein and the hydrophobic thickness of the surrounding lipid bilayer matrix (Owicki, Springgate and McConnell, 1978; Owicki and McConnell, 1979). The hydrophobic matching therefore is an important component of lipid–protein interactions in membranes. Hence, in the models studied in this chapter, the effect of lipid–protein mismatch is considered to be fundamental in the understanding the influence of proteins on lipid bilayers (Sec. 5.2), the instability of the gramicidin channel (Sec. 5.3) and the phase separation of the lipid–protein and lipid–polypeptide mixtures with a lower critical mixing point (Sec. 5.4).

A protein incorporated in the lipid bilayer usually perturbs the physical properties of the surrounding lipids, such as their hydrocarbon chain order (Morrow and Davis, 1988). Since the order of the lipid chain in the fluid phase is linearly related to the hydrophobic thickness of the bilayer [Eq. (4.4)], a protein in the lipid bilayer can induce a local variation in lipid hydrophobic thickness. In Sec. 5.2, we study these effects on the basis of the lipid model described in Sec. 4.3.2 and then compare them with the results of Sperotto and Mouritsen based on the Pink model (Sperotto and Mouritsen, 1991). We also investigate the influence of proteins on the correlations between lipids by introducing a new correlation function.

Gramicidin *A* is a linear antibiobic polypeptide which forms ionic channels in lipid bilayers. The channel exists as a dimer of helical $\beta_{LD}$ structure spanning the bilayer (Urry *et al.*, 1971). The dimer has a finite lifetime of about 0.1 seconds which influences the conducting properties of the system (Gennis, 1989). The conformation of gramicidin *A* molecules does not depend strongly on the thickness of the lipid bilayer into which it is embedded, whereas the lifetime of the channel depends strongly on bilayer thickness. The lifetime has its maximum for a hydrophobic bilayer thickness which is close to the hydrophobic length of the channel. Due to the hydrophobicity and structure of gramicidin $A$, gramicidin–lipid systems are ideally suited model membranes for the study of lipid–protein interactions which are not influenced by hydrophilic interactions. Therefore the kinetics of the channel formation and its dependence on temperature and on the thickness of lipid bilayer have been a subject of interest for both experimental and theoretical studies (O'Connell, Koeppe II and Andersen, 1990; Kolb and Bamberg, 1977; Bamberg and Laüger, 1974; Huang, 1986). However, most of the studies are concerned one channel opening at a time. In Sec. 5.3 we study the equilibrium channel density and its dependence on temperature and lipid-protein interactions by simulating a microscopic model of lipid–gramicidin mixtures.

The presence of transmembrane amphiphilic proteins or polypeptides in lipid membranes has considerable influence on the phase equilibria of the mixed system (Mouritsen and Sperotto, 1992). In particular the lipid-protein interactions give rise to phase-separation (Huschilt, Hodges and Davis, 1985; Morrow, Huschilt and Davis, 1985; Morrow and Davis, 1988). Despite considerable experimental studies on lipid–protein interactions in recent years, only a few phase diagrams of lipid–protein mixtures have been elucidated with sufficient accuracy to allow a theoretical interpretation in terms of the details of lipid–protein interactions. The difficulty in obtaining accurate experimental phase diagrams for lipid–protein and lipid–polypeptide mixtures is related to several different circumstances. It is, for example, common that most experiments do not give information on the free energy of the mixture directly but rather certain derivatives of the free energy, such as the specific heat and the spectroscopic order parameters. It is often difficult to determine the position of phase boundaries based on these derivatives without invoking certain model assumptions. Furthermore apparent anomalies in the specific heat are not sufficient to determine the existence of a phase transition or a phase boundary and spectroscopic order parameters depend in principle on certain intrinsic time and length scales of the experimental technique in question.

In Sec. 5.4, we propose a lattice model (Zhang *et al.*, 1992c) to describe the phase diagram of phospholipid bilayers containing small transmembrane proteins or polypeptides. The model is based on the extended Pink model described in Sec. 4.3.1. The interaction between the lipid bilayer and the protein or polypeptide is modeled using the concept of hydrophobic matching. The phase diagram has been derived by computer simulation techniques which fully account for thermal density fluctuations and operate on the level of the free-energy thereby permitting an accurate identification of the phase boundaries. The calculations predict a closed loop of gel–fluid coexistence with a lower critical mixing point, which is in agreement with recent experimental measurements on phospholipid bilayers mixed with synthetic transmembrane amphiphilic peptides or with gramicidin $A$ (Morrow, Huschilt and Davis, 1985; Morrow and Davis, 1988).

## 5.2 Lipid Order Parameter Profiles around Proteins

On the basis of the mattress model (Mouritsen and Bloom, 1984), Sperotto and Mouritsen (Sperotto and Mouritsen, 1991) introduced lipid–protein interactions into the Pink model by assuming that the hydrophobic membrane-spanning part of the protein molecule is a stiff, rod-like and hydrophobically smooth object with no appreciable internal flexibility (Owicki, Springgate and McConnell, 1978; Jähnig, 1981; Sadler and Worcester, 1982). The protein is therefore characterized only by a cross-sectional area, $A_P$, (or circumference $\rho_P$) and a hydrophobic half-length, $d_P$. The Hamiltonian describing the lipid-protein interaction for a bilayer composed of two monolayers can be written as follows

$$\begin{aligned} \mathcal{H}_{LP} &= \Pi A_P \sum_i L_{P,i} + \frac{\gamma}{2}(\frac{\rho_P}{z}) \sum_{\langle i,j \rangle} \sum_{\alpha,\beta} |d_\alpha + d_\beta - 2d_P| \mathcal{L}^1_{\alpha,i} \mathcal{L}^2_{\beta,i} L_{P,j} - \\ & \frac{\eta}{2}(\frac{\rho_P}{z}) \sum_{\langle i,j \rangle} \sum_{\alpha,\beta} min(d_\alpha + d_\beta, 2d_P) \mathcal{L}^1_{\alpha,i} \mathcal{L}^2_{\beta,i} L_{P,j} \end{aligned} \tag{5.1}$$

where $z$ is the coordination number and $z = 6$ for the hexagonal lattice. $L_{P,i}$ is the protein occupation variable, which satisfy the completeness relation $\sum_\alpha \mathcal{L}_{\alpha,i} + L_{P,i} = 1$.

The parameters $\gamma$ and $\eta$ refer to the mismatch and the van der Waals interaction respectively. The total Hamiltonian of the model is therefore

$$\mathcal{H} = \mathcal{H}_{LL} + \mathcal{H}_{LP}, \tag{5.2}$$

where $\mathcal{H}_{LL}$ is the Hamiltonian for pure lipid bilayers. In order to describe the thickness profile of lipids near an isolated protein, Sperotto and Mouritsen (Sperotto and Mouritsen, 1991) introduced a decay length, $\xi$, defined by the following relation,

$$< d_L(I) > = < d_L^\circ > + (d_P - < d_L^\circ >) e^{-D(I)/\xi} \tag{5.3}$$

where $< d_L^\circ >$ is the mean thickness of the pure lipid bilayer at a given temperature, D(I) is the distance of the lipid from the protein, and $I$ is an index for the lipid layers around the protein. Sperotto and Mouritsen then calculated the decay length for the Pink model, *i.e.* $\mathcal{H}_{LL} = \mathcal{H}_0$. However, as we now know, there is no phase transition in the Pink model for the calculated parameters in the thermodynamic sense (Sec. 4.2.2). Hence it is useful to make a similar study for the bilayer model described in Sec. 4.3.2 and compare the effects of proteins on the properties of lipids for both cases, *i.e.* in the presence and in the absence of a first-order phase transition. Here we use $\gamma = 0.01 \times 10^{-13}$ erg $\mathring{A}^{-2}$ and $\eta = 0.03 \times 10^{-13}$ erg $\mathring{A}^{-2}$ (Sperotto and Mouritsen, 1991).

We simulated both cases by choosing different coupling parameters, $J_2$ and $\gamma_{mis}$, in the pure lipid bilayer model of Sec. 4.3.2. The system then undergoes a first-order phase transition for the case of $J_2 = 0.04J_0$ and $\gamma_{mis} = 0.004 \times 10^{-13} erg/\mathring{A}$ and is equivalent to the Pink model for $J_2 = 0$ and $\gamma_{mis} = 0$ (Sec. 4.4.2). The protein is assumed to take up seven sites forming a hexagonal shape with a side length of two sites since integral proteins like gramicidin $A$ or the polypeptides may be modeled by this way (Chapman *et al.*, 1977; Davis *et al.*, 1983). The thickness profiles of bilayer near the 7-site protein at different temperatures for both cases are presented in Figs. 5.1 and 5.2, where $d_P = 16\mathring{A}$, respectively. It is shown that the protein-induced disturbance of the lipid bilayer decays with increasing distance from the protein and it is clearly temperature dependent. The profiles result in the occurrence

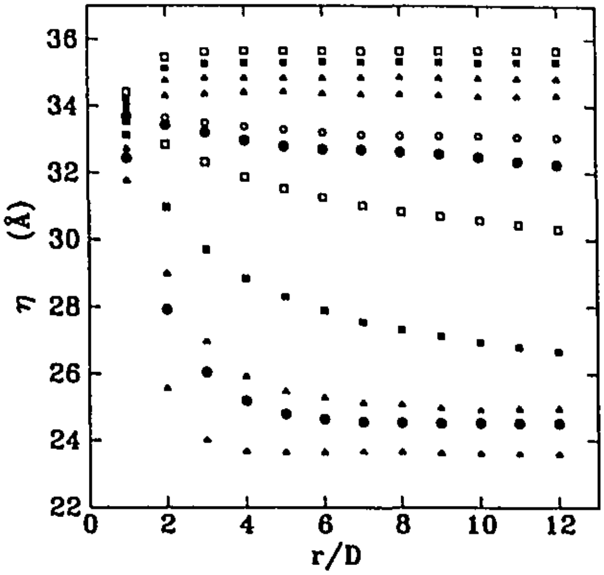

Figure 5.1: Bilayer thickness as a function of distance to the protein for a variety of temperatures in the Pink model. $T$ = 300, 305, 309, 311, 313, 313.5, 314, 315, 317, 319, 330 $K$ from top to bottom.

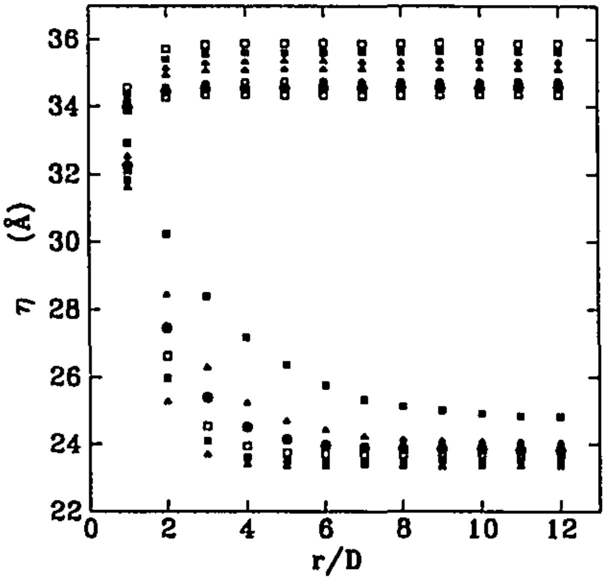

Figure 5.2: Bilayer thickness as a function of distance to the protein for a variety of temperatures in the extended model. $T$ = 300, 305, 309, 311, 313, 313.5, 314, 315, 317, 319, 321, 325, 330 $K$ from top to bottom.

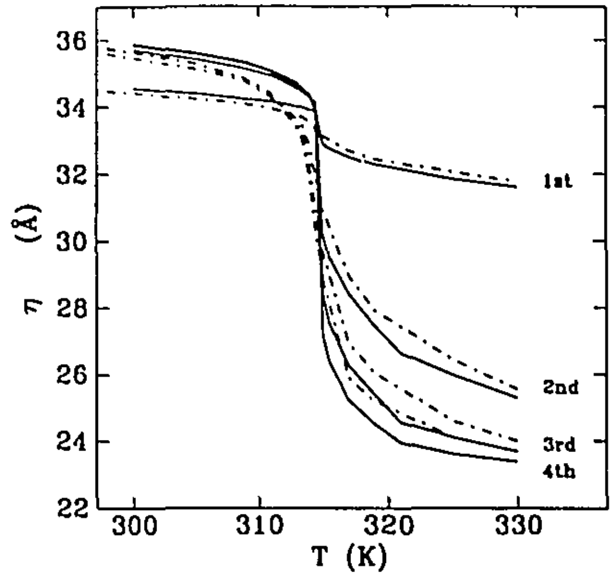

Figure 5.3: Thickness in the first four layers around the protein as a function of temperature for the extended Pink model (solid lines) and for the Pink model (dotdashed lines).

of a correlation between lipid molecules and a competition between the lipid–lipid interactions and the lipid–protein mismatch. Since the correlations in the pure lipid bilayer are stronger in the temperature region close to the transition, the disturbance due to the presence of the protein can extend beyond the first few molecular layers in this region. The effect of the protein also rapidly decays outside this region. While the decay length, $\xi$, indicates the range of lateral correlations for the lipid bilayer, the hydrophobic thickness of the first lipid layer around the protein is a measure of the competition between the interactions of the first layer lipids with the protein and with their neighboring lipid molecules respectively. For the cases shown in Figs. 5.1 and 5.2, the hydrophobic length of the protein is less than the mean thickness of lipid bilayer in the gel phase but is greater in the fluid phase. Because the interactions between the lipid molecules are weaker in the fluid phase and stronger in the gel phase, the thickness of the first layer in the fluid phase can be stretched to match the length of the protein completely while the reduction of the thickness in gel phase is limited.

There is a striking difference between the profiles for the two cases. For example

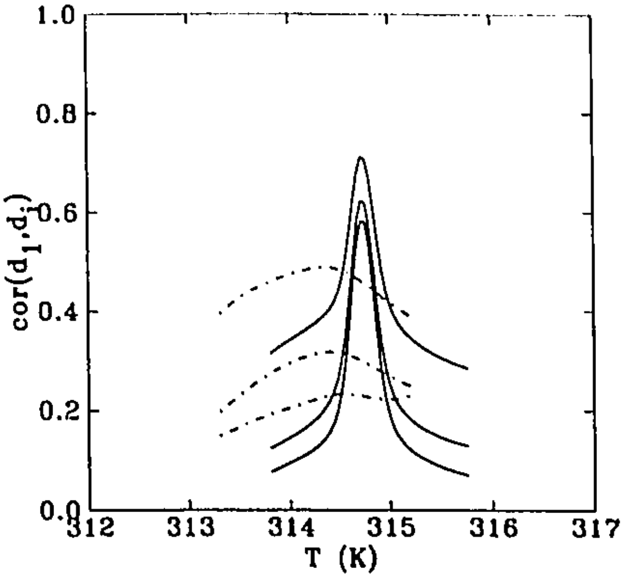

Figure 5.4: The thickness correlations as function of temperature for the extended Pink model (solid lines) and for the Pink model (dotdashed lines). In both cases the curves from top to bottom correspond to i=2,3,4.

profiles of the hydrophobic thickness vary more dramatically with temperature $T$ in Fig. 5.2 than in Fig. 5.1. The hydrophobic thickness of the first four layers as a function of temperature is shown in Fig. 5.3. There are abrupt changes of the hydrophobic thickness for all the layers at the transition temperature, although the jumps in the thickness are not all equal. This is characteristic of a first order phase transition.

It is shown, in Figs. 5.1 and 5.2, that the relation in Eq. (5.3) is not valid at the phase transition so that we cannot define the decay length, $\xi$, in the transition temperature region. Since the decay length, $\xi$, is dependent on the correlation between the lipid molecules, we examine the correlations in the lipid bilayer directly. The hydrophobic thickness correlation function of lipid molecules is here defined as

$$cor(d_1, d_i) = \frac{< d_1 d_i > - < d_1 >< d_i >}{\sigma_1 \sigma_i} \tag{5.4}$$

where $\sigma_i = [< d_i^2 > - < d_i >^2]^{\frac{1}{2}}$, and $d_i$ is the thickness of $i$-th layer around a reference center. Here the index $i$ refers to the distance away from the central site. When this site is occupied by a protein, we refer to the correlation function as

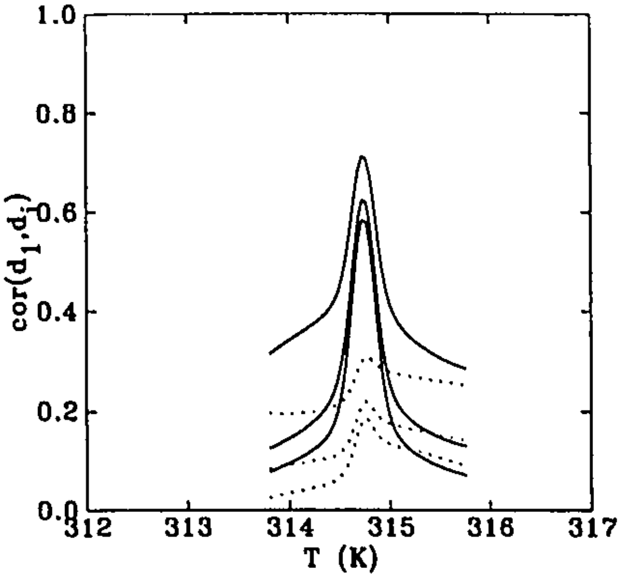

Figure 5.5: The thickness correlations as function of temperature for the extended Pink model in the absence of a protein (solid lines) and in the presence of the protein (dotdashed lines).

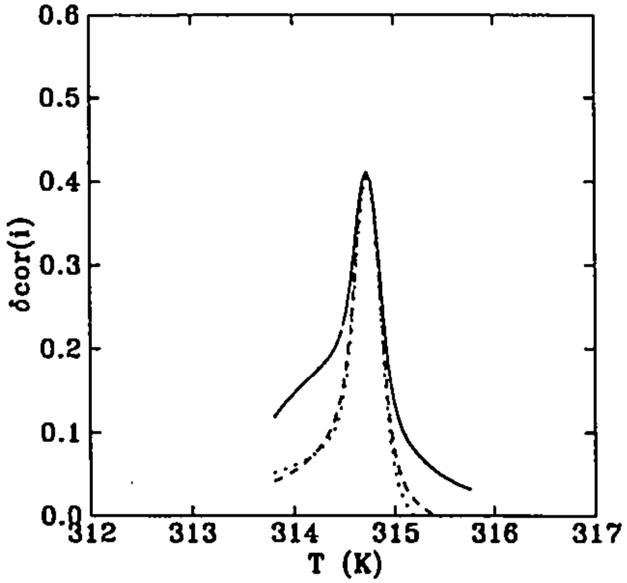

Figure 5.6: $\delta cor(i)$ as functions of temperature for $i = 2$ (solid line), 3 (dashed line), and 4 (dotdashed line) for the extended Pink model.

$cor(d_1, d_i)_P$ to distinguish it from the non-protein case.

The correlations are shown in Fig. 5.4 as functions of temperature $T$ for the two cases (with and without a first order transition) in the pure lipid bilayer. The three curves presented for each case correspond to $i = 2, 3, 4$ respectively. The correlation function for $i = 2$ has the largest values at all temperatures for both cases. As expected, there are strong correlations at the transition temperature $T_m$ for the first order transition case. Beyond the transition region, the correlations are weaker than that for the case with no transition. This is consistent with other observations such as the specific heat and the lateral compressibility (Sec. 4.4.1). However the correlations between lipid molecules are suppressed in the presence of proteins. This is shown in Fig. 5.5, where the curves for the correlation function are presented for both in the presence and in the absence of the protein. These results are consistent with the recent experimental observations by Watnick *et al.* for the mixtures of gramicidin and lecithin (Watnick and Chan, 1990). The results obtained from their $^2H$-NMR relaxation measurements indicate that the peptide disrupts the cooperative fluctuations characteristic of pure multilamellar lipid dispersions through the hydrophobic mismatch between itself and the lipids.

The quantity $\delta cor(i) = cor(d_1, d_i) - cor(d_1, d_i)_P$ is a measure of the effect of the protein on the hydrophobic thickness of the lipid bilayer. $\delta cor$ is shown as a function of $T$ in Fig. 5.6. Since $\delta cor(2) \approx \delta cor(3)$ and $\delta cor(1) \geq \delta cor(2)$, the effect of proteins on the lipid bilayer is very short range except at the transition. A longer range effect occurs at the transition since $\delta cor(i)$ has the same values for $i = 2, 3, 4$. Therefore, use of this analysis allows us reach a conclusion similar to that Sperotto and Mouritsen obtained from their decay length calculations. They found that the perturbation by proteins on the surrounding lipids is strongly dependent on temperature and reach its maximum at the transition (Sperotto and Mouritsen, 1991).

## 5.3 Thermal Equilibrium and Gramicidin Channel Formation

The cation permeability of lipid bilayers increases in the presence of the linear pentadecapeptide, gramicidin $A$ (Wagner *et al.*, 1972). It is known that gramicidin $A$ forms dimeric channels consisting of two monomers that are linked by of the order of six hydrogen bonds (Hladky and Haydon, 1972; Bamberg and Laüger, 1974). When two molecules of gramicidin $A$, one in each monolayer, form a linear dimer, an ion-specific channel through the bilayer is created. The channel loses its ionic conductivity when it dissociates into monomeric units. Studies of the statistics of channel opening by conductance measurements show that the dimers (channels) and monomers are in thermal equilibrium (Hladky and Haydon, 1972; Bamberg and Laüger, 1973; Zingsheim and Neher, 1974),

$$G + G \rightleftharpoons G_2 \tag{5.5}$$

where $G$ and $G_2$ represent the gramicidin monomers and dimers respectively.

Most experimental results for the mean lifetime of a single channel support the assumption that the mismatch between the gramicidin dimer (a channel) and the lipid bilayers mainly accounts for the dissociation of the gramicidin dimer (Elliott *et al.*, 1983). For example, the mean lifetime of gramicidin channels in monoacylglycerol–squalene bilayers was found to increase as the bilayer thickness decreases from 28.5 to 21.7 $\AA$ while the hydrophobic length of the channel is assumed to be 21.7 $\AA$. This is consistent with the fact that a decrease in mismatch makes the dimeric state more stable.

There have been many theoretical studies on the kinetics of the channel formation and its dependence on membrane structure. A theoretical model was proposed for the relation between the mean lifetime of gramicidin channels and the thickness of lipid bilayers by Elliott *et al.* (Elliott *et al.*, 1983) and was modified by Huang (Huang, 1986) in term of deformation of the bilayer. The basic idea of the model is as follows: when a dimeric gramicidin channel is formed in a membrane of thickness greater than the length of the channel, the membrane deforms locally to accommodate the channel. Then the restoring force of the deformed membrane will reduce the stability of the dimer. The dissociation constant $k_D$ can in this case be estimated from (Huang, 1986)

$$k_D = \nu e^{-g^*/k_B T} \tag{5.6}$$

where $g^*$ is the free energy of activation, which is the energy required to break the hydrogen bonds linking two monomers, and $\nu$ is a frequency factor almost independent of temperature.

Here we simulate dimer formation on a microscopic level. The assumption that the hydrocarbon chains of lipids adapt to the thickness of the hydrophobic core of a protein in the membrane is the basis of the mattress model, which allows us to formulate a microscopic model for gramicidin channels in the lipid bilayers using the bilayer model discussed in Sec. 4.3.2. Even though the parameters in the bilayer model has been determined for DPPC bilayers only, we assume that the mechanics of channel dissociation is valid for all phospholipid bilayers, *i.e.* the mismatch between the gramicidin dimer and the bilayers should still account for the instability of the channels.

The microscopic model consists of two parts: the model of pure lipid bilayers which is described in Sec. 4.3.2 and the coupling of the gramicidin monomers or dimers incorprated in the bilayers to lipid molecules. By analogy with the interactions between the acyl chains, the interactions between lipid molecules and gramicidin monomers are then written as follows,

$$\begin{aligned}\mathcal{H}_{LG} \;=\; & \sum_{n=1}^{2}\{\sum_i \Pi A_G \mathcal{L}^n_{M,i} - \frac{J_{LG}}{2}(\frac{d_G}{d_1})\sum_{\langle i,j\rangle}\sum_{\alpha=1}^{10} I_\alpha \mathcal{L}^n_{\alpha,i}\mathcal{L}^n_{M,j}\} - E_H \sum_i \mathcal{L}^1_{M,i}\mathcal{L}^2_{M,i} + \\ & \frac{\gamma^{LG}_{mis}}{2}\sum_{\langle i,j\rangle}\sum_{\alpha,\beta}|d_\alpha + d_\beta - 2d_G|\mathcal{L}^1_{\alpha,i}\mathcal{L}^2_{\beta,i}\mathcal{L}^1_{M,j}\mathcal{L}^2_{M,j}.\end{aligned} \tag{5.7}$$

$\mathcal{L}^n_{M,i}$ is the occupation variable for gramicidin monomers which is unity when the $i$-th site of the $n$-th monolayer is occupied by a gramicidin monomer and zero otherwise. In this approximation the hydrophobic part of the gramicidin monomer is assumed to be a stiff rod-like object with no internal flexibility. It can therefore be characterized by a cross-section area, $A_G$, and the length of the hydrophobic core, $d_G$. $J_{LG}$ is the direct lipid–protein interaction constant, which depends on the properties of gramicidin hydrophobic surface. The parameter, $\gamma^{LG}_{mis}$, is related to the hydrophobic effect describing the hydrophobic area exposed by the longer species to water. $E_H$ is the strength of the hydrogen bonding between the two monomers of a dimer.

In the model of Eq. (5.7) it is assumed for computational convenience that the monomers are single-site objects on the lattice substituting for a single acyl chain. It is however possible to relate the results of this model to those of the experimental situation where the monomers occupy about seven adjacent lattice sites by a simple scaling, though this is clearly an approximation. From a scaling argument, we choose $E_H \approx 2 \times 10^{-13} erg$ as a single hydrogen bond instead of six or seven hydrogen bonds. Although the approximation overestimates the mixing entropy, it works quite well in the lipid–protein model described in Sec. 5.4. Finally we only consider the case of $d_G = d_{10} = 11.25\mathring{A}$ because experiments (Elliott *et al.*, 1983; Huang, 1986) suggest that the hydrophobic thickness of gramicidin channels matches the thickness of the membrane exactly in fluid phase. Consequently the value of $\gamma^{LG}_{mis}$ is chosen to be the same as $\gamma_{mis}$ (Sec. 5.4).

The equilibrium dimer probability, $P_{eq}$, is defined as the percentage of dimers in thermodynamic equilibrium and is therefore a measure of the tendency to form ionic channels. The dimer probability is affected by several factors, such as the temperature, the mismatch condition between the gramicidin dimer and the lipid chains, and the direct lipid–protein interaction. An increase in temperature may cause the monomer–monomer bonding in a channel to break, thereby lowering the dimer probability. Temperature also indirectly affects the probability via changes in the hydrophobic thickness of the lipid bilayer. Furthermore the mismatch between the dimers and lipids always tends to break a dimer into two monomers. However the effect of mismatch is dependent on the lateral distribution of the dimers, which is controlled by the strength of the direct van der Waals interactions between lipids and

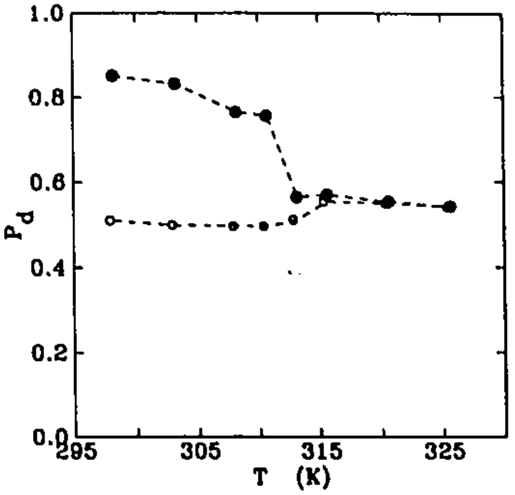

Figure 5.7: Dimer probability as a function of temperature. ○ refers to the data with the van der Waals lipid-gramicidin interaction; ● refers to the data without such an interaction.

proteins. For the case when this attractive interaction is very weak, the gramicidin monomers and dimers aggregate in the bilayer plane in such a way that the contact between lipids and dimers decreases maximally and the effect of mismatch on the channel is therefore suppressed. For the case where the lipid-protein interaction is sufficiently strong, *i.e.* close to the strength of van der Waals interaction between lipid molecules, the gramicidin dimers or monomers disperse considerably so that the environment of each channel will be similar to that of an isolated channel.

The dimer probabilities, $P_{eq}(T)$, are shown in Fig. 5.7 as functions of temperature, $T$, for the cases with and without the direct van der Waals interaction between lipids and gramicidin. The gramicidin-lipid mixture was simulated on two $40 \times 40$ triangle lattices, 3% of which is occupied by gramicidin monomers. It is shown that the equilibrium channel probabilities in the fluid phase of the bilayer are almost the same for the two cases because the lipid-gramicidin interaction in the fluid phase is very weak. However, they are quite different in the gel phase of the bilayer. Indeed the direct lipid-protein interaction, together with the effect of entropy, overcomes the mismatch between the hydrophobic thickness of gramicidin dimers and that of the lipid bilayer and disperses the dimers randomly in the bilayer. In this situation Fig. 5.7 shows that the mismatch is very effective so that the channel probability in the gel phase decreases. In the opposite case, when the direct lipid–protein interaction is very weak, the dimers aggregate in the bilayer so that the mismatch does not affect the channels inside the gramicidin clusters and the entropy effect on the channels decreases. Therefore the channel probability in this case is even higher than in the fluid phase where the hydrophobic thickness of dimers is closely matched to that of the lipid bilayer. Overall, the dimer probability has a large value (about 80%) over a large temperature region in the gel phase because the hydrogen bonding in dimers is considerably stronger than the van der Waals interactions in DPPC bilayers.

The equilibrium constant of dimerization, $K_{eq}$, can be related to the channel probability $P_{eq}$ by $K_{eq} \approx AP_{eq}(1 - P_{eq})^{-2}$ (Cohen, Atkinson and Summers, 1970), where $A$ is the mean area of lipid bilayer.

## 5.4 Critical Mixing of Protein and Lipids

The occurrence of critical mixing in two-component lipid membranes is a wide-spread phenomenon. There is a strong experimental evidence that it occurs in DMPC and DPPC lipid bilayers containing either gramicidin $A$ (Morrow and Davis, 1988) or synthetic transmembrane amphiphilic polypeptides of the type Lys$_2$–Gly–Leu$_n$–Lys$_2$–Ala–amide with $n = 16$ and 24 (Huschilt, Hodges and Davis, 1985; Morrow, Huschilt and Davis, 1985). The phospholipid–polypeptide systems were studied using a combination of calorimetry and NMR difference spectroscopy, therefore the resulting phase diagrams have a high degree of accuracy. The experimental data for the phospholipid–gramicidin $A$ system have not been interpreted in terms of a quantitative phase diagram although it was argued that the data are consistent with the presence of a lower critical mixing point (Morrow and Davis, 1988). Since there may also be some influence from the dimer–monomer equilibrium in the case of gramicidin $A$ which is not accounted for in the present type of modeling, we restrict ourselves to a quantitative comparison of our theoretical results of critical mixing with experimental results for DPPC lipid bilayers containing synthetic polypeptides. Since the experimental data for both the long and the short peptide are quite similar, we discuss these two systems together. It should however be noted that there is a slight quantitative difference between the phase diagram for the two peptides which can easily be rationalized in terms of the hydrophobic matching concept. The short peptide tends to stabilize the fluid phase more strongly than the long peptide because the short peptide is more closely matched to the fluid hydrophobic thickness of DPPC than the long peptide (Mouritsen and Sperotto, 1992).

Morrow and Whitehead (Morrow and Whitehead, 1988) used a Landau expansion of the free energy in terms of area per lipid molecule to obtain protein–lipid phase diagrams with critical mixing. However the phenomenological modeling does not account for the thermal density fluctuations and cannot address the microscopic origins of such phase diagrams. Hence we propose a microscopic model to describe the phase diagrams and we identify the phase boundaries by using the Lee-Kosterlitz method described in Sec. 2.3.2. Our work is therefore complementary to the work of Morrow and Whitehead.

The microscopic interaction model used in this section to describe a lipid bilayer mixed with small transmembrane proteins or polypeptides consists of two parts. The first part, $\mathcal{H}_{\rm LL}$ given in Sec. 4.3.1, describes the internal energy of the pure lipid bilayer and the second part, $\mathcal{H}_{\rm LP}$, describes the interactions between the lipid bilayer and the protein. Direct interactions between different proteins are neglected since we are only concerned with low ratios of protein to lipid. The lipid–protein interactions, $\mathcal{H}_{\rm LP}$, can be formulated in terms of a direct lipid–protein interaction in addition to a hydrophobic mismatch term

$$\mathcal{H}_{\rm LP} = \Pi A_{\rm P} \sum_{i} \mathcal{L}_{{\rm P},i} - \frac{J_{\rm LP}}{2} \left( \frac{d_{\rm P}}{d_1} \right) \sum_{(i,j)} \sum_{\alpha} I_{\alpha} \mathcal{L}_{\alpha,i} \mathcal{L}_{{\rm P},j} + \frac{\gamma_{\rm mis}^{\rm LP}}{2} \sum_{(i,j)} \sum_{\alpha} |d_{\alpha} - d_{\rm P}| \mathcal{L}_{\alpha,i} \mathcal{L}_{{\rm P},j} \tag{5.8}$$

The geometric parameters of the protein are chosen to be $A_{\rm P} = 68.0\text{Å}^2$ and $d_{\rm P} = d_{10} = 11.25\text{Å}$, where $d_{10}$ is the acyl-chain length in the fluid state. It is assumed that the protein is small in the sense that it only occupies one site of the lipid lattice. This assumption, which is made for computational convenience, will be discussed further at the end of this section. The parameter, $\gamma_{\text{mis}}^{\text{LP}}$, is related to the hydrophobic effect and describes the exposure of the longer species to water (Mouritsen and Bloom, 1984). Since we are mainly concerned with the case where $d_{\text{P}}$ is close to the hydrophobic acyl chain length in the fluid phase, we only need to consider a value of $\gamma_{\text{mis}}^{\text{LP}}$ which describes the exposure of acyl chains (rather than protein side chains) to water. As described in Sec. 4.3.1, we therefore choose $\gamma_{\text{mis}}^{\text{LP}} = \gamma_{\text{mis}} = 5 \times 10^{-16}\text{erg/Å}$. The actual value of $J_{\text{LP}}$ depends on the properties of the protein hydrophobic surface, i.e. the type of amino-acid side chains. In most of the simulations we choose the direct lipid–protein interaction parameter to be $J_{\text{LP}} = 0.25 \times 10^{-13}\text{erg}$.

In the binary mixture for a given temperature $T$, the chemical potential, $\mu$, of the proteins in the lipid controls the equilibrium composition of the mixture given by the molar fraction of proteins, $c$. The molecular composition of the system fluctuates over the miscroconfigurations of the equilibrium ensemble. We can thus use the ensemble of microconfigurations generated at equilibrium to calculate the distribution function, $n(c,\mu,T,N)$, for the composition. Here $n(c,\mu,T,N)$ denotes the probability of occurrence of a microconfiguration with composition $c$ at the values chosen for $\mu$ and $T$. The part of the free energy which describes the composition dependence of the total free energy for a fixed value of $T$, $\mu$, and system size $N$ is related to $n(c,\mu,T,N)$ as follows (Sec. 2.3.2)

$$\mathcal{F}(c,\mu,T,N) = -k_B T \ln n(c,\mu,T,N). \tag{5.9}$$

The relative stability of two different bilayer phases characterized by compositions $c^{(1)}$ and $c^{(2)}$ can now be determined by examining free-energy differences such as

$$\Delta\mathcal{F}(N) = \mathcal{F}(c^{(1)},\mu,T,N) - \mathcal{F}(c^{(2)},\mu,T,N). \tag{5.10}$$

Fig. 5.8 shows the free energy function, $\mathcal{F}(c,\mu_{\text{m}},T,N)$, for four different temperatures, $T = 313.0\text{K}$, $310.0\text{K}$, $304.0\text{K}$, and $303.5\text{K}$, all of which are below the gel–fluid phase transition temperature, $T_{\text{m}} = 313.7\text{K}$, of the pure DPPC lipid–bilayer given by

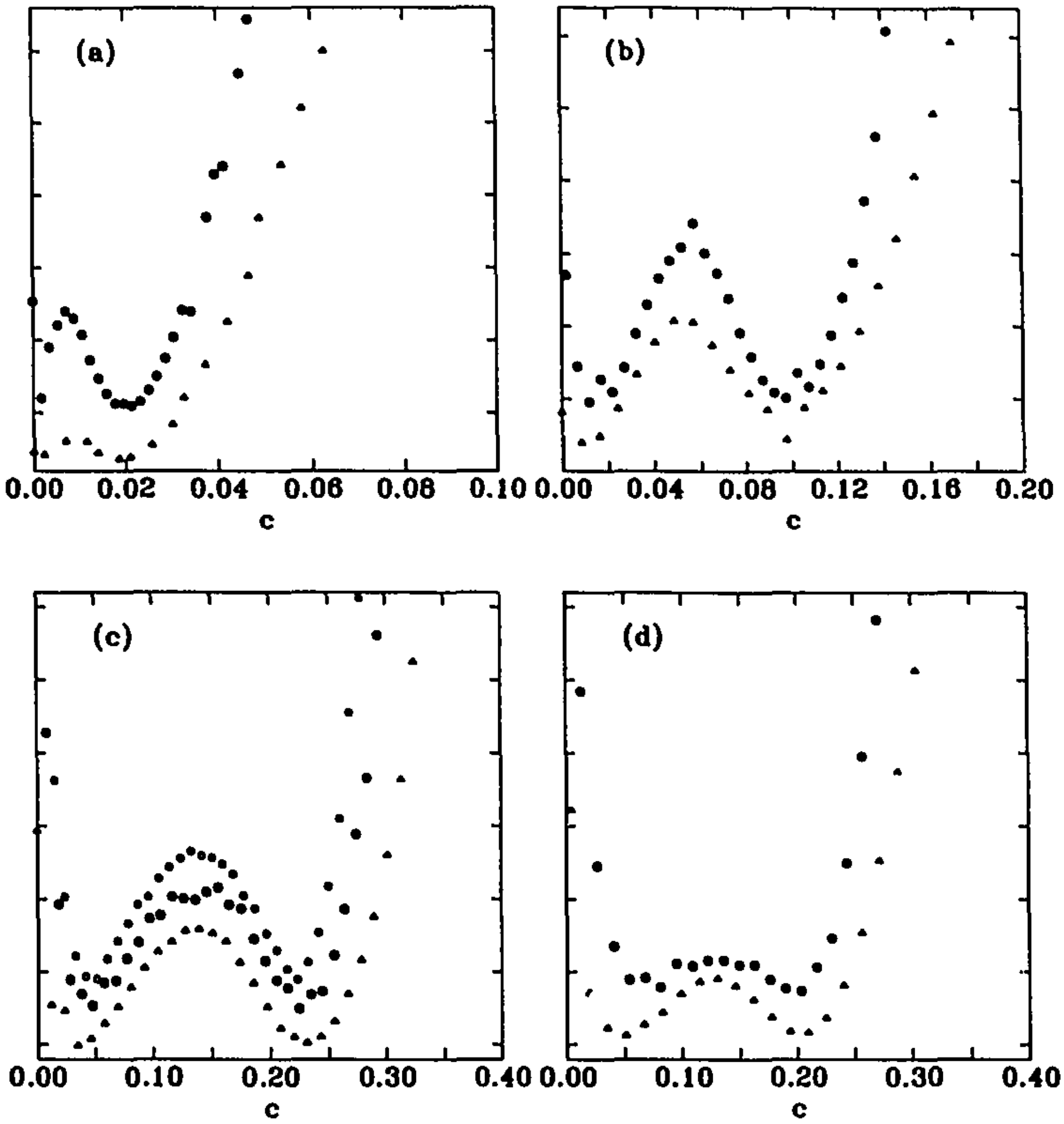

Figure 5.8: Free energy $\mathcal{F}(c, \mu_{\rm m}(N), T, N)$ as a function of bilayer composition, $c$, for different lattice sizes, $N = L \times L$, $L = 16\,(\triangle), 24\,(\bullet), 32\,(\circ)$, for three different temperatures, (a): $T$ = 313.0K, (b): $T$ = 310.0K, (c): $T$ = 304.0K, and (d): $T$ = 303.5K. $\mu_{\rm m}(N)$ refers to the chemical potential at phase coexistence for a system of size $N$ consisting of a DPPC lipid bilayer embedded with small transmembrane proteins or polypeptides.

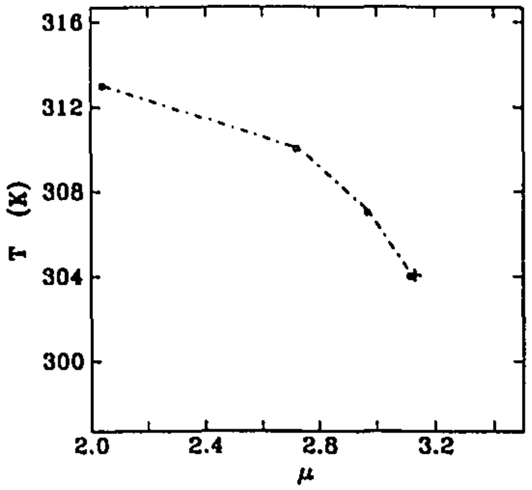

Figure 5.9: Theoretical $T$–$\mu$ phase diagram for the microscopic model of lipid–protein interactions. The lower critical mixing point is marked by (+). The diagram corresponds to a DPPC lipid bilayer embedded with small transmembrane proteins or polypeptides.

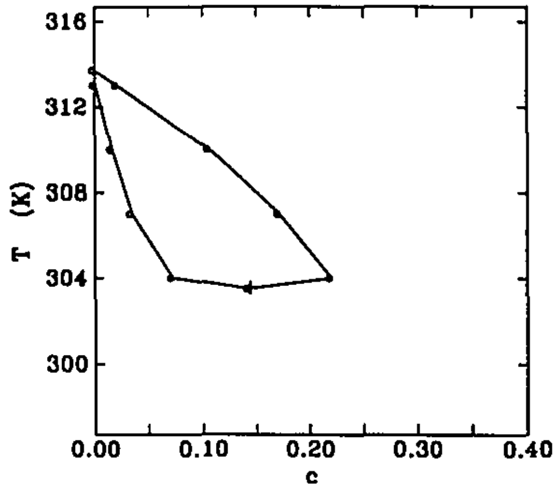

Figure 5.10: Theoretical $T$–c phase diagram (o) for the microscopic model of lipid–protein interactions. The solid curve is drawn as a guide to the eye. The critical mixing point is indicated by (+). The diagram corresponds to a DPPC lipid bilayer embedded with small transmembrane proteins or polypeptides.

present model (Sec. 4.3.1). The free energy was calculated for a value of the chemical potential, $\mu = \mu_m$, at which the two lipid phases coexist and hence the two minima of the free energy are equally deep. The following conclusions can be drawn from the size dependence of the data in Fig. 5.8. For the two higher temperatures, $T = 313.0$K and 310.0K, the free-energy barrier, $\Delta\mathcal{F}(N)$ in Eq.( 5.10), separating the two minima increases with system size indicating that the two phases are separated by a first-order transition, *i.e.* the two phases coexist in the thermodynamic limit. In contrast, at $T = 304.0$K in Fig. 5.8c, the barrier height does not depend on system size to within numerical error indicating that the system is close to a continuous transition, in this case a lower critical mixing point. For even lower temperatures, e.g. $T \leq 303.5$K, the barrier decreases with system size indicating that the difference between the two minima, and hence the two phases, vanishes in the thermodynamic limit. At these temperatures the mixture is therefore in a one-phase region at all compositions.

The phase diagram spanned by temperature and chemical potential was obtained from data of the type presented in Fig. 5.8 and is shown in Fig. 5.9. The dashed line in this figure gives the line of coexistence between the gel and fluid lipid phases. The line terminates in the critical mixing point. The corresponding phase diagram spanned by temperature and bilayer composition is displayed in Fig. 5.10. This figure shows that the lipid–protein interactions of the present microscopic model produce the characteristic 'tear-drop' shaped closed coexistence loop of a binary mixture with a lower critical mixing point. We also found an absence of phase separation at $T = 305.0$K for $J_{LP} = 0.3 \times 10^{-13}$erg. This indicates that for larger values of the direct lipid–protein interaction constant, $J_{LP}$, the critical mixing point moves towards higher temperatures. Specifically it suggests that the direct lipid–protein interactions are responsible for the location of the critical mixing point.

In order to make a direct quantitative comparison between the theoretical phase diagram in Fig. 5.10 and the corresponding experimental data, it is first necessary to scale the theoretical data in a manner which allows for the fact that the peptides in the experimental system are larger relative to the lipid acyl-chains than assumed in

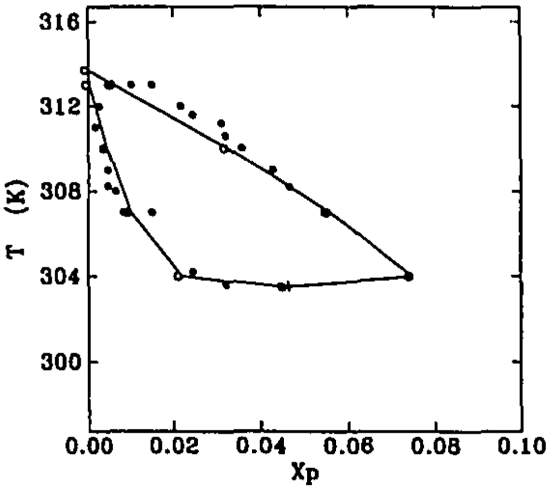

Figure 5.11: Rescaled theoretical $T$–$x_P$ phase diagram (∘) for the microscopic model of lipid–protein interactions. The rescaling is performed in order to facilitate a comparison with a specific lipid bilayer system: DPPC bilayers mixed with $\alpha$-helical amphiphilic transmembrane proteins of the type Lys$_2$–Gly–Leu$_n$–Lys$_2$–Ala–amide. The experimental data (•) for mixtures of DPPC with Lys$_2$–Gly–Leu$_{24}$–Lys$_2$–Ala–amide (Morrow, Huschilt and Davis, 1985) are shown for comparison. The solid line connecting the theoretical points is drawn as a guide to the eye.

the lattice model. In the model description it is assumed for computational convenience that the peptides are single-site objects on the lattice substituting for a single acyl chain. Although it is in principle feasible, it would be computationally more demanding to perform the simulation with objects which occupy several adjacent lattice sites. It is however possible to scale the data in Fig. 5.10 to provide an approximation to the case where the polypeptides occupy more sites and hence have a larger volume fraction. The approximation underlying this simple scaling is on the same level as the Flory-Huggins approximation for polymer blends (Flory, 1953; Huggins, 1941) which for the present system overestimates the mixing entropy. For concentrations which are not too high this approximation should be reliable. Fig. 5.11 shows the same data for the phase diagram as in Fig. 5.10 but now scaled down to a concentration measure, $x_P$, corresponding to a polypeptide which occupies seven lattice sites appropriate for a poly-leucine $\alpha$-helix, *i.e.* $x_P = c\left(\frac{7}{2} - \frac{5c}{2}\right)^{-1}$. For comparison we plot on the same figure the experimental data for the DPPC–polypeptide membrane as obtained for NMR difference spectroscopy (Huschilt, Hodges and Davis, 1985). The agreement between the experimental data and the theoretical predictions are quite satisfactory considering the approximation which underlies the concentration scaling. The good agreement suggests that the microscopic interaction model has captured the essentials of the lipid–protein interactions in the present lipid bilayer system. The experimental phase diagram for the shorter peptide with $n = 16$ is very similar (Morrow, Huschilt and Davis, 1985). Note, that since the experiments have been carried out on perdeuterated DPPC which has a lower transition point than that of normal DPPC, the experimental data have been subject to a trivial translation in temperature in order to compensate for the isotope effect and to facilitate the comparison between theory and experiment.

# Chapter 6

# Hydrogen Bonding in Lipid Bilayers

In this chapter, we propose a model for thermodynamic phase transitions and geometric transitions involving hydrogen bonding between the polar-heads of lipid bilayers (Zhang *et al.*, 1992d). The relationship of the results to experiment is discussed.

## 6.1 Introduction

As described in Chap. 4, phospholipids are surfactant-like molecules with two hydrophobic fatty acid chains and a hydrophilic polar head. The nature of the polar head is therefore important for the hydration properties of the bilayer. Two types of polar head, phosphatidylcholine (PC) and phosphatidylethanolamine (PE), together account for the polar heads of the majority of phospholipids in most cell membranes (Silvius, Brown and O'Leary, 1986). Lameller phases composed of PE hydrate less strongly than the corresponding lamellar phases of PC (Lis *et al.*, 1982), and show a much greater tendency to form dehydrated and/or non-lamellar phases than do PC lipids of comparable acyl chain composition.

Boggs (Boggs, 1980) and Hauser *et al.* (Hauser *et al.*, 1981) suggested that the differences in the hydration properties of PE and PC lipids are largely attributable

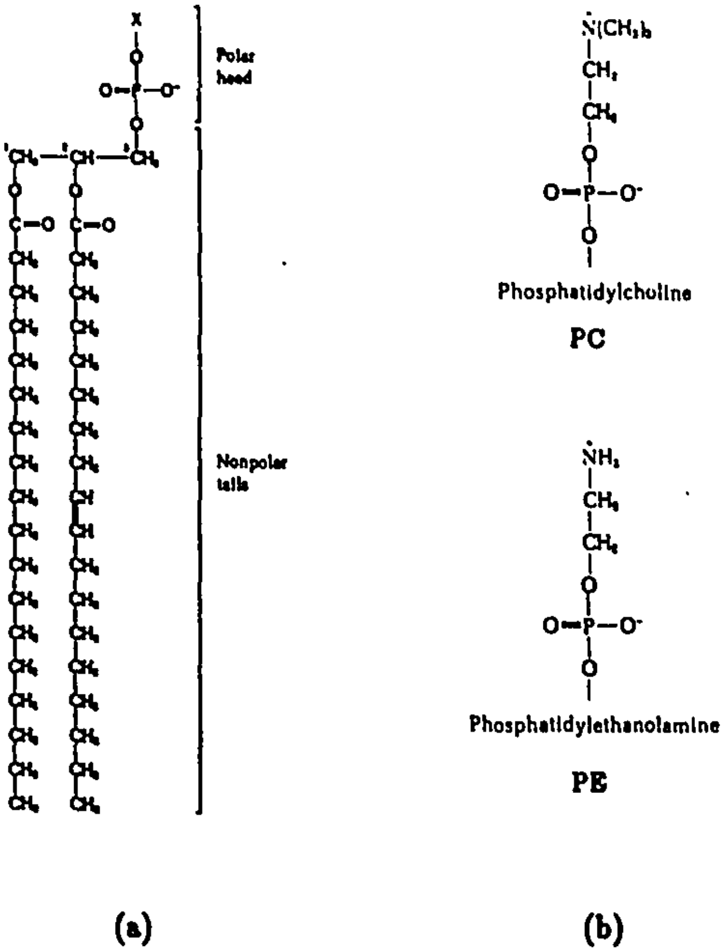

Figure 6.1: (a) General structure of phosphoglycerides; (b) Two types of polar head groups-PE and PC

to differences in the abilities of these two lipids to participate in intermolecular lipid-lipid hydrogen bonding. The hydrogen bonding of dilauroylphosphatidylethanolamine (DLPC) was investigated by using X-ray crystallography by Hitchcock *et al.* (Hitchcock *et al.*, 1974) who found that in anhydrous crystals each PE polar head was connected by N–H...O hydrogen bonds to four neighboring polar heads. Here the bonds are between the oxygens (acceptors) of the phosphate group and the hydrogens (donors) of the amino group. Since the trimethylammonio group of PC lipids cannot form hydrogen bonds, the PC headgroup can serve as an acceptor but not as a donor of hydrogen bonds.

As described in Chap. 4, fully hydrated one-component PC bilayers undergo a phase transition, known as the main phase transition, in which the bilayer passes from a gel (solid) phase to a liquid-crystalline (fluid) phase. Both these phases are stable hydrated phases. For pure PE lipid bilayers, the situation is considerably different. Several studies (Seddon, Harlos and Marsh, 1983; Seddon, Cevc and Marsh, 1983; Chang and Epand, 1983; Mantsch *et al.*, 1983; Wilkinson and Nagle, 1984; Silvius, 1991) showed that aqueous dispersions of dimyristoyl phosphatidylethanolamine (DMPE) can form at least three distinct types of lamellar phase: stable, virtually dehydrated 'crystalline' (AS) phases in which the acyl chains are rigid and tightly packed and the polar heads are presumably hydrogen bonded to one another; a hydrated solid (HS) or gel metastable phase, in which the chains are somewhat less tightly ordered; and a hydrated fluid (HF) stable phase, in which the chains are flexible. The crystalline nature of the AS phase was confirmed by the X-ray crystallographic studies of Seddon *et al.* (Seddon, Harlos and Marsh, 1983; Seddon, Cevc and Marsh, 1983) who showed that this phase has basically the same structure as the anhydrous crystal. On heating, the AS phase makes a first order phase transition to the HF phase. Several effects occur at this transition. Firstly, the solid melts and the acyl chains become flexible (chain melting). A second likely effect in the HS and HF phases is that the interlipid hydrogen bond network existing in the AS phase could be disrupted by competition with lipid–water interactions. The precise degree to which interlipid hydrogen bonding interactions are disrupted upon conversion of the AS phase to the HS or HF phase has yet to be established experimentally, although it appears that lipid–water hydrogen bonding is extensive in the HF phase in particular. In contrast to the AS to HF transition, the transition of the metastable, but long lived HS phase to the HF phase exhibits a considerably lower latent heat.

There have been a number of theoretical models relevant to hydrogen bonding in lipid bilayers. The earlier models were phenomenological models for the effect of hydrogen bonding on the transition temperature of the main phase transition proposed by Nagle (Nagle, 1976), and Eibl and Wooley (Eibl and Wooley, 1979). MacDonald *et al.* (MacDonald and Pink, 1988) proposed a microscopic model for those hydrated ceribrosides in which there is a single donor–single acceptor complex on the amide group giving rise to a 'striped' ground state composed of $1d$ hydrogen bonding networks. This model included both hydrogen bonding effects and chain melting at the main phase transition. Their model is similar to a Potts lattice gas model of krypton adsorbed on graphite proposed by Berker *et al.* (Berker, Ostlund and Putnam, 1978) and a site-bond percolation model, with temperature dependent bond probability, proposed by Coniglio *et al.* (Coniglio, Stanley and Klein, 1982) to study the sol–gel transition. Both models include a site degree of freedom which cannot bond with neighboring sites, and other degrees of freedom which are able to, but need not, bond with neighboring sites. However, in both models, the bonds are not correlated with the relative position of the sites.

## 6.2 Model for Hydrogen Bonding in Lipid Bilayers

In this section we present a microscopic lattice model to describe the hydrogen bonding aspects of the main phase transition of pure PE bilayers. It is a five state interacting model on a $2d$ square lattice which mimics both the hydrogen bonding network proposed for PE lipids by Hitchcock *et al.* (Hitchcock *et al.*, 1974) and its disrup-

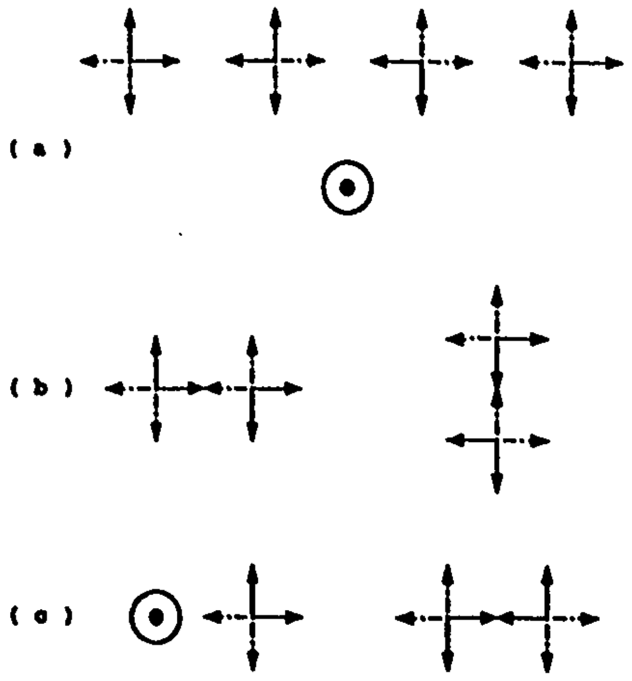

Figure 6.2: (a) Five states of the model. The solid vectors point in the direction of the HB donors and are equal to $\vec{S}^{(x)}$ and $\vec{S}^{(y)}$. The dashed vectors represent the direction of the HB acceptors. The four bonding states can be represented by $(\hat{x},\hat{y})$, $(-\hat{x},\hat{y})$, $(-\hat{x},-\hat{y})$, and $(\hat{x},-\hat{y})$ respectively. The fifth (unbonding) state is schematically represented as a circle with a dot inside. (b) Two of the bonding possibilities for nearest neighbor sites. (c) Two examples of nearest neighbor sites which do not bond.

tion by lipid-water interactions. Each lattice site represents a PE polar head which can have a maximum of four possible hydrogen bonds (HBs) with the polar heads of neighboring molecules. Each polar head has two HB donors and HB acceptors. The structure of the polar head is such that the two donors are perpendicular to each other and the donors are antiparallel to the acceptors. This is the case for PE polar heads in DLPC (Hitchcock *et al.*, 1974). Each lattice site represents a PE polar head and can be in one of five possible states (Fig. 6.2a). Four of these states are called bonding states, and we assume that for the bonding states the donors are oriented along the links between lattice sites. Since the two donors are perpendicular we associate with each bonding state a horizontal unit vector $\vec{S}^{(x)}$ corresponding to the direction of one of the donors and a vertical unit vector $\vec{S}^{(y)}$ corresponding to the direction of the other donor at the same site. Thus, the four bonding states are given by ($\vec{S}^{(x)} = \hat{x}$, $\vec{S}^{(y)} = \hat{y}$), ($\vec{S}^{(x)} = -\hat{x}$, $\vec{S}^{(y)} = \hat{y}$), ($\vec{S}^{(x)} = -\hat{x}$, $\vec{S}^{(y)} = -\hat{y}$), and ($\vec{S}^{(x)} = \hat{x}$, $\vec{S}^{(y)} = -\hat{y}$). This allows three possible arrangements on each lattice bond connected by bonding states: two donors, two acceptors, or one donor and one acceptor. In this model, a hydrogen bond of bonding energy, $E_b$, is formed when an acceptor and a donor are present on the same lattice bond. The two other arrangements have no energy associated with them. The system lowers its energy by an amount, $E_b$, when an HB is formed and the same value of the energy is required to break an HB. On each site it is possible for one of the HB donor vectors, $\vec{S}^{(x)}$ or $\vec{S}^{(y)}$ to bond without the other donor bonding. The same is true for the acceptors. Thus, from zero to four HBs can be formed between a site and its four nearest neighbors. The polar head is also allowed to be in the $5th$ state, called the 'unbonding' state (Pink, MacDonald and Quinn, 1988; Coniglio and Klein, 1980). This state has a degeneracy, $D_u$, which partially represents all possible orientations of the polar head, both in-plane and out-of-plane, for which a polar head cannot form hydrogen bonds with neighboring polar heads. The degeneracy, at low values, is principally a measure of the ability of the polar head to become hydrated by the surrounding water molecules if the energy cost of the hydration is assumed to be negligible, but it includes melted chain conformation (typical of the HS or HF phase) at higher values of $D_u$. The thermally induced competition between the formation of HBs and the degeneracy effect of the unbonding state should therefore result in a hydration–dehydration transition. For the unbonding state the donor vectors are assigned the values $\vec{S}^{(x)} = 0$ and $\vec{S}^{(y)} = 0$. Some of the various bonding possibilities are shown in Fig. 6.2(b)–(c).

The Hamiltonian for the five-state model described above can be written as follows:

$$\mathcal{H} = -E_b \sum_i [f(\vec{S}^{(x)}_{\vec{r}_i} \cdot \vec{S}^{(x)}_{\vec{r}_i+\hat{x}}) + f(\vec{S}^{(y)}_{\vec{r}_i} \cdot \vec{S}^{(y)}_{\vec{r}_i+\hat{y}})] \tag{6.1}$$

where $f(1) = 1$, $f(z) = 0$ for $z \neq 1$ and $\vec{S}^{(x)}_{\vec{r}_i}$ and $\vec{S}^{(y)}_{\vec{r}_i}$ represent the donor vectors of the $ith$ polar head located at the position $\vec{r}_i$. Note that the lattice spacing is set equal

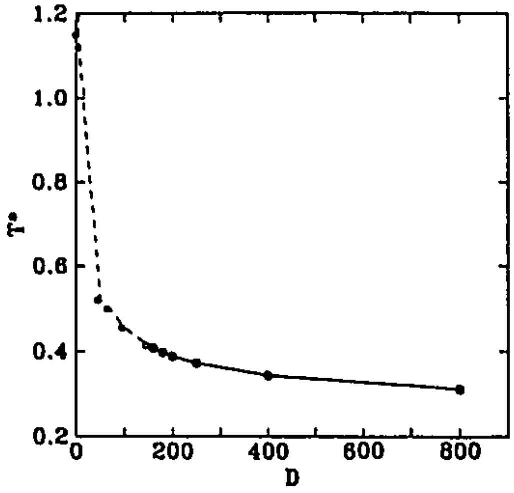

Figure 6.3: The solid line indicates a first order transition. The dashed line indicates no thermal phase transition, but the existence of a percolation transition.

to unity here.

## 6.3 Phase Diagram for the Five-State Model

In this section we examine the phase behavior of the microscopic model by the standard Metropolis Monte Carlo method with non-conserved dynamics in conjunction with the new techniques described in Chap. 2.

The phase diagram for the model in terms of $T^*(= k_B T/E_b)$ and the unbonding degeneracy, $D_u$, is shown in Fig. 6.3. For $D_u > 160$, the system undergoes a first order transition. It is determined by calculating the free energy as a function of the internal energy at the transition (Sec. 2.3.2). The typical results for the first order transition is presented in Fig. 6.4(a), which shows that the energy barrier, $\Delta\mathcal{F}(L)$ increases with increasing $L$. The first order transition is accompanied by a percolation transition. In this case the system makes an abrupt transition from the percolating case to a situation where there are only a few clusters of hydrogen bonded polar head.

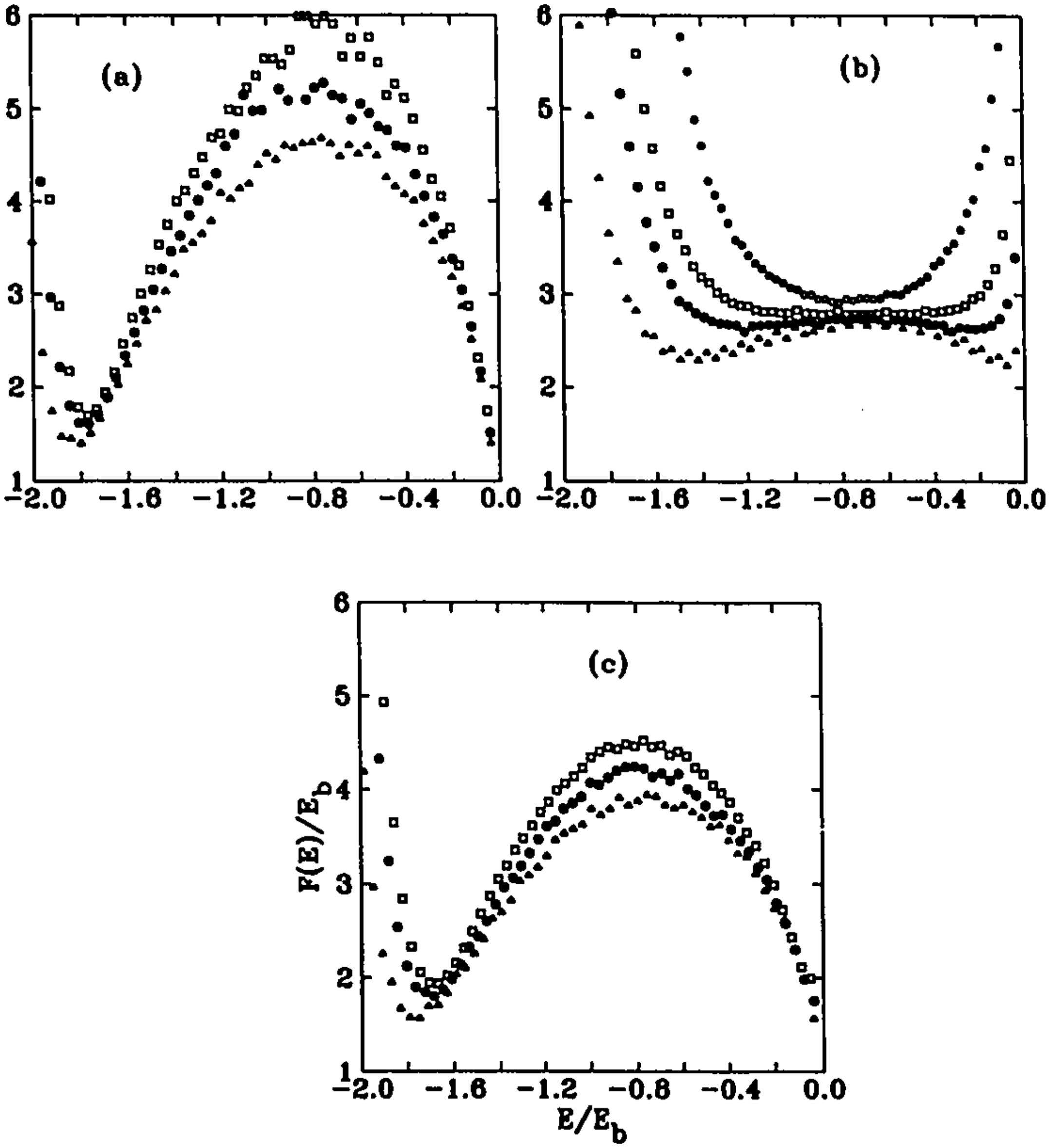

Figure 6.4: Free energy $\mathcal{F}(E,L)$ vs $E/E_b$. $D_u$ = (a) 200, (b) 100, (c) 160.

The system does not exhibit a thermal phase transition for values of $D_u$ below about 160 because $\Delta\mathcal{F}(L)$ decreases with increasing $L$ and reaches the Gaussian behavior, implying the absence of a phase transition, in the thermodynamic limit (Fig. 6.4b). At $D_u = 160$, the system is at or extremely close to a critical point. Fig. 6.4(c) shows that, in this case, the free energy as a function of $E/E_b$ exhibits two minima with a maximum between them but that the height of the maximum, $\Delta\mathcal{F}(L)$, is independent of system size to within calculational error.

The latent heat is an important quantity related to a first order phase transition. It can be obtained by integrating the specific heat. Although there is the size-effect of the specific heat for a finite system, the area under the specific heat curve is about constant which corresponds to the latent heat (Zhang *et al.*, 1992a; Zhang *et al.*, 1992c). Fig. 6.5 shows that the specific heat scales reasonably as a function of system size, $L$, for $D_u = 200$ and reaches certain limit when $L$ is large enough. The area under the reached curve in Fig. 6.5 gives the latent heat of transition, $\Delta H$, which is shown in Fig. 6.6 for several values of $D_u$ in the first order transition regime. The point at $D_u = 160$ is an estimate of the location of the critical point. The same values for $\Delta H$ also can be found by calculating the difference between the minima in free energy at the respective first order phase transition (Fig. 6.4a) although this method may require a large system.

## 6.4 Percolation Transitions at Low Degeneracies

There is no thermal phase transition along the dashed line in the phase diagram (Fig. 6.3). However, there is a percolation transition which occurs when an infinite cluster of sites connected by hydrogen bonds spans the lattice at a definite transition temperature $T_p^*$. We now wish to determine the critical properties of this transition.

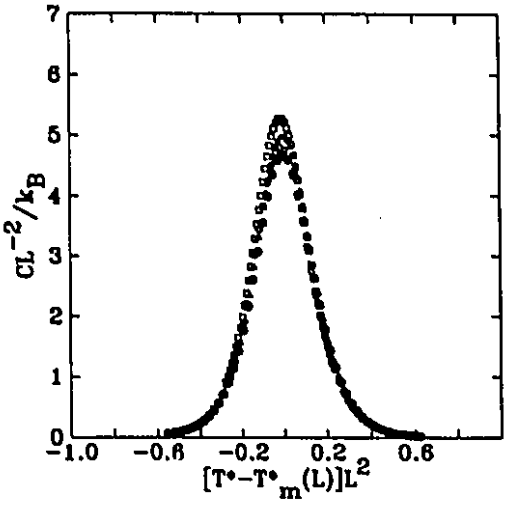

Figure 6.5: Scaling function for the specific heat for $L$ = 12, 16, 20, and 24,and $D_u = 200$. The specific heat is in units of $k_B$. The peak height of the scaling function decreases with increasing $L$.

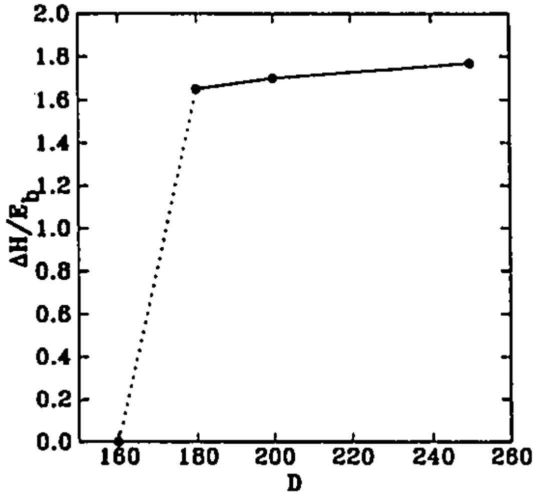

Figure 6.6: Latent heat in the regime of first order phase transitions as a function of $D_u$. The lines are guides to the eye. The point at $D_u = 160$ is an estimate of the location of the critical point

### 6.4.1 Summary of Percolation Theory

The simplest phase transition problem in statistical physics is probably the purely geometric problem of the so-called *percolation transition.* A *site percolation* problem can be described as follows. Consider a lattice which we take, for simplicity, as a two dimensional square lattice, which composed of the sites and the bonds. Each lattice site can be either occupied or unoccupied. A site is occupied with a probability $p$ ($< 1$) and unoccupied with a probability $1 - p$. For $p$ less than a certain probability $p_c$, there are only finite clusters on the lattice. A cluster is a collection of occupied sites connected by nearest neighbor distances. For $p$ larger than or equal to $p_c$ there is an infinite cluster which connects each side of the lattice with the opposite side, *i.e.*, the system percolates. For the site percolation problem all $2d$ bonds between the sites are present. In a *bond percolation*, all the sites are occupied but a bond is occupied with a probability $p$ and leave it empty with probability $1 - p$. Clusters are defined in a similar way as for the site percolation. Combining these two problems, we have the site-bond percolation. In the *site-bond percolation* problem sites are present with a probability $p_s$. Bonds can exist only between occupied sites. If two neighboring sites are occupied the bond is present with a probability $p_b$. We call the percolations mentioned above as ordinary random percolation (RP) to distinguish them from other percolations discussed in Sec. 6.4.3. They follow the hyperscaling relation described by Eq.( 6.8).

In contrast, the bootstrap percolation (BP) (Adler, 1991; Chalupa, Leath and Reich, 1981; Kogut and Riess, 1975) does not follow the hyperscaling law. In $m$ state *bootstrap percolation* configurations are generated with site probability $p$, and then occupied sites with fewer than $m$ neighbors are recursively eliminated. This culling tends to increase the value of the percolation threshold for $m > 1$. The ordinary percolation is the special case of BP with m=0.

### 6.4.2 Finite-Size Scaling for Percolation Transition

Following power laws are observed at the percolation transition, $p_c$ (Stauffer, 1984).

$$P_\infty \sim (p - p_c)^\beta \tag{6.2}$$

$$\chi \equiv \sum_s n_s s^2 \sim (p - p_c)^{-\gamma} \tag{6.3}$$

$$\xi \sim (p - p_c)^{-\nu} \tag{6.4}$$

where $P_\infty$ is the probability of an occupied site belonging to the infinite spanning cluster, $n_s$ is the number of clusters per site with $s$ sites, and $\xi$ is the connectedness length. The sum in Eq. (6.3) does not include the largest cluster. For a finite system of size $L$, the power laws lead to scaling relations:

$$P_{span}(L, \delta p) = f(\delta p L^{1/\nu}) \tag{6.5}$$

$$P_\infty(L, \delta p) = L^{-\beta/\nu} g(\delta p L^{1/\nu}) \tag{6.6}$$

$$\chi(L, \delta p) = L^{\gamma/\nu} h(\delta p L^{1/\nu}) \tag{6.7}$$

where $\delta p = (p - p_c)/p_c$, $P_{span}$ equals the probability of the system containing a spanning cluster, and $f, g$, and $h$ are scaling functions. A scaling law known as *hyperscaling* is given by

$$d\nu = \gamma + 2\beta \tag{6.8}$$

where $d$ refers to the dimension of space. The hyperscaling is satisfied by the exponents obtained for standard percolation problems (Stauffer, 1984).

### 6.4.3 Percolation Transition in the Five-State Model

The five-state model described in Eq. (6.1) is a natural example of correlated site-bond percolation. A site is occupied if it is in any one of the four bondable states. Two neighboring occupied sites are connected by a bond only if they have a hydrogen bond. Most other examples of site-bond percolation in thermally driven systems impose bonds on the system. For example, the critical point of the Ising model becomes a percolation transition if one assigns bonds between spins pointing in the same direction with a probability $1 - e^{-2J/k_BT}$ (Coniglio and Klein, 1980), where $J$ is the Ising nearest neighbor coupling. The critical percolation exponents in this case are given by their Ising model equivalents. Another example is a model of gelation in microemulsions devised by Stauffer and Eicke (Stauffer and Eicke, 1992) who use a Widom model to investigate three transitions: phase separation when the magnetization becomes non-zero, electrical percolation when an infinite cluster of up spins is formed, and gelation when an infinite cluster of up spin connected randomly by bonds with probability $p_b$ is formed. Again the bonds are imposed and are not part of the Hamiltonian. When bonds are imposed at random with a particular probability, the critical exponents are to be the same as those for ordinary percolation. According to the random percolation theory (Stauffer, 1984), the exponents of ordinary percolation are $\beta = 5/36 \approx 0.14$, $\gamma = 43/18 \approx 2.39$, and $\nu = 4/3 \approx 1.33$.

In the five-state model, the bonding probability $p$ is not a parameter. Therefore we assume that $T^*$ plays the same role as $p$ in random percolation models. Replacing $\delta p$ in Eqs. (6.5)-(6.7) by $t = (T^* - T_p^*)/T_p^*$, one has

$$P_{span}(L,t) = f(tL^{1/\nu}) \tag{6.9}$$

$$P_\infty(L,t) = L^{-\beta/\nu} g(tL^{1/\nu}) \tag{6.10}$$

$$\chi(L,t) = L^{\gamma/\nu} h(tL^{1/\nu}). \tag{6.11}$$

We use the standard cluster labeling techniques to enumerate the clusters and calculate $\chi, P_\infty$, and $P_{span}$. Similar to the case of calculating the formation of lipid domains (Sec. 4.5), the Ferrenberg-Swendsen method also allows us to calculate cluster properties at percolation transition. At $T^* = T_p^*$, according to the Eq. (6.9), $P_{span}$ is independent of the size of system. The temperature $T_p^*$ can then be determined by the crossing of the curves for $P_{span}$ versus temperature for different sizes. Two plots of $P_{span}$ as a function of $T^*$ for $D_u$ =5 and 100 respectively are presented in Fig. 6.7. It is shown that the transition region narrows as $L$ and $D_u$ increase in Fig. 6.7. The scaling function, $f$ [Eq. (6.9)], can also be used to calculate the exponent $\nu$. By fixing

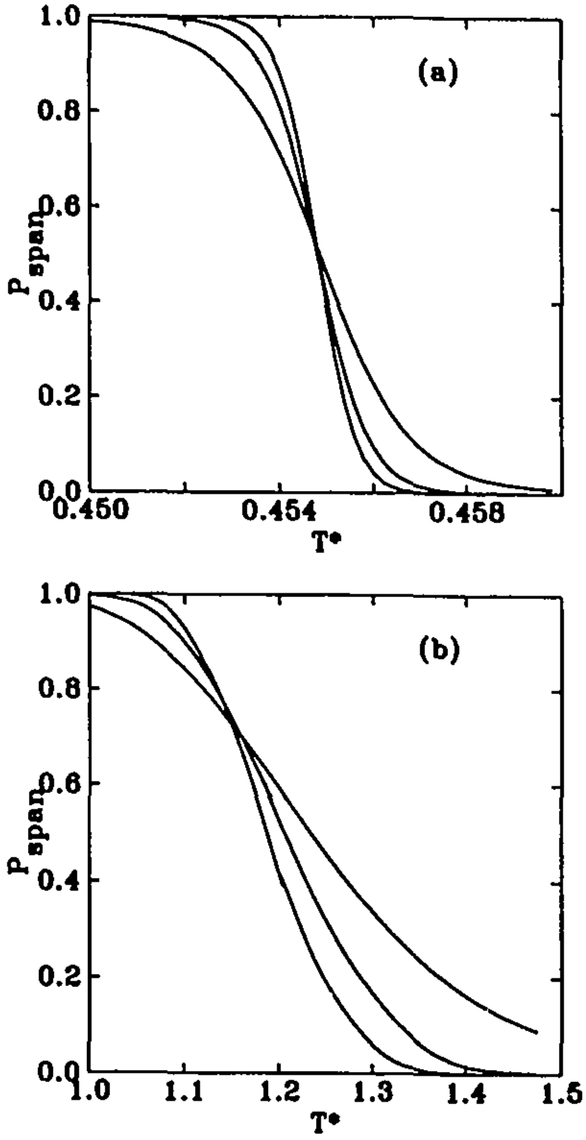

Figure 6.7: $P_{span}$ vs $T^*$ for $L = 20, 40$, and 60. (a) $D_u = 100$; (b) $D_u = 5$. The transition region narrows as $L$ increases.

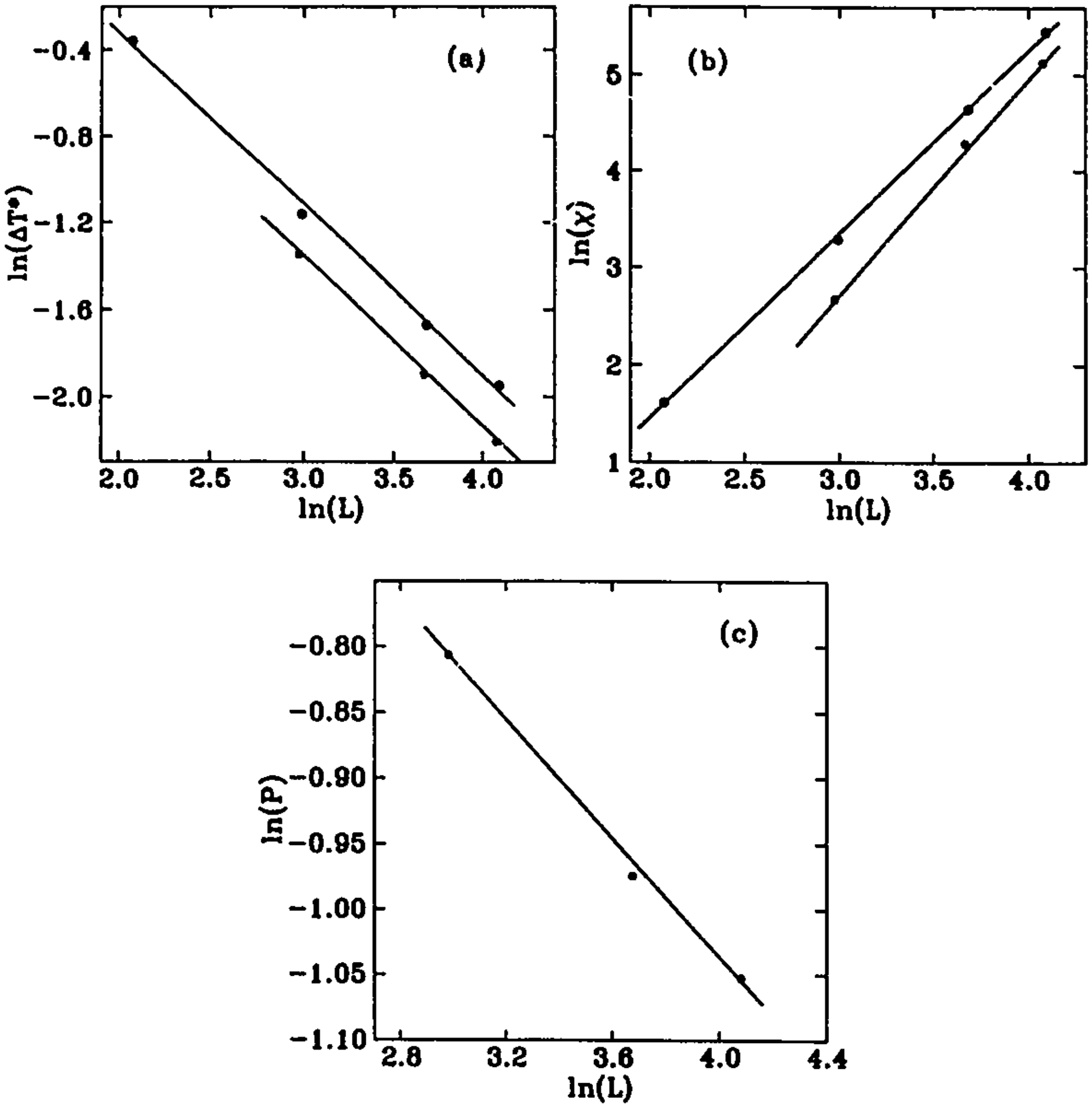

Figure 6.8: (a) $\ln\left(T_p^*(0.8) - T_p^*(0.2)\right)$ vs $\ln L$. (b) $\ln \chi$ vs $\ln L$. For (a) and (b): Lower plot for $D_u = 100$; upper plot for $D_u = 5$. (c) $\ln P_\infty$ vs $\ln L$ for $D_u = 100$.

$P_{span}(L,t) = x$ for different sizes, one has $T^*(x) - T^*_p = T^*_p c_x L^{-1/\nu}$, where $c_x$ is a constant for a given $x$, and $T^*(x)$ is the temperature at which a fraction $x$ of the configuration span vertically. Therefore, the exponent $\nu$ can be obtained from the following relation,

$$\Delta T \equiv T^*(x_1) - T^*(x_2) = T^*_p(c_{x_1} - c_{x_2})L^{-1/\nu} \sim L^{-1/\nu}. \tag{6.12}$$

The scaling plots, with $x_1 = 0.2$ and $x_2 = 0.8$, for $D_u = 100$ and $D_u = 5$ are shown in Fig. 6.8(a). To obtain the other exponents, the scaling behaviors at $T^* = T^*_p$ are studied and shown in Fig. 6.8(b) and 6.8(c).

The exponents for $D_u = 100$ are $\nu = 1.28 \pm 0.03$, $\gamma = 2.87 \pm 0.11$, and $\beta = 0.28 \pm 0.04$, where the error estimates are based on how the slopes in the log–log plots vary as we vary the estimate of $T^*_p$. As can be seen, the exponents do not follow the hyperscaling relation [Eq. (6.8)]. The value of $\nu$ is reasonably close to that of ordinary random percolation but the other two exponents are significantly higher. This is similar to the situation in bootstrap percolation. For $m = 2$ on a square lattice simulations of BP show that $\nu$ is the same as RP (Adler and Aharony, 1988), and $\beta$ is higher (Chalupa, Leath and Reich, 1981; Kogut and Riess, 1975). Although our results are not sufficiently precise to establish any quantitative connection to BP, they do show the same qualitative behavior. Also, for $m > 2$ on a square lattice BP has a first order transition at $p_c = 1$ just as the five-state model has a first order transition for large enough degeneracy.

These results can be understood quite readily. The effect of the interactions in the five-state model is to fill in the clusters that would be obtained from random percolation. This effect can easily be observed visually by examining the snapshots of configurations as shown in Fig. 6.9. One can then see that above the transition there are very few clusters, but very close to the transition there is one large cluster containing almost all the sites. This filling-in will not affect the linear extent of the clusters and thus $\nu$ will not change. However since both $P_\infty$ and $\chi$ depend on the mass of the clusters, one would expect these two exponents to increase.

For $D_u = 0$ it is clear that the transition must be at infinite temperature since the

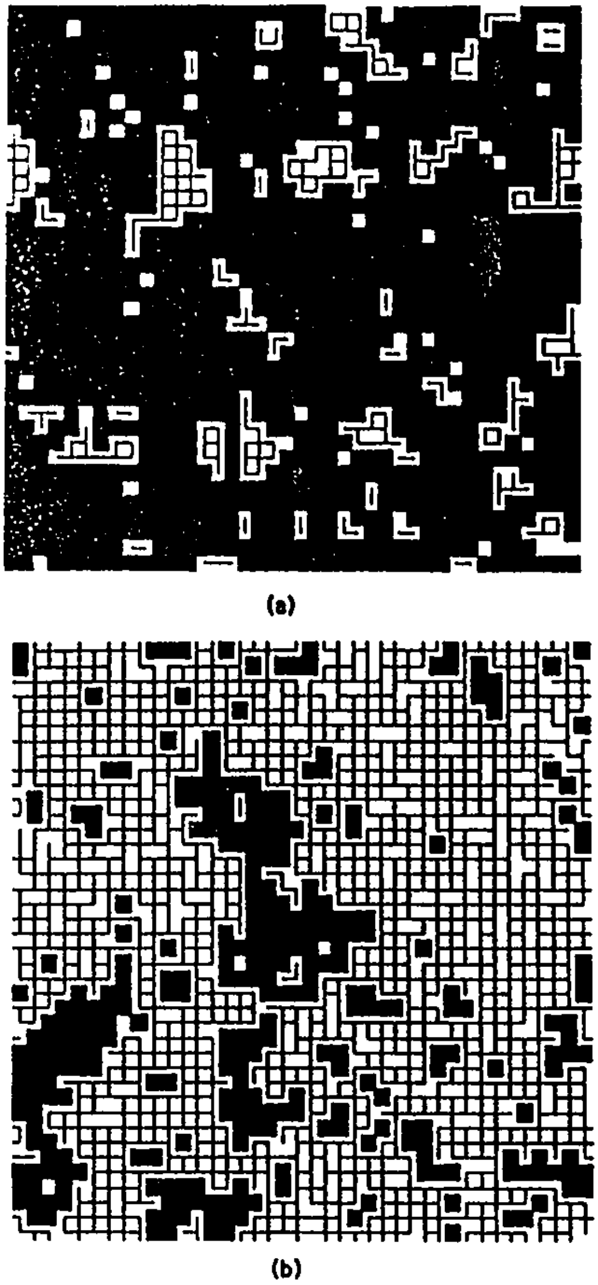

Figure 6.9: Configurations for $D_u = 100$. The shaded squares indicate unbonding states. The lines indicate actual HB bonds. (a) $T^* = 1.01T_p^*$. (b) $T^* = 0.99T_p^*$.

site probability is unity and the bond probability at finite temperatures is always less than or equal to 0.5 which is the percolation transition for random bond percolation on a square lattice. Thus, one expects the $D_u = 0$ version of the five-state model to be equivalent to random bond percolation, and to give the ordinary percolation exponents.

The presence of a percolation transition without a thermal transition resembles the suggestion of Adler and Stauffer (Adler and Stauffer, 1991) for a liquid–gas transition line above the critical temperature in the Ising model. They found an evidence for a sharp transition line where there is a change in the convergence behavior of the Taylor series expansion of the magnetization for a system in a large magnetic field. This transition line corresponds to the percolation transition based on the Kertesz droplet definition (Kertesz, 1989).

# Chapter 7

# Conclusion

In this thesis we have been concerned with the properties of theoretical models for the nematic–isotropic phase transition in thermotropic liquid crystals and for the main gel–fluid phase transition in lipid bilayers. The various Monte-Carlo simulation methods have been successfully applied to the analysis of the nature of the phase transitions, the study of phase stabilities, the determination of the phase diagrams and the analysis of the fluctuations in these models.

The computational problems arising in studies of the orientational-ordering transition in the Lebwohl–Lasher model are related to the strong pretransitional effects which make it difficult to reveal the nature of the transition and to accurately determine the transitional properties. In particular it is difficult to calculate the limits of stability of the two phases. We have in Chapter 3 been taking full advantage of the recent advances in Monte-Carlo simulation techniques of phase transitions by using the Lee–Kosterlitz method in combination with the Ferrenberg–Swendsen reweighting method. We found unambiguous evidence for a very weak first-order transition with stability limits extremely close to the equilibrium phase transition temperature. By studying the variation of the free energy around the transition temperature, the spinodal points were found to be extremely close ($\sim 10^{-3}$) to the transition temperature, in good agreement with experimental studies of room-temperature nematogens. Furthermore it was shown that the first-order character of the transition can be enhanced by introducing a term $P_4(\cos\theta_{ij})$ into the Lebwohl–Lasher model.

The director fluctuations in the Lebwohl–Lasher model have been investigated by Monte Carlo simulations which led to equilibrium time series of the nematic director and the nematic order parameter. From the $R/S$-analysis and the power spectrum, we have found that the Hurst exponent is $H \simeq 1$ for all temperatures in the nematic phase and $H \simeq 0.5$ independent of temperature in the isotropic phase. In the presence of a unidirectional ordering field, there is a crossover from $H \simeq 1$ to $H \simeq 0.5$ in the nematic phase, whereas the presence of the field does not affect the Hurst exponent in the isotropic phase. For comparison we also showed that the order-parameter fluctuations is characterized by a Hurst exponent, $H \simeq 0.5$, independent of the phase, the temperature, and the presence of the ordering field. These results indicate that the director fluctuations exhibit fractional Brownian motion in the nematic phase whereas, whenever the continuous degeneracy is broken, the fluctuations follow ordinary Brownian motion ($H = 0.5$). The finding of $H \simeq 1$ in the nematic phase was confirmed by a recent neutron-scattering experiment on the nematogen *d-PAA* (Zhang *et al.*, 1993). The field-induced crossover between fractional and normal Brownian motion is consistent with the results from the neutron-scattering studies of *d-PAA* (Otnes and Riste, 1992; Zhang *et al.*, 1993).

The Lebwohl–Lasher model is quite successful in describing experimental data for those properties of the nematic–isotropic phase transition which are not particularly material dependent. Hence a microscopic model for not only the nematic–isotropic phase transition but also the nematic–smectic $A$ phase transition may be established on the basis of the Lebwohl–Lasher model. However the positional degrees of freedom and the couplings between molecular positions and their orientations, which have been neglected in the Lebwohl–Lasher model are all present in real liquid crystals. In order to describe the phase transition involving the smectic phases, which have different spatial ordering from the nematic phase, translational variables for the molecules are required. Although a continuous variable description of the translational degrees of freedom is closer to what happens in liquid crystals, the computational problems that arise could be a real challenge to modern computers. Instead an approximate approach, similar to the Pink–Potts model of Mouritsen and Zuckermann for interfacial melting (Mouritsen and Zuckermann, 1987), could be developed by assigning Potts states to each molecule to describe its relative deviation from its position in the $3d$ lattice of the Lebwohl–Lasher model. The spatial ordering of liquid crystals would then be defined through such Potts states. On the basis of this description, we could examine the couplings between the translational and orientational freedoms that induce the layer ordering which appears in the smectic phases of liquid crystals. The relative strength of the interactions involved could be determined by the fact that there is a weakly first-order orientational transition with no spatial ordering at a higher temperature and a spatial order-disorder (second-order) phase transition at a lower temperature.

We have in Chapter 4 extended the Pink model by including hydrophobic mismatch interactions between the lipid acyl-chain conformation states and interlayer interactions between the two monolayers in order to describe the main phase transition in the lipid bilayers. The nature of the extented models was studied by using finite-size-scaling plus the Lee-Kosterlitz method. By finding the scaling function for the specific heat we obtained a latent heat of 8.12 kcal/mol in the thermodynamic limit, which is in good agreement with the experimental observations. The method of Ferrenberg and Swendsen was successfully used to calculate the cluster distributions at the phase transition. The hysteresis effects due to limited statistics in the standard Monte Carlo simulations can be easily avoided by using the new method. Our study suggested the the finite-size effects should be considered in the interpretation of experimental observations for small systems, such as large unilamellar vesicles. The mismatch between the lipid acyl-chain conformation states still needs to be verified by experiment although the concept of mismatch between lipids and proteins has been widely accepted by experimentalists.

On the basis of the extended models for pure lipid bilayers, we have in Chapter 5 extended the earlier work of Sperotto and Mouritsen for the effects of proteins on lipid bilayers. A new correlation function was introduced to describe directly the effect of proteins on correlations between lipid molecules at the main phase transition of these systems. Suppression of the correlations in the presence of proteins was found and this was shown to be consistent with recent $^2H$-$NMR$ relaxation measurements. The model describing the two monolayers in the bilayers in Chapter 4 makes the study of gramicidin channels in thermal equilibrium possible. The dependence of the equilibrium channel probabilities on temperature found in this work should be tested by doing experiments for gramicidin–phospholipid mixtures. The same interactions between gramicidins and lipids considered in this work have been used to interpretate the experimental phase diagrams of the DPPC–polypeptide mixtures successfully. We derived the phase diagram by simulations which fully account for thermal density fluctuations and which operate on the level of the free-energy thereby permitting an accurate identification of the phase boundaries for the binary mixtures. This represents progress in a field where the calculated specific heat was usually used to determine the phase diagrams because there are several examples in the literature where apparent specific-heat anomalies had incorrectly been taken as indications of a phase transition or a phase-coexistence region. Our calculations predicted a closed loop of gel–fluid coexistence with a lower critical mixing point which location is strong affected by the van der Waals-like interactions between proteins and lipids. The good agreement between the experimental data and the theoretical predictions suggests that the microscopic interaction model has captured the essentials of the lipid–protein interactions in the present lipid bilayer system. The successful use of the hydrophobic-matching concept in the modeling of lipid–protein or polypeptide interactions and its consequences for the phase equilibria should definitely be useful for the modeling of more complex membrane systems, such as ternary mixtures of lipids, polypeptides, and cholesterol. It was recently shown in an experimental $NMR$ study by Nezil and Bloom (Nezil and Bloom, 1991) that the cholesterol-induced thickening effect of short synthetic polypeptides is in agreement with the predictions of the hydrophobic-matching criterion. It would therefore be of interest to extend both the experimental and the theoretical work discussed here to such three-component systems in order to gain further insight into the nature of lipid–protein interactions in membranes.

In Chapter 6 we have proposed and analyzed a model for $2d$ hydrogen bonding networks in lipid bilayers. Our purpose was to understand the phase behavior and percolation properties of these systems in the absence of other more complex effects. We have shown by computer simulation that the model has a percolation transition in the absence of a thermal transition at low values of $D_u$ and a first-order phase transition accompanying the percolation transition for $D_u > 160$. We have investigated in detail the nature of the percolation transition for $0 < D_u < 160$, where there is no thermal transition and found that the scaling behavior cannot be described by random percolation theory, but could be similar to that found in bootstrap percolation. The exponents for the percolation transition were obtained by using the method of Ferrenberg and Swendsen.

It would be interesting to find an actual lipid system which exhibits such a percolation transition without a thermal transition. Such a transition could be inferred from spectroscopic measurements of the number of hydrogen bonds. From the point of view of hydrogen bonding in lipid bilayers, we have only described part of the behavior of the system at the main phase transition. For first order phase transitions, we identify the low temperature fully bonded phase with the dehydrated crystalline phase, which is therefore characterized by mostly bonding energy and small overall degeneracy. By contrast, the high temperature phase which is composed of mostly unbonding states and therefore represents a hydrated solid or hydrated fluid phase, is characterized by a higher degeneracy and a small energy difference between lipid-lipid and lipid-water hydrogen bonds. What is missing in the model described in Chapter 6 is a detailed analysis of the chain melting phase transition which accompanies change in the hydrogen bonding network. We intend to generalize the model to include these effects by using the Pink model to describe the chain degrees of freedom for two chains at each lattice site. Non-hydrogen bonding interactions between polar heads and differences in free energy between the dehydrated crystalline and hydrated solid phases may be introduced phenomenologically via additional energy and local entropy terms. Dynamics and metastability may also be examined in the spirit of the work done on the quenching of Ising models. Furthermore a 'toy' model for hydrogen bonding in water can be obtained by extending the model described in Chapter 6 to three dimensions.

# References

Adler, J. 1991. *Physica A*, **171**, 453.

Adler, J. and Aharony, A. 1988. *J. Phys. A*, **21**, 1387.

Adler, J. and Stauffer, D. 1991. *Physica A*, **175**, 222.

Albon, N. and Sturtevant, J. 1978. *Proc. Natl. Acad. Sci. USA*, **75**, 2258.

Bamberg, E. and Laüger, P. 1973. *J. Membr. Biol.*, **11**, 177.

Bamberg, E. and Laüger, P. 1974. *Biochim. Biophys. Acta*, **367**, 127.

Berker, A. N., Ostlund, S., and Putnam, F. A. 1978. *Phys. Rev. B*, **17**, 3650.

Biltonen, R. L. 1990. *J. Chem. Thermodynamics*, **22**, 1.

Binder, K. 1981. *Phys. Rev. Lett.*, **47**, 693.

Binder, K. and Heermann, D. W. 1988. *Monte Carlo Simulation in Statistical Physics*. Springer, Berlin.

Biscarini, F., Zannoni, C., Chiccoli, C., and Pasini, P. 1991. *Mol. Phys.*, **73**, 439.

Boggs, J. 1980. *Can. J. Biochem.*, **52**, 3425.

Caillé, A., Pink, D., de Verteuil, F., and Zuckermann, M. J. 1980. *Can. J. Phys.*, **58**, 581.

Challa, M. S. S., Landau, D., and Binder, K. 1986. *Phys. Rev. B*, **34**, 1841.

Chalupa, J., Leath, P. L., and Reich, G. R. 1981. *J. Phys. C*, **12**, L31.

Chang, H. and Epand, R. M. 1983. *Biochim. Biophys. Acta*, **728**, 319.

Chapman, D., Cornell, B. A., Eliasz, A. W., and Perry, A. 1977. *J. Mol. Biol.*, **113**, 517.

Chiccoli, C., Pasini, P., Biscarini, F., and Zannoni, C. 1988. *Mol. Phys.*, **65**, 1505.

Chiccoli, C., Pasini, P., and Zannoni, C. 1988. *Physica*, **148** A, 298.

Cleaver, D. J. and Allen, M. P. 1991. *Phys. Rev. B*, **43**, 1918.

Cleaver, D. J. and Allen, M. P. 1992. Mol. Phys. (submitted).

Cohen, G. H., Atkinson, P. H., and Summers, D. F. 1970. *Nat. New Biol.*, **231**, 121.

Coniglio, A. and Klein, W. 1980. *J. Phys. A*, **13**, 2775.

Coniglio, A., Stanley, H. E., and Klein, W. 1982. *Phys. Rev. B*, **25**, 6805.

Corvera, E., Laradji, M., and Zuckermann, M. J. 1993. Phys. Rev. E (in press).

Davis, J. H. 1979. *Biophys. J.*, **27**, 339.

Davis, J. K., Clare, D. M., Hodges, R. S., and Bloom, M. 1983. *Biochemistry*, **22**, 5298.

de Gennes, P. G. 1974. *The Physics of Liquid Crystals.* Clarendon Press, Oxford.

Doniach, S. 1978. *J. Chem. Phys.*, **68**, 4912.

Eibl, H. and Wooley, J. P. 1979. *Biophys. Chem.*, **10**, 261.

Elliott, J. R., Needham, D., Dilger, J. P., and Hayden, D. A. 1983. *Biochim. Biophys. Acta*, **735**, 95.

Fabbri, U. and Zannoni, C. 1986. *Mol. Phys.*, **58**, 763.

Feder, J. 1988. *Fractals.* Plenum Publ. Co., New York.

Feder, J. 1991. In Riste, T. and Sherrington, D., editors, *Spontaneous Formation of Space–Time Patterns and Criticality*, page 113, Dordrecht. Kluwer.

Ferrenberg, A. M. and Swendsen, R. H. 1988. *Phys. Rev. Lett.*, **61**, 2635.

Fisher, M. E. 1971. In Green, M. S., editor, *Critical Phenomena*, Academic, New York.

Flory, P. J. 1953. *Principles of Polymer Chemistry.* Cornell University Press, Ithaca.

Flory, P. J. 1969. *The Statistical Mechanics of Chain Molecules.* Wiley, New York.

Flory, P. J. 1975. *Science*, **188**, 1268.

Fraser, D. P., Zuckermann, M. J., , and Mouritsen, O. G. 1991. *Phys. Rev. A*, **43**, 6642.

Fuller, G. J., Luckhurst, G. R., and Zannoni, C. 1985. *Chem. Phys.*, **92**, 105.

Gennis, R. B. 1989. *Biomembranes.* Springer-Verlag, New York.

Georgallas, A., Hunter, D. L., Lookman, T., Zuckermann, M. J., and Pink, D. A. 1984. *Eur. Biophys. J.*, **11**, 79.

Gunton, J. D., San Miguel, M., and Sahni, P. S. 1983. In Domb, C. and Lebowitz, J. L., editors, *Phase Transitions and Critical Phenomena*, volume 8, page 267, New York. Academic Press.

Hauser, H., Pascher, I., Pearson, R. H., and Sundell, S. 1981. *Biochim. Biophys. Acta*, **650**, 21.

Henderson, R. 1981. In Balian, R. *et al.*, editors, *Membranes and Intercellular Communication*, New York. Elsevier/North-Holland Publishing Co.

Hitchcock, P. B., Mason, R., Thomas, K. M., and Shipley, G. 1974. *Proc. Nat. Acad. Sci. USA*, **938**, 3036.

Hladky, S. B. and Haydon, D. A. 1972. *Biochim. Biophys. Acta*, **274**, 294.

Huang, H. W. 1986. *Biophys. J.*, **50**, 1061.

Huggins, M. J. 1941. *J. Chem. Phys.*, **9**, 440.

Hurst, H. E. 1951. *Trans. Am. Soc. Civ. Eng.*, **116**, 770.

Huschilt, J. C., Hodges, R. S., and Davis, J. H. 1985. *Biochemistry*, **24**, 1377.

Ipsen, J. H. 1991. unpublished data.

Ipsen, J. H., Jørgensen, K., and Mouritsen, O. G. 1990. *Biophys. J.*, **58**, 1099.

Jähnig, F. 1981. *Biophys. J.*, **36**, 329.

Kahn, F. J. 1982. *Physics Today*, **35**, 66.

Kertesz, J. 1989. *Physica A*, **161**, 58.

Kogut, P. M. and Riess, I. 1975. *Phys. Status Solidi B*, **69**, K15.

Kolb, H. and Bamberg, E. 1977. *Biochim. Biophys. Acta*, **464**, 127.

Landau, L. D. and Lifshitz, E. M. 1980. *Statistical Physics*. Perganon Press, Oxford.

Lasher, G. 1970. *J. Chem. Phys.*, **53**, 4141.

Lasher, G. 1972. *Phys. Rev. A*, **5**, 426.

Lebwohl, P. A. and Lasher, G. 1972. *Phys. Rev. A*, **6**, 426.

Lebwohl, P. A. and Lasher, G. 1973. *Phys. Rev. A*, **7**, 2222(E).

Lee, J. and Kosterlitz, J. M. 1990. *Phys. Rev. Lett.*, **65**, 137.

Lee, J. and Kosterlitz, J. M. 1991a. *Phys. Rev. B*, **43**, 1268.

Lee, J. and Kosterlitz, J. M. 1991b. *Phys. Rev. B*, **43**, 3265.

Lehninger, A. L. 1979. *Biochemistry*. Worth Publishers, Inc., New York.

Lis, L. J., McAlister, M., Fuller, N., Rand, R. P., and Parsegian, V. A. 1982. *Biophys. J.*, **37**, 657.

Litster, J. D. and Birgeneau, R. J. 1982. *Physics Today*, **35**, 26.

Luckhurst, G. R. and Simpson, P. 1982. *Mol. Phys.*, **47**, 251.

MacDonald, L. and Pink, D. A. 1988. *Phys. Rev. B.*, **37**, 3552.

Maier, W. and Saupe, A. 1959. *Z. Naturforsch.*, **14 A**, 882.

Maier, W. and Saupe, A. 1960. *Z. Naturforsch.*, **15 A**, 287.

Mandelbrot, B. 1982. In Freeman, W. H., editor, *The Fractal Geometry of Nature*, page 247, San Fransisco.

Mantsch, H. H., Hsi, S. C., Butler, K. W., and Cameron, D. 1983. *Biochim. Biophys. Acta*, **728**, 325.

Marčelja, S. 1974. *Biochim. Biophys. Acta*, **367**, 165.

Metropolis, N., Rosenbluth, A., Rosenbluth, M., Teller, A., and Teller, E. 1953. *J. Chem. Phys.*, **21**, 1087.

Morrow, M. R. and Davis, J. H. 1988. *Biochemistry*, **27**, 2024.

Morrow, M. R., Huschilt, J. C., and Davis, J. H. 1985. *Biochemistry*, **24**, 5396.

Morrow, M. R. and Whitehead, J. P. 1988. *Biochim. Biophys. Acta*, **941**, 271.

Mouritsen, O. G. 1984. *Computer Studies of Phase Transitions and Critical Phenomena*. Springer–Verlag, Heidelberg.

Mouritsen, O. G. 1987. In Baeriswyl, D., editor, *Physics in Living Matter*, Berlin. Springer-Gerlag.

Mouritsen, O. G. 1990. In Brasseur, R., editor, *Molecular Description of Biological Membrane Components by Computer Aided Conformational Analysis*, Florida. CRC press, Inc.

Mouritsen, O. G. and Bloom, M. 1984. *Biophys. J.*, **46**, 141.

Mouritsen, O. G., Ipsen, J. H., Jørgensen, K., Sperotto, M. M., Zhang, Z., Corvera, E., Fraser, D. P., and Zuckermann, M. J. 1992. In Luckhurst, G. F., editor, *Computer Simulation of Liquid Crystals*, The Nederlands. Kluwer Academic Publishers.

Mouritsen, O. G. and Sperotto, M. M. 1992. In Jackson, M., editor, *Thermodynamics of Cell Surface Receptors*, Florida. CRC press, Inc.

Mouritsen, O. G. and Zuckermann, M. J. 1987. *Phys. Rev. Lett.*, **58**, 389.

Nagle, J. F. 1976. *J. Memb. Biol.*, **27**, 233.

Nezil, F. A. and Bloom, M. 1991. *Biophys. J.*, **61**, 1176.

O'Connell, A. M., Koeppe II, R. E., and Andersen, O. S. 1990. *Science*, **250**, 1256.

Otnes, K. and Riste, T. 1992. *Phys. Scr.*, **T44**, 77.

Owicki, J. C. and McConnell, H. M. 1979. *Proc. Natl. Acad. Sci. USA*, **76**, 4750.

Owicki, J. C., Springgate, M. W., and McConnell, H. M. 1978. *Proc. Natl. Acad. Sci. USA*, **75**, 1616.

Pershan, P. S. 1982. *Physics Today*, **35**, 34.

Pink, D. A. 1983. In Chapman, D., editor, *Biomembrane Structure and Function*, London. Macmillan.

Pink, D. A., Green, T. J., and Chapman, D. 1980. *Biochemistry*, **19**, 345.

Pink, D. A., MacDonald, L., and Quinn, B. 1988. *Chem. Phys. Lipids*, **47**, 83.

Sackmann, E. 1983. In Hoppe, W., Lohmann, W., Markl, H., and Ziegler, H., editors, *Biophysics*, page 425, New York. Springer-Verlag.

Sadler, D. M. and Worcester, D. L. 1982. *J. Mol. Biol.*, **159**, 485.

Salem, L. 1962. *J. Chem. Phys.*, **37**, 2100.

Saupe, A. 1968. *Angew. Chem. internat. Edit.*, **7**, 97.

Seddon, J. M., Cevc, G., and Marsh, D. 1983 *Biochemistry*, **22**, 1280.

Seddon, J. M., Harlos, K., and Marsh, D. 1983. *J. Memb. Biol.*, **258**, 3850.

Seelig, J. and Seelig, A. 1980. *Q. Rev. Biophys.*, **13**, 1.

Shinitzky, M. and Yuli, I. 1982. *Chem. Phys. Lipids*, **30**, 261.

Silvius, J. R. 1991. *Chem. Phys. Lipids*, **57**, 241.

Silvius, J. R., Brown, P. M., and O'Leary, T. J. 1986. *Biochemistry*, **25**, 4249.

Snyder, R. G. 1967. *J. Chem. Phys.*, **47**, 1316.

Snyder, R. G. 1970. *J. molec. Spectrosc.*, **36**, 222.

Sperotto, M. M. and Mouritsen, O. G. 1991. *Biophys. J.*, **59**, 261.

Stanley, H. E. 1971. *Introduction to the Theory of Phase Transitions and Critical Phenomena*. Clarendon Press, Oxford.

Stauffer, D. 1984. *Introduction to Percolation Theory.* Taylor and Francis, London.

Stauffer, D. and Eicke, H. F. 1992. *Physica A*, **182**, 29.

Stephanov, M. A. and Tsypin, M. M. 1991. *Nucl. Phys. B*, **366**, 420.

Stinson, T. W. and Litster, J. D. 1970. *Phys. Rev. Lett.*, **25**, 503.

Tevlin, P., Jones, F. P., Lafleur, S., and Trainor, L. E. H. 1986. *J. Chem. Phys.*, **85**, 4052.

Thoen, J., Marynissen, H., and Van Dael, W. 1982. *Phys. Rev. A*, **26**, 2886.

Träuble, H. and Haynes, D. H. 1971. *Chem. Phys. Lipids*, **7**, 324.

Urry, D. W., Goodall, M. C., Glickson, J. D., and Mayers, D. F. 1971. *Proc. Natl. Acad. Sci. USA*, **68**, 1907.

Wagner, R. R., Prevee, L., Brown, F., Summers, D. F., Sokol, F., and MacLeod, R. 1972. *J. Virol.*, **10**, 1228.

Watnick, P. I. and Chan, S. I. 1990. *Biochemistry*, **29**, 6215.

Wilkinson, D. A. and Nagle, J. F. 1984. *Biochemistry*, **23**, 1538.

Wulf, A. 1977. *J. Chem. Phys.*, **67**, 2254.

Zannoni, C. 1979. *Mol. Cryst. Liq. Cryst. Lett.*, **49**, 247.

Zannoni, C. 1986. *J. Chem. Phys.*, **84**, 424.

Zhang, Z., Laradji, M., Guo, H., Mouritsen, O. G., and Zuckermann, M. J. 1992a. *Phys. Rev. A*, **45**, 7560.

Zhang, Z., Mouritsen, O. G., Otnes, K., Riste, T., and Zuckermann, M. J. 1993. Phys. Rev. Lett. (accepted).

Zhang, Z., Mouritsen, O. G., and Zuckermann, M. J. 1992a. *Phys. Rev. A*, **46**, 6707.

Zhang, Z., Mouritsen, O. G., and Zuckermann, M. J. 1992b. *Phys. Rev. Lett.*, **69**, 2803.

Zhang, Z., Mouritsen, O. G., and Zuckermann, M. J. 1992c. unpublished.

Zhang, Z., Sperotto, M. M., Zuckermann, M. J., and Mouritsen, O. G. 1992b. Biochim. Biophys. Acta (in press).

Zhang, Z., Tobochnik, J., Zuckermann, M. and Silvius, J. 1992c. Phys. Rev. E (in press).

Zhang, Z., Zuckermann, M. J., and Mouritsen, O. G. 1992. Mol. Phys. (in press).

Zingsheim, H. P. and Neher, E. 1974. *Biophys. Chem.*, **2**, 197.

Zuckermann, M. J. and Mouritsen, O. G. 1987. *Eur. Biophys. J.*, **15**, 77.